PREPARATION OF $MnFe_2O_4$-BASED NANOCOMPOSITE PHOTOCATALYST FOR THE DEGRADATION OF DYE AND PHARMACEUTICAL CONTAMINATED IN THE SYNTHETIC WASTEWATER

SAKCHAI KAEWSUBDEJSIRI

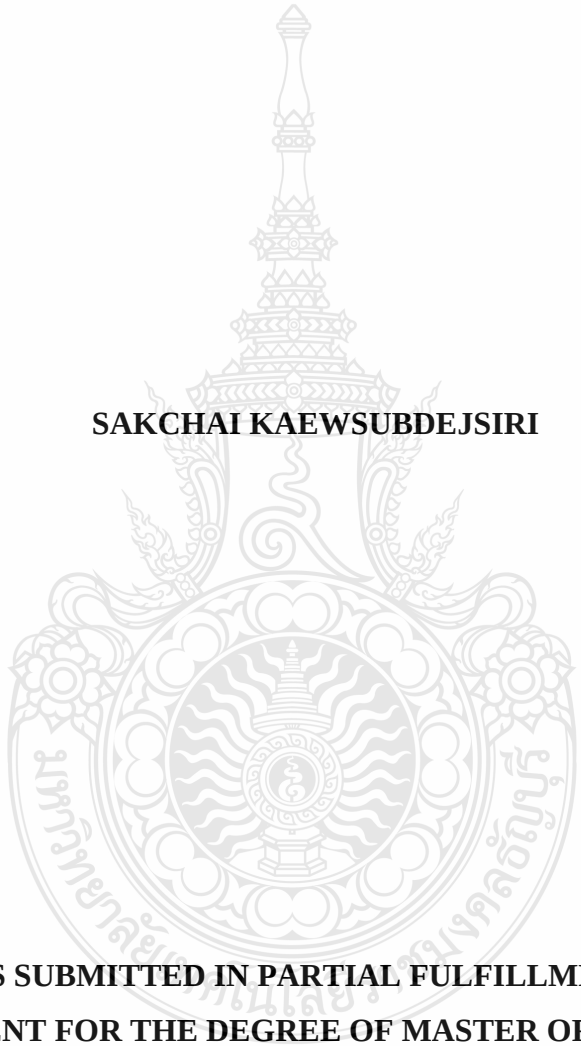

A THESIS SUBMITTED IN PARTIAL FULFILLMENT OF THE REQUIREMENT FOR THE DEGREE OF MASTER OF ENGINEERING
PROGRAM IN CIVIL ENGINEERING
FACULTY OF ENGINEERING
RAJAMANGALA UNIVERSITY OF TECHNOLOGY THANYABURI
ACADEMIC YEAR 2024

PREPARATION OF $MnFe_2O_4$-BASED NANOCOMPOSITE PHOTOCATALYST FOR THE DEGRADATION OF DYE AND PHARMACEUTICAL CONTAMINATED IN THE SYNTHETIC WASTEWATER

SAKCHAI KAEWSUBDEJSIRI

A THESIS SUBMITTED IN PARTIAL FULFILLMENT OF THE REQUIREMENT FOR THE DEGREE OF MASTER OF ENGINEERING
PROGRAM IN CIVIL ENGINEERING
FACULTY OF ENGINEERING
RAJAMANGALA UNIVERSITY OF TECHNOLOGY THANYABURI
ACADEMIC YEAR 2024

PREPARATION OF $MnFe_2O_4$-based NANOCOMPOSITE PHOTOCATALYST FOR THE DEGRADATION OF DYE AND PHARMACEUTICAL CONTAMINATED IN THE SYNTHETIC WASTEWATER	**MR. SAKCHAI KAEWSUBDEJSIRI**	**2024**

วิทยานิพนธ์ฉบับนี้เป็นงานวิจัยที่เกิดจากการค้นคว้าและวิจัย ขณะที่ข้าพเจ้าศึกษาอยู่ในคณะวิศวกรรมศาสตร์ มหาวิทยาลัยเทคโนโลยีราชมงคลธัญบุรี ดังนั้นงานวิจัยในวิทยานิพนธ์ฉบับนี้ถือเป็นลิขสิทธิ์ของมหาวิทยาลัยเทคโนโลยีราชมงคลธัญบุรี และข้อความต่างๆในวิทยานิพนธ์ฉบับนี้ ข้าพเจ้าขอรับรองว่าไม่มีการคัดลอกหรือนำงานวิจัยของผู้อื่นมานำเสนอในชื่อของข้าพเจ้า

This thesis consists of research materials conducted at the Faculty of Engineering, Rajamangala University of Technology Thanyaburi and hence the copyright owner. I hereby certify that the thesis does not contain any forms of plagiarism.

.....

(Mr. Sakchai Kaewsubdejsiri)

Thesis Title	Preparation of $MnFe_2O_4$-based nanocomposite photocatalyst for the degradation of dye and pharmaceutical contaminated in the synthetic wastewater
Name - Surname	Mr. Sakchai Kaewsubdejsiri
Program	Civil engineering
Thesis Advisor	Associate Professor Thammasak Rojviroon, D. Eng.
Academic Year	2024

THESIS COMMITTEE

.....Chairman
(Associate Professor Orawan Rojviroon, D. Eng.)

.....Committee
(Associate Professor Sanya Sirivithayapakorn, Ph.D.)

.....Committee
(Assistant Professor Kullaya Saricheewin, D. Eng.)

.....Committee
(Associate Professor Thammasak Rojviroon, D.Eng.)

Approved by the Faculty of Engineering, Rajamangala University of Technology Thanyaburi in Partial Fulfillment of the Requirements for the Degree of Master of Engineering

..... Dean of Faculty of Engineering
(Associate professor Sorapong Pavasupree, Ph.D.)
Date.....Month.....Year.....

Thesis Title	Preparation of $MnFe_2O_4$-Based Nanocomposite Photocatalyst for the Degradation of Dye and Pharmaceutical Contaminants in Synthetic Wastewater
Name - Surname	Mr. Sakchai Kaewsubdejsiri
Program	Civil Engineering
Thesis Advisor	Associate Professor Thammasak Rojviroon, D.Eng.
Academic Year	2024

ABSTRACT

This thesis investigated the enhancement of photocatalytic efficiency of manganese ferrite ($MnFe_2O_4$) by integrating it with graphitic carbon nitride ($g\text{-}C_3N_4$) for the degradation of organic dyes and pharmaceutical contaminants in synthetic wastewater. The $MnFe_2O_4/g\text{-}C_3N_4$ (MnFG) nanocomposites were successfully synthesized via a hydrothermal method and evaluated for their photocatalytic performance in degrading pollutants such as Indigo Carmine (IC), Reactive Black 5 (RB5), and Tetracycline (TC).

Comprehensive characterization of the photocatalysts was conducted using X-ray diffraction (XRD) for phase analysis, scanning electron microscopy (SEM) and transmission electron microscopy (TEM) for morphology and structural observations, Fourier-transform infrared spectroscopy (FT-IR) for functional group identification, X-ray photoelectron spectroscopy (XPS) for surface composition, ultraviolet-visible diffuse reflectance spectroscopy (UV-vis DRS) for optical properties, and photoluminescence spectroscopy (PL) for charge carrier dynamics.

The $g\text{-}C_3N_4$-enhanced MnFG nanocomposites exhibited over 99% degradation efficiency for IC and RB5, and high efficiency for TC under visible light irradiation. TC kinetic analysis revealed that the degradation followed pseudo-first-order kinetics, indicating a strong correlation between composite composition and photocatalytic activity. These findings demonstrated the potential of MnFG nanocomposites for effective environmental remediation and provided a foundation for future research focused on optimizing composite design and elucidating underlying photocatalytic mechanisms.

Keywords: Photocatalysis, $MnFe_2O_4$, $g\text{-}C_3N_4$, wastewater treatment, organic dyes, environmental remediation.

Acknowledgments

This research study has been successfully accomplished through the generosity and support of Assoc. Prof. Dr. Thammasak Rojviroon, Assoc. Prof. Dr. Orawan Rojviroon, Asst. Prof. Dr. Ranjith Rajendran, Ms. Nicharee Akechatree, Ms. Yuwadee Leelert, and Ms. Kanchana Loytala. Their invaluable knowledge, suggestions, and recommendations have played a significant role in enhancing this research work. The researcher extends heartfelt gratitude for the commitment and kindness of everyone who dedicated their time and effort.

The researcher also wishes to thank and dedicate all the merits of this research to the parents and friends who provided unwavering support and encouragement throughout the research process. Furthermore, the success of conducting this research is also attributed to the assistance and provision of analytical tools and equipment from the staff of the Civil Engineering Department, Faculty of Medicine, Rajamangala University of Technology Thanyaburi, as well as to all faculty members who contributed their knowledge and guidance in carrying out the research. Thank you for all the support.

Finally, the researcher sincerely hopes that this study will be beneficial to those interested, and apologizes for any shortcomings or incompleteness that may occur in this research work.

Mr. Sakchai Kaewsubdejsiri

Table of Contents

Table of Contents (Continued)

List of Tables

List of Tables (Continued)

List of Tables (Continued)

List of Tables (Continued)

List of Tables (Continued)

List of Figures

List of Figures (Continued)

List of Abbreviations of Thesis

g-C_3N_4	Graphitic Carbon Nitride
IC	Indigo Carmine
RB5	Reactive Black 5
TC	Tetracycline
MnFG	Manganese Ferrite Graphitic Carbon Nitride Composite
UVA	Ultraviolet A
XRD	X-ray Diffraction
XPS	X-ray Photoelectron Spectroscopy
SEM	Scanning Electron Microscopy
TEM	Transmission Electron Microscopy
EDS	Energy Dispersive X-ray Spectroscopy
ROS	Reactive Oxygen Species

CHAPTER 1

INTRODUCTION

1.1 Background and importance

Enhancing the potential of photocatalysts at the nanoparticle level is currently one of the key challenges to the application of photocatalytic technologies to environmental cleanup issues. The necessity of finding solutions to this worldwide issue, encompassing air pollution, wastewater treatment, and environmental contamination, promptly spurred extensive investigations into the principles of photocatalyst design. The utilization of composite materials in preparing photocatalysts has been demonstrated to greatly augment the efficiency of the photocatalytic process across several dimensions, including increased surface area, enhanced stability, reduced toxicity, improved cost-effectiveness, and recyclability. Furthermore, it boasts the highest efficiency in decomposing pollutants, rendering it an intriguing option for both theoretical exploration and practical implementation [1-5].

One important way to increase the effectiveness of the photocatalytic process is to use graphitic carbon nitride (g-C_3N_4) when creating photocatalysts [6]. The exceptional optical properties and chemical stability of g-C_3N_4 provide the explanation [7-9]. Concurrently, the performance of the photocatalyst is improved through synergistic integration because of its advantageous electrical conductivity characteristics [10-13]. To get the ideal combination of properties and improve stability and efficiency for environmental applications, composite photocatalyst design is essential [14-17]. As a result, a crucial step in the photocatalytic process is the careful selection of photocatalyst reactants. A promising approach to enhance the photocatalytic properties of photocatalysts involves incorporating metal oxides, such as CeO_2, TiO_2, SnO_2, WO_3, and ZnO into the precursor material [18, 19]. The photocatalytic process holds significant potential due to its unique properties and wide-ranging applications. In-depth research on this strategy can lead to the discovery of high-performance photocatalysts that effectively promote the production, separation, and utilization of photoexcited carriers in organic synthesis [20, 21]. Materials or metal oxides integrated with photocatalysts can leverage the distinctive properties of different materials [19, 22]. Researchers have at their disposal

a powerful toolkit to manipulate light harvesting, adsorption capacity, and ultimately the activity and selectivity of photocatalysts [22]. Harnessing electronic properties to control reaction selectivity has been proven to be a viable approach due to the presence of highly oxidative radical species under ultraviolet light [23, 24]. Moreover, the highly efficient charge separation of nanocomposites is particularly intriguing due to their novel properties. The first challenge to improve selectivity for a specific oxidation reaction is to better understand the reaction kinetics of photocatalysts [25]. Significant knowledge gaps remain regarding the surface characteristics of photocatalysts, the properties of materials such as $MnFe_2O_4$, Fe_2O_3, $BiVO_4$, and WO_3 [26], and the application of synthetic methods, which serve as a powerful tool for investigating surface properties and photocatalytic reactions [19]. Electrons can undergo photoexcitation when molecules exhibit positive adsorption energy, and such combinations may provide multiple advantages, including enhanced stability, broader absorption spectra, reduced charge recombination due to lower light intensity, improved photocatalytic properties, and synergistic effects that decrease the energy band gap [19, 26, 27].

In this study, an advanced photocatalyst, $MnFe_2O_4$/g-C_3N_4 (MnFG), is developed by integrating the metal oxide MnFe2O4 with carbon-based precursors $MnFe_2O_4$ and g-C_3N_4 using the hydrothermal method to enhance pollutant degradation. The research aims to evaluate photocatalytic efficiency and explore the reaction mechanisms involved in pollutant decomposition using the synthesized MnFG photocatalyst. This work focuses on two types of contaminants: synthetic dyes wastewater and synthetic pharmaceutical wastewater.

1.2 Purpose of the Study

1.2.1 Synthesis and analysis of the photocatalytic physical properties of the MnFG photocatalyst for the preparation of nanocomposites.

1.2.2 Evaluation of the degradation efficiency of the synthesized photocatalysts under the photocatalytic process.

1.2.3 Investigation of the kinetics of the photocatalytic degradation process.

1.3 Scope of works

1.3.1 Preparation of Photocatalyst: The photocatalyst utilized in this study is $MnFe_2O_4$/g-C_3N_4 (MnFG), synthesized through the hydrothermal method.

1.3.2 Experimental Setup: All experiments are conducted using a batch reactor system.

1.3.3 Two types of synthetic wastewater are employed in the experiments:

- Synthetic wastewater polluted with dyes, specifically indigo carmine (IC) and reactive black 5 (RB5).
- Synthetic wastewater containing pharmaceutical pollutants, specifically tetracyclines.

1.3.4 Kinetic Analysis: The photocatalytic degradation process is analyzed based on pseudo-first-order reaction kinetics.

1.4 Expected benefits

1.4.1 Development of photocatalysts with optimal properties and high efficiency, making them suitable for application in photocatalytic processes for wastewater treatment.

1.4.2 Establishment of a viable alternative for advanced wastewater treatment technologies, contributing to more effective contaminant removal.

1.4.3 Acquisition of comprehensive kinetic analysis data to enhance understanding of contaminant degradation mechanisms and process efficiency.

CHAPTER 2
REVIEW OF THE LITERATURE

2.1 Introduction to Photocatalytic.

Photocatalysis has emerged as a pivotal technology in environmental remediation and renewable energy production, leveraging light energy to drive chemical reactions. This process hinges on semiconductors that absorb photons, generating electron-hole pairs capable of initiating redox reactions to degrade pollutants or produce clean fuels [23, 24, 28]. Photocatalytic addresses critical challenges such as wastewater treatment, air purification, and carbon dioxide reduction, aligning with Sustainable Development Goals (SDGs) for clean water, affordable energy, and climate action [29-31].

At the core of Photocatalytic lies the excitation of a semiconductor material by light, typically with energy exceeding its bandgap. This generates electron-hole pairs that migrate to the surface, where they participate in redox reactions [23, 32-34]. Photocatalysts absorb ultraviolet (UV) light to produce electrons in the conduction band (CB) and holes in the valence band (VB) [28, 32, 35].These charge carriers can reduce oxygen to superoxide radicals ($\cdot O_2^-$) or oxidize water to hydroxyl radicals ($\cdot OH$), both potent oxidants for organic pollutant degradation[23, 32, 33, 36] as shown in Figure 2.1. The efficiency of this process depends on minimizing electron-hole recombination, achieved through structural modifications like doping or heterojunction formation[23, 28, 33].

2.1.1 Photocatalyst.

A photocatalyst is defined as a semiconducting material that absorbs photons to generate electron-hole pairs, initiating redox reactions without being consumed in the process. Unlike conventional catalysts, photocatalysts require light irradiation to activate their catalytic properties, enabling reactions under ambient conditions. The mechanism begins with photon absorption, where energy exceeding the material's bandgap promotes electrons (e^-) from the valence band (VB) to the conduction band (CB), leaving positively charged holes (h^+) in the VB [37, 38]. These charge carriers migrate to the catalyst surface, where they interact with adsorbed species such as water, oxygen, or pollutants, producing reactive oxygen species (ROS) like hydroxyl radicals ($\bullet OH$) and superoxide anions ($\bullet O_2^-$) [37].

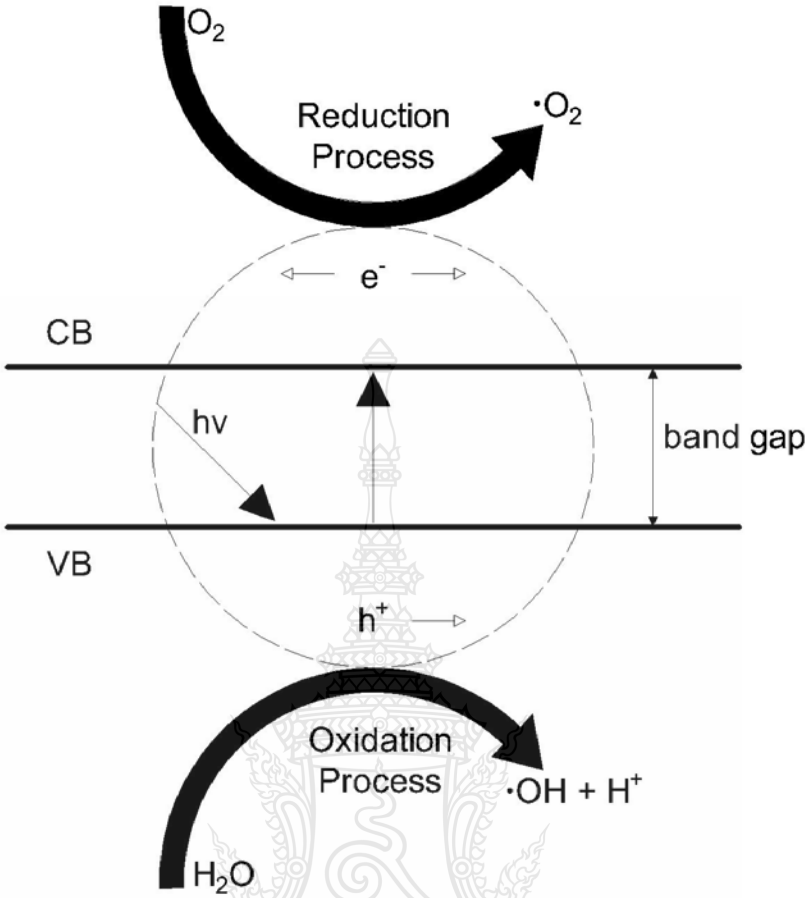

Figure 2.1 Mechanism of Photocatalytic Photodegradation.

2.1.2 Classification of Photocatalysts

Photocatalytic materials are systematically categorized based on their structural composition, charge transfer mechanisms, and operational efficiencies in light-driven chemical reactions. Contemporary research identifies six primary classifications, each addressing specific energy conversion and environmental remediation challenges through tailored photophysical properties.

- **Metal Oxide-Based Photocatalysts**.

Metal oxides dominate photocatalytic systems due to their tuneable band gaps and stability. TiO_2 (3.2 eV bandgap) and ZnO (3.3 eV) exhibit UV-driven activity, while doping (e.g., W, Fe) reduces bandgaps to ~2.5 eV for visible-light absorption [39, 40]. Mesoporous TiO_2 (10 nm pores) enhances mass transport, achieving

70% site accessibility over cycles [40]. Three-Dimensional Ordered Microstructure of Titanium Dioxide (3DOM TiO_2) architectures (300 nm macropores) enable dual photocatalytic-thermocatalytic toluene conversion (90% efficiency) [39].

$MnFe_2O_4$, a spinel ferrite, has a 1.9–2.4 eV bandgap and cubic structure (Fd-3m space group). Its magnetic properties arise from Mn(II) and Fe(III) in tetrahedral/octahedral sites, enabling efficient charge separation [41, 42]. Ce-doped $MnCe_xFe_{2-x}O_4$ increases lattice parameters (8.388 A at x=0.5) and enhances methylene blue degradation (91.53% efficiency) [41].

- **Spinel Ferrite Photocatalysts**

Spinel ferrites (AB_2O_4) integrate transition metals in tetrahedral (A) and octahedral (B) sites, enabling visible-light absorption through d-d electron transitions. Manganese ferrite ($MnFe_2O_4$) exemplifies this class, with a cubic spinel structure (Fd-3m space group) and lattice parameter of 8.343–8.388 Å [34, 41]. Its 2.42 eV bandgap allows absorption up to 512 nm, while Fe^{3+}/Mn^{2+} redox pairs facilitate hole-mediated degradation pathways. $MnFe_2O_4$ nanoparticles (6–24 nm) exhibit 92% acid violet 7 degradation under UV light via hydroxyl radical (·OH) generation [34, 43].

Comparative studies show $MnFe_2O_4$ outperforms cobalt ferrite ($CoFe_2O_4$) due to higher surface area (72.3 vs. 65.85 m^2/g) and stability [34, 43]. Heterostructures like $CeO_2/MnFe_2O_4$ enhance charge separation through p-n junctions, achieving a 0.0108 min^{-1} degradation rate constant for methylene blue 2.8× faster than pure $MnFe_2O_4$ [44, 45]. Challenges include photo corrosion under visible light, mitigated by sacrificial agents (S^{2-}/SO_3^{2-}) that scavenge holes [43, 46].

- **Polymeric Semiconductor Photocatalysts**

Graphitic carbon nitride (g-C_3N_4) represents a metal-free polymeric photocatalyst with a 2.7 eV bandgap, enabling visible-light absorption up to 460 nm. Its layered structure comprises tri-s-triazine units connected by tertiary amines, providing a high specific surface area (up to 202 m^2/g) and π-conjugated electron systems [46, 47]. Nitrogen vacancies in g-C_3N_4 create mid-gap states, reducing recombination and enhancing CO_2 reduction efficiency (62.5% aromatic yield) [42, 47].

Modifications like exfoliation into quantum dots or doping with phosphorus (P) narrow the bandgap to 1.5 eV, extending absorption into the near-infrared

[46, 48]. Z-scheme heterojunctions (e.g., g-C_3N_4/$W_{18}O_{49}$) preserve redox potentials, achieving 1097 μmol·h^{-1} hydrogen evolution 40% higher than pristine g-C_3N_4 [42, 49]. However, low quantum efficiency (≤18%) and rapid charge recombination remain challenges, addressed through hydrogel immobilization or machine learning-guided design [42, 48].

- **Composite Heterojunction Systems**

Composite photocatalysts combine multiple materials to optimize light absorption and charge separation. Type-II heterojunctions (e.g., α-Fe_2O_3/TiO_2) spatially separate electrons and holes via staggered band alignments, while Z-scheme systems (e.g., $BiVO_4$/g-C_3N_4) mimic natural photosynthesis for high redox efficiency[43, 49]. The MoS_2/CdS/TiO_2 ternary system demonstrates vectorial electron transfer, with CdS (−0.52 eV CB) injecting electrons into TiO_2 (−0.29 eV CB) and MoS_2 providing H_2 adsorption sites[49, 50].

Core-shell structures like Cu_xO@TiO_2 leverage visible-light absorption from copper oxides (1.2–2.0 eV) and TiO_2's stability, maintaining 85% Cr(VI) reduction over 10 cycles [41, 42]. Challenges include interfacial charge resistance and scalability limitations, particularly for three-dimensionally ordered microporous (3DOM) architectures, causing 30% pressure drops in flow reactors [42, 51].

2.1.3 $MnFe_2O_4$ nanoparticles

Manganese ferrite ($MnFe_2O_4$) nanoparticles are spinel-type ferrites with a cubic crystal structure (space group Fd3m), where Mn^{2+} and Fe^{3+} ions occupy tetrahedral (A) and octahedral (B) sites [52] shown in Figure 2.2. Synthesized via coprecipitation, hydrothermal, or sol-gel methods, these nanoparticles exhibit tunable sizes (5–38 nm) depending on synthesis parameters like pH, annealing temperature (500–1200°C), and dopants [53-55]. For instance, coprecipitation at pH 9–12 yields particles with crystallite sizes of 5–15 nm, while sol-gel methods produce 27.4 nm particles confirmed by XRD [52, 55]. The lattice parameter ranges from 8.34 Å to 9.40 Å, influenced by Fe/Mn ratios and synthesis conditions [53, 54]. The properties of $MnFe_2O_4$ are present in table 2.1 and the Advantages and Limitations are in table 2.1

Table 2.1 Properties of $MnFe_2O_4$

Properties	Details	References
Crystal Structure	Cubic spinel (Fd3m), lattice parameter 8.34–9.40 Å	[53-55]
Particle Size	5–38 nm (TEM/XRD)	[52, 55, 56]
Bandgap	1.4–1.9 eV	[55, 56]

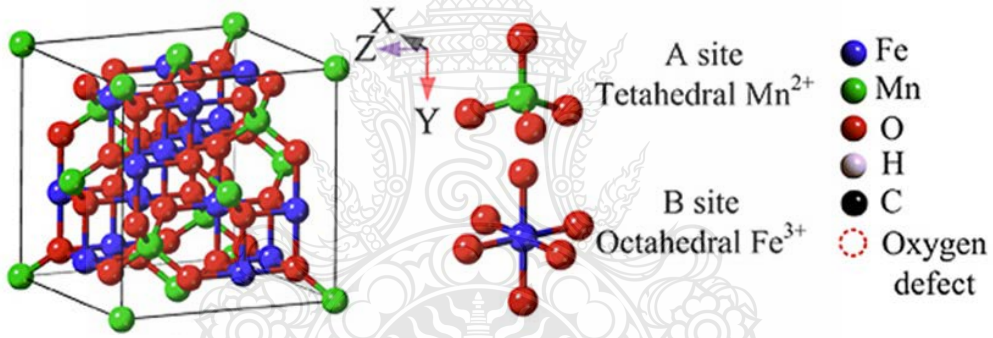

Figure 2.2 Schematic diagram of $MnFe_2O_4$ [57]

2.1.4 Graphitic carbon nitride (g-C_3N_4)

Graphitic carbon nitride (g-C_3N_4) is a metal-free semiconductor composed of carbon and nitrogen atoms arranged in a layered structure similar to graphite. Synthesized primarily through thermal polymerization of nitrogen-rich precursors like urea or melamine at 500–600°C, it forms a tri-s-triazine-based framework with alternating C–N bonds [58, 59] shown in Figure 2.3. The material exhibits a bandgap of ~2.7 eV, enabling visible-light absorption up to 460 nm, and demonstrates high thermal stability (up to 600°C), making it suitable for harsh photocatalytic environments [58-60].

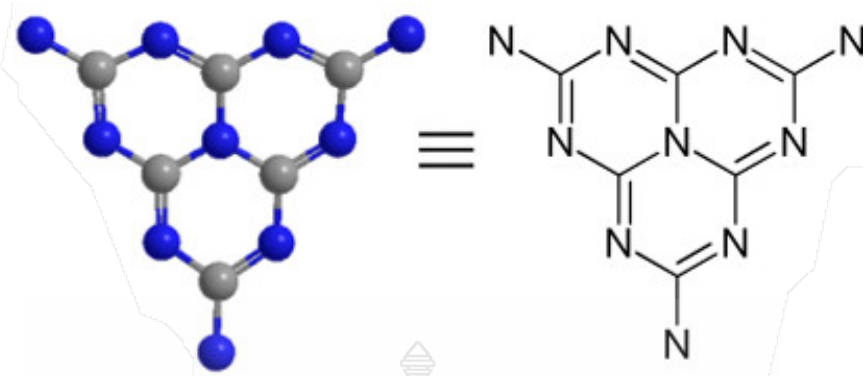

Figure 2.3 Structure of g-C_3N_4 [61]

g-C_3N_4's polymeric structure consists of tris-triazine units connected via tertiary amines, creating a porous morphology [59]. Synthesis methods include direct thermal condensation of precursors like melamine, which produces a bulk material with a high degree of polymerization [58]. The process can be modified to achieve varying textural structures, such as nanosheets or hollow rods, through templating or doping techniques [62].

The material's electronic structure allows for visible-light-driven applications, though its efficacy is limited by rapid electron-hole recombination [60]. Heterojunction formation with other semiconductors, such as TiO_2 or Ag_3PO_4, enhances charge separation and light utilization. For example, a Z-scheme heterojunction in TiO_2/g-C_3N_4 composites improves photocatalytic CO_2 reduction by promoting electron transfer [63, 64].

g-C_3N_4 exhibits a hexagonal lattice structure (space group P6m2) with interlayer distances of 0.326 nm, confirmed by XRD peaks at 27.4° (002 plane) and 13.1° (100 plane). Porous variants synthesized using citric acid as a template show increased surface area (13.975 m^2/g vs. 9.163 m^2/g for bulk) and smaller crystallite sizes (~43.5 nm) [65]. SEM reveals irregular tissue-like morphologies in doped samples, while TEM confirms ultrathin nanosheets with abundant edge sites for catalytic reactions [34, 66].

The material's band structure comprises a highest occupied molecular orbital (HOMO) at +1.6 eV and a lowest unoccupied molecular orbital (LUMO) at -1.1 eV, facilitating redox reactions. Photoluminescence spectroscopy indicates suppressed

electron-hole recombination in heterojunctions like g-C_3N_4/ZnS, where a Z-scheme mechanism preserves redox potentials [67]. UV-vis diffuse reflectance spectra show absorption edges redshifted to 650 nm in Fe^{3+}-doped samples, enabling near-infrared activity [34, 68]. Properties of g-C_3N_4 are shown in Table 2.2

Table 2.2 Properties of g-C_3N_4

Properties	Details	References
Crystal Structure	Hexagonal (P6m2), interlayer distance 0.326 nm	[34, 66]
Bandgap	2.7 eV (tenable to 1.5 eV via doping)	[34, 66, 67]
Surface Area	9.163–13.975 m^2/g (porous vs. bulk)	[65]
Thermal Stability	Stable up to 600°C	[66]

2.1.5 $MnFe_2O_4$/g-C_3N_4 Heterojunction Composites

$MnFe_2O_4$/ g-C_3N_4 composites integrate the visible-light absorption of g-C_3N_4 (bandgap ~2.7 eV) with the magnetic properties of $MnFe_2O_4$, enabling efficient pollutant degradation and catalyst recovery [69, 70]. The cubic spinel structure of $MnFe_2O_4$ (lattice parameter: 8.34–9.40 Å) provides Fe^{3+}/Mn^{2+} redox pairs for hole-mediated degradation, while the g-C_3N_4 layered structure offers π-conjugated electron systems for charge transfer [71, 72]. Optimized composites achieve > 90% methylene blue degradation under visible light via hydroxyl radical (·OH) pathways [70, 73].

The composite's enhanced activity stems from a Type II heterojunction, where the conduction band (CB) of g-C_3N_4 (−1.3 eV) lies above that of $MnFe_2O_4$ (−0.5 eV), while the valence band (VB) of $MnFe_2O_4$ (+2.7 eV) resides below g-C_3N_4 (+1.4 eV) [66, 74]. Under visible light, photogenerated electrons migrate from g-C_3N_4 to $MnFe_2O_4$, while holes transfer inversely, suppressing recombination and prolonging carrier lifetimes. This mechanism facilitates the generation of reactive oxygen species (•OH, $•O_2^-$) responsible for pollutant degradation [75, 76].

$MnFe_2O_4$ incorporation grants the composite ferrimagnetic behavior, with saturation magnetization values ranging from 45–76 emu/g, enabling facile magnetic separation [74, 75]. The hybrid structure also improves thermal stability, retaining >85%

activity after five cycles due to robust interfacial bonding between $MnFe_2O_4$ nanoparticles and g-C_3N_4 nanosheets [74, 77].

- **Synthesis Methods for $MnFe_2O_4$/g-C_3N_4 Composites**

$MnFe_2O_4$/g-C_3N_4 composites are fabricated using methods that optimize interfacial bonding, crystallinity, and photocatalytic-magnetic synergy. The show is a detailed comparison in Table 2.3

Table 2.3 Synthesis Methods for $MnFe_2O_4$/g-C_3N_4 Composites.

Method	Key Steps	Advantages	Limitations	References
Hydrothermal	Precursor mixing, autoclaving (160–200°C)	High crystallinity, controlled morphology, strong interfacial bonding	Energy-intensive, long reaction times	[74, 76, 78]
Calcination	Thermal treatment (400–550°C) of precursors	Scalability, induces nitrogen doping in g-C_3N_4	Particle agglomeration, reduced surface area	[75, 79]
Co-precipitation	Fe^{3+}/Mn^{2+} salts + g-C_3N_4 in basic solution	Rapid synthesis (1–2 hours), cost-effective	Irregular particle size, weak crystallinity	[66, 80, 81]
Solid-state	Mechanical mixing + high-temperature annealing	Simple setup, avoids solvent use	Poor interfacial contact, limited scalability	[76, 82]

- **Hydrothermal synthesis of $MnFe_2O_4$/g-C_3N_4 composites**

Hydrothermal synthesis of $MnFe_2O_4$/g-C_3N_4 composites typically involves dissolving Mn^{2+} (e.g., $MnSO_4 \cdot H_2O$) and Fe^{3+} (e.g., $FeCl_3 \cdot 6H_2O$) precursors in a solvent such as ethanol-water mixtures, followed by the addition of pre-synthesized g-

C_3N_4 [72, 83]. The mixture is sonicated to ensure dispersion, then transferred to a Teflon-lined autoclave and heated at 120–180°C for 10–24 hours under autogenous pressure [72, 83, 84]. Post-synthesis, the composite is washed repeatedly with ethanol and deionized water to remove impurities, then dried at 60–80°C or freeze-dried to maintain structural integrity [85]. This method promotes the formation of $MnFe_2O_4$ nanoparticles anchored on g-C_3N_4 surfaces through hydrogen bonding or electrostatic interactions, enhancing photocatalytic and adsorption properties [72, 83]. Critical Synthesis Parameters of Hydrothermal synthesis of $MnFe_2O_4$/g-C_3N_4 composites will show in table 2.4

Table 2.4 Critical Synthesis Parameters of Hydrothermal synthesis of $MnFe_2O_4$/g-C_3N_4 composites.

Parameter	**Optimal Range**	**Impact on Properties**	**Ref.**
Temperature	120–180°C	Higher temperatures enhance crystallinity but risk g-C_3N_4 decomposition	[70, 86]
Reaction Time	12–24 hours	Prolonged durations improve heterojunction formation	[72, 87]
$MnFe_2O_4$/g-C_3N_4 Ratio	1:1 to 1:2 (w/w)	Excess g-C_3N_4 (>50%) blocks active sites on $MnFe_2O_4$	[86, 87]
pH	9–11	Alkaline conditions Favor spinel phase formation	[83, 87]

The integration of $MnFe_2O_4$ with graphitic carbon nitride (g-C_3N_4) has emerged as a promising strategy to enhance photocatalytic efficiency for both environmental remediation and energy production. This nanocomposite leverages the synergistic properties of its components, $MnFe_2O_4$ provides magnetic recoverability and visible-light absorption, while g-C_3N_4 offers a high surface area and tunable electronic structure. Together, they form a heterojunction that improves charge separation, extends light absorption, and facilitates redox reactions for pollutant degradation and hydrogen evolution [76, 78, 88]. Below, we explore the mechanistic details and reaction pathways that underpin the photocatalytic activity of $MnFe_2O_4$/g-C_3N_4 composites.

2.1.6 Mechanisms of $MnFe_2O_4$/g-C_3N_4 composites in the Photocatalytic process

Under visible-light irradiation, both $MnFe_2O_4$ and g-C_3N_4 are photoexcited, generating electron-hole pairs. As shown in equations 2.1 and 2.2

$$g-C_3N_4 + hv \rightarrow g-C_3N_4(e^-_{CB} + h^+_{VB}) \quad (2.1)$$

$$MnFe_2O_4 + hv \rightarrow MnFe_2O_4(e^-_{CB} + h^+_{VB}) \quad (2.2)$$

Electrons in the CB of g-C_3N_4 migrate to the CB of $MnFe_2O_4$, while holes in the VB of $MnFe_2O_4$ transfer to g-C_3N_4 [76, 78, 89]. This spatial separation suppresses recombination and prolongs carrier lifetimes, as confirmed by photoluminescence spectroscopy [89, 90].

Reactive Species Generation. The separated charges participate in redox reactions with adsorbed species. As shown in equations 2.3 - 2.7

- Electrons reduce dissolved O_2 to superoxide radicals ($\bullet O_2^-$) [91]

$$e^- + O_2 \rightarrow \bullet O_2^- \quad (2.3)$$

- Holes oxidize H_2O or OH^- to hydroxyl radicals ($\bullet OH$)

$$h^+ + H_2O \rightarrow \bullet OH + H^+ \quad (2.4)$$

- $\bullet O_2^-$ further reacts to form hydrogen peroxide (H_2O_2) and $\bullet OH$

$$\bullet O_2^- + 2H^+ + e^+ \rightarrow H_2O_2 + O_2 \quad (2.5)$$

- Conduction-band electrons (e^-) or $\bullet O_2^-$ react with H_2O_2

$$H_2O_2 + e^- \rightarrow \bullet OH + OH^- \quad (2.6)$$

$$H_2O_2 + \bullet O_2^- \rightarrow \bullet OH + OH^- + O_2 \quad (2.7)$$

$\bullet OH$ attacks organic pollutants (R) through hydrogen abstraction, electrophilic addition, or electron transfer. As shown in the equation 2.8

$$H_2O_2 + O_2 \rightarrow \text{Intermediates} \rightarrow CO_2 + H_2O \quad (2.8)$$

2.2 Dye

Synthetic dyes, particularly azo and anthraquinone variants, are widely used in textiles (60–70% of commercial dyes), food, and pharmaceuticals due to their cost-effectiveness and color stability [92-94]. However, approximately 80% of dye-laden industrial wastewater enters ecosystems untreated [95, 96], causing aquatic toxicity through light attenuation and oxygen depletion while accumulating in food chains. Chronic exposure links dyes like Indigo Carmine to hypertension (OR 1.45) [96] and Reactive Black 5 to mutagenicity [96, 97]. Their structural complexity hinders degradation [96, 98, 99], necessitating advanced remediation strategies like adsorption [96, 98] and enzymatic treatments [99, 100] to mitigate ecological and public health risks.

2.2.1 Types and Classification of Dyes

Dyes are categorized by origin (natural/synthetic) and chemical structure. Natural dyes, derived from plants, minerals, or microbes, are biodegradable but limited in scalability. Synthetic dyes, particularly azo variants, dominate industrial applications due to cost-effectiveness and colorfastness but pose significant environmental risks [101-103]. The classification and examples of dyes are presented in Table 2.5.

Table 2.5 Dye Classification.

Category	Subtypes	Sources/Examples	Applications	References
Natural Dyes	Plant-based	Indigofera tinctoria (indigo), madder roots	Textiles, food, cosmetics	[101, 103, 104]
	Microbial	Shewanella spp. (bacterial pigments)	Eco-friendly textile dyeing	[104, 105]
	Mineral	Iron oxide, titanium dioxide	Paints , coatings	[103, 104]
Synthetic Dyes	Azo (mono-, di-, trisazo)	Reactive Black 5, C.I. Acid Green 19	Textiles, leather, plastics	[102, 105, 106]
	Anthraquinone	Indigo Carmine (C.I. 73015)	Food, pharmaceuticals , textiles	[106, 107]
	Triphenylmethane	Malachite green	Paper, ink	[106, 108]

2.2.2 Environmental and Health Impacts

Dye-containing wastewater contaminates aquatic ecosystems, inhibits photosynthesis, and bioaccumulates in food chains. Synthetic dyes like RB5 and IC are linked to carcinogenicity, mutagenicity, and endocrine disruption. The impact of dyes on health and the environment [106, 108, 109]. The impact of dyes on health and the environment is presented in Table 2.6.

Table 2.6 The impact of dyes on health and the environment.

Impact Type	Description	References
Aquatic Toxicity	Reduces dissolved oxygen, blocks sunlight penetration, harms aquatic organisms	[106, 108, 110]
Human Health	Carcinogenic (e.g., benzidine in azo dyes), allergic dermatitis, organ damage	[106, 107, 109]
Soil Contamination	Accumulates in agricultural soils, impairing plant growth and microbial activity	[106, 110]
Persistent Pollution	Non-biodegradable azo dyes persist in water, requiring advanced remediation	[105, 106, 108]

2.2.3 Indigo Carmine (IC)

Indigo Carmine ($C_{16}H_8N_2Na_2O_8S_2$) is a disodium salt derived from the sulfonation of indigo, a naturally occurring dye originally extracted from plants like Indigofera tinctoria [107]. Its molecular structure (Figure 2.4) features a conjugated chromophore system comprising two indole rings linked by a central double bond, with sulfonate ($-SO_3^-$) groups at the 5 and 5′ positions (Table 1). These sulfonate groups enhance water solubility, making IC suitable for aqueous applications, while the chromophore confers its characteristic blue-violet hue, which is pH-dependent [107]. Molecular properties of Indigo Carmine show in table 2.7

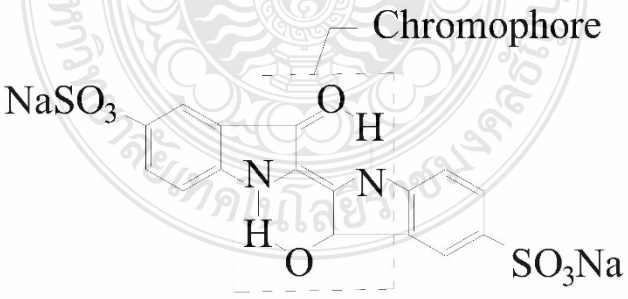

Figure 2.4 Indigo Carmine structure.

Table 2.7 Molecular properties of Indigo Carmine.

Property	Value
Molecular formula	$C_{16}H_8N_2Na_2O_8S_2$
Molecular weight	466.36 g/mol
Chromophore system	Conjugated indole rings
Functional groups	Sulfonate ($-SO_3^-$), carbonyl
CAS number	860-22-0

- **Physical Characteristics of IC**

IC is a dark blue crystalline powder with a melting point exceeding 300°C, indicative of its thermal stability. It exhibits limited solubility in organic solvents like ethanol but dissolves readily in water (10 g/L at 25°C), forming a blue solution that shifts to green-yellow under alkaline conditions [107]. Its light absorption maxima at 608–612 nm facilitate spectrophotometric detection in environmental and industrial samples [107].

- **Chemical Reactivity of IC**

IC's chemical stability is influenced by pH, oxidizing agents, and reducing environments. In acidic media (pH < 3), the dye remains stable, but alkaline conditions (pH > 8) trigger hydrolysis, leading to color fading [107]. The chromophore's conjugated system is susceptible to oxidation, particularly by ozone and hydroxyl radicals, which break the double bonds and degrade the aromatic structure [111, 112]. However, the sulfonate groups resist complete mineralization, often leaving residual sulfonic acid derivatives in treated water [112].

2.2.4 Reactive Black 5 Dye (RB5)

Reactive Black 5 (RB5) is a diazo dye characterized by the molecular formula $C_{26}H_{21}N_5Na_4O_{19}S_6$ (Figure 2.5)and a molecular weight of 991.82 g/mol. Its structure comprises two azo (-N=N-) groups linked to naphthalene and benzene rings, with sulfonic acid ($-SO_3H$) substituents enhancing water solubility. The chromophoric system, responsible for its intense black color, exhibits a maximum absorbance (λmax) at 599 nm in aqueous solutions [113]. This structural complexity contributes to RB5's

resistance to conventional degradation methods, necessitating advanced treatment approaches. Molecular properties of RB5 are shown in Table 2.8

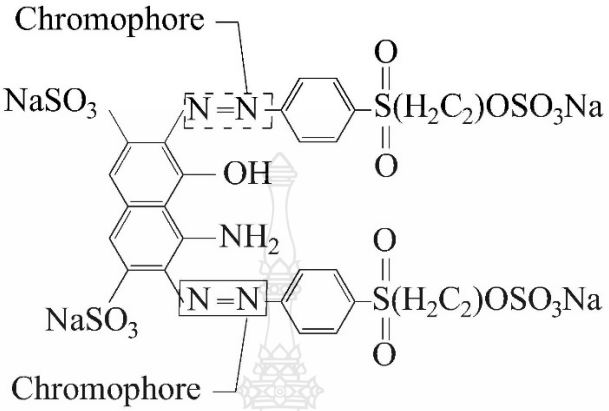

Figure 2.5 Reactive Black 5 structure.

Table 2.8 Molecular properties of RB5.

Property	Value
Molecular formula	$C_{26}H_{21}N_5Na_4O_{19}S_6$
Molecular weight	991.82 g/mol
Chromophore system	Azo group (-N=N-) with extended conjugation
Functional groups	Azo group, sulfonate groups (-SO_3H), chlorine atoms (Cl)

- **Physical Characteristics of RB5**

RB5 exists as a dark blue to black crystalline powder with a melting point exceeding 300°C, indicative of high thermal stability. It dissolves readily in water (up to 582 g/L at 22°C), forming solutions that appear blue-black at neutral pH but shift to green-yellow under alkaline conditions due to hydrolysis of the sulfonate groups. The dye's molar extinction coefficient exceeds 28,000 $L \cdot mol^{-1} \cdot cm^{-1}$, enabling sensitive spectrophotometric detection.

- **Chemical Reactivity of RB5**

RB5's chemical stability is pH-dependent. Under acidic conditions (pH < 3), the dye remains intact, but alkaline environments (pH > 8) trigger hydrolysis, leading to color loss. The azo bonds are prone to reduction by agents like zerovalent iron (ZVI), breaking the chromophore into aromatic amines. Oxidation via hydroxyl radicals (•OH) or ozone (O_3) cleaves the conjugated system, generating intermediates such as naphthalene sulfonic acids.

2.3 Tetracycline

TC enters ecosystems primarily through incomplete metabolism in humans/animals (25–75% excretion rate) [114], agricultural runoff from manure-fertilized fields[114], and inefficient removal in conventional wastewater treatment plants (WWTPs)[115]. Residual concentrations in surface waters range from <0.11 mg/L to 6.8 mg/L, with higher levels near pharmaceutical industries [114]. Soil adsorption coefficients (Kd = 70–5000 L/kg) limit its mobility but enable long-term accumulation in agricultural topsoil [114, 116].

Tetracycline's chemical formula is $C_{22}H_{24}N_2O_8$, with a molar mass of 444.440 g/mol. It crystallizes as a bright yellow, amphoteric powder that fluoresces under ultraviolet light. The molecule contains four linearly fused benzene rings (A–D), a dimethylamine group at C4, and a tricarbonyl system spanning C1–C3 [117].

2.4 Characterization techniques

2.4.1 Photoluminescence (PL)

Photoluminescence (PL) spectroscopy is a non-destructive analytical technique used to study electronic transitions and defect states in photocatalytic materials. When a material absorbs photons, electrons are excited to higher energy states, and their subsequent radiative recombination emits light, which is detected as PL. This emission spectrum provides insights into bandgap structures, defect-mediated recombination, and charge carrier dynamics [118, 119]. Time-correlated single-photon counting (TCSPC) further enables lifetime analysis, distinguishing radiative recombination processes across

picosecond-to-second timescales. Such capabilities are indispensable for characterizing defects, bandgap transitions, and electron-hole recombination pathways in semiconductors like g-C_3N_4 and transition metal oxides [66, 118, 120].

2.4.1 X-ray Diffraction (XRD) [121]

X-ray diffraction (XRD) is a cornerstone technique for analyzing the crystallographic structure and phase composition of nanomaterials. When X-rays interact with a crystalline material, constructive interference occurs at specific angles determined by Bragg's law in equation 2.9

$$n\lambda = 2d\sin\theta \quad (2.9)$$

where

λ is the X-ray wavelength (nm).

d is the interplanar spacing (nm).

θ is the diffraction angle (degree, °).

For nanoparticles, peak broadening in XRD patterns inversely correlates with crystallite size due to the Scherrer equation 2.10

$$L = K\lambda/\beta\cos\theta \quad (2.10)$$

where

L is the crystallite size (nm).

K is a shape factor (~0.9).

β is the full width at half maximum (FWHM) (radian, rad).

Crystallites below 10 nm exhibit significant broadening, complicating phase identification, while those under 5 nm may produce undetectable signals. Modern XRD systems, such as the Rigaku Smart Lab, enable in situ studies of structural changes under thermal stress (up to 1500°C) and small-angle X-ray scattering (SAXS) for pore size distribution analysis. For example, XRD confirmed the anisotropic growth of

wurtzite CoS nanoplates by correlating peak broadening differences between {h00} and {00l} planes with crystallite dimensions.

2.4.2 X-ray Photoelectron Spectroscopy (XPS) [122].

XPS provides nanoscale surface chemical analysis by measuring the kinetic energy of photoelectrons ejected from a material irradiated with X-rays. The binding energy (E_b) of these electrons is element-specific and sensitive to the chemical environment to equation 2.11

$$E_b = h\nu - E_k - \phi \quad (2.11)$$

where

$h\nu$ is the photon energy (eV).

E_k is the electron kinetic energy (eV).

ϕ is the spectrometer work function (eV).

With a penetration depth of ~10 nm, XPS identifies surface composition, oxidation states, and coating thickness. For instance, Fe^{3+}-modified biochar showed enhanced tetracycline adsorption due to surface hydroxyl and carboxyl groups, as validated by O 1s and C 1s spectra. However, XPS requires ultra-high vacuum and dry, contamination-free samples, limiting its applicability to in situ liquid-phase systems.

2.4.3 Fourier transform infrared spectroscopy (FT-IR)

FT-IR spectroscopy probes molecular vibrations to identify functional groups and chemical bonds in nanomaterials. The absorption intensity follows the Beer-Lambert law shown in equation 2.12

$$A=\epsilon cl \quad (2.12)$$

where

A is absorbance (au),

ϵ is molar absorptivity ($L.mol^{-1}$),

c is concentration (mol/L).

l is path length (cm).

Recent advances include infrared reflection anisotropy spectroscopy for semiconductor surface analysis and attenuated total reflectance (ATR) modes for in situ degradation studies. For example, FT-IR detected ketoprofen methyl ester artifacts in GC-MS analyses of horse urine, revealing alkaline liquid-liquid extraction-induced esterification.

2.4.4 Transmission electron microscopy (TEM)

TEM combines high-resolution imaging (<0.1 nm) with elemental analysis via energy-dispersive X-ray spectroscopy (EDS) and electron energy-loss spectroscopy (EELS). Aberration-corrected TEM achieves atomic-scale resolution, as demonstrated in Pt-Co core-shell nanoparticles, where interfacial strain enhances oxygen reduction activity. In situ TEM tracks dynamic processes like lithiation in SnO_2 nanowires, revealing fracture mechanisms during battery cycling. Dark-field TEM imaging of Co nanoparticles in Y-zeolites resolved sub-1 nm clusters, while electron tomography reconstructed 3D atomic arrangements in gold nanocrystals. However, electron beam-induced damage remains a challenge, particularly for organic-inorganic hybrids.

2.4.5 UV-Vis Diffuse Reflectance Spectroscopy (UV-Vis DRS)

UV-Vis Diffuse Reflectance Spectroscopy (UV-Vis DRS) is a non-destructive analytical technique widely employed to characterize the optical properties of solid-phase materials, particularly semiconductors and photocatalysts [123]. Unlike conventional UV-Vis absorption spectroscopy, which measures transmitted light through a sample, DRS quantifies the diffuse reflection of light from powdered or bulk materials. This method is especially advantageous for studying heterogeneous catalysts like

$MnFe_2O_4$@g-C_3N_4 composites, as it avoids the complexities of sample preparation required for transmission-based analyses [124].

The fundamental theory underlying DRS is the Kubelka-Munk (K-M) model, which relates the diffuse reflectance (R_∞) to the absorption coefficient (K) and scattering coefficient (S) of the material. The Kubelka-Munk function is expressed as equation 2.12.

$$F(R_\infty) = \frac{(1-R_\infty)^2}{2R_\infty} = \frac{K}{S} \quad (2.12)$$

$F(R_\infty)$ is proportional to the absorption coefficient (α) for weakly absorbing materials. This transformation allows the conversion of reflectance data into absorption-like spectra, enabling direct comparison with traditional absorption measurements.

The optical bandgap (E_g) of a semiconductor is a critical parameter governing its light-harvesting capabilities and photocatalytic activity. For $MnFe_2O_4$@g-C_3N_4 composites, which exhibit indirect allowed electronic transitions, the Tauc plot method is employed to estimate Eg. The Tauc equation for indirect bandgap materials is given by equation 2.13.

$$(\alpha h\nu)^{1/2} = A(h\nu - E_g) \quad (2.13)$$

where:

α = absorption coefficient (derived from $F(R_\infty)$) (cm^{-1}).

$h\nu$ = photon energy (eV).

A = proportionality constant ($cm^{-1}.eV^{-1}$).

E_g = optical bandgap energy (eV).

For direct bandgap materials, the exponent n = 1/2, whereas n = 2 is used for indirect transitions. The intersection of the linear extrapolation of the $(\alpha h\nu)1/2$ vs. $h\nu$ plot with the x-axis provides the E_g value [125].

2.4.6 Gas Chromatography-Mass Spectrometry (GC-MS)

GC-MS separates and identifies volatile compounds via retention time and mass-to-charge (m/z) ratios. In nanomaterials, it detects residual solvents or degradation products. For example, GC-MS revealed ketoprofen methyl ester formation during alkaline extraction of horse urine, highlighting pH-dependent artifact generation. Coupled with thermal desorption, GC-MS analyzed tetracycline decomposition byproducts in soil, achieving 98% degradation at 300°C

2.5 Kinetics of Photocatalytic Reactions.

The photocatalytic kinetics of $MnFe_2O_4$/g-C_3N_4 composites are governed by complex interfacial charge transfer processes, reactive oxygen species (ROS) generation dynamics, and adsorption-desorption equilibria at the catalyst surface. These heterojunction systems exhibit reaction rates influenced by multiple operational parameters, including catalyst loading, oxidant concentration, light intensity, and pollutant molecular structure, often following pseudo-first-order kinetics with rate constants modulated by synergistic heterojunction effects [76, 126].

2.5.1 Pseudo-First-Order Reaction Dynamics

The degradation of organic pollutants over $MnFe_2O_4$/g-C_3N_4 composites typically adheres to pseudo-first-order kinetics, expressed as equation 2.13

$$\ln(C_0 / C) = k_{obs} t \quad (2.13)$$

where k_{obs} represents the apparent rate constant. For steroid hormone degradation, k_{obs} values reach 62×10^3 min^{-1} under $MnFe_2O_4$/g-C_3N_4/peroxymonosulfate (PMS)/visible light systems, significantly exceeding those of standalone PMS activation. This enhancement arises from dual activation pathways. photogenerated electrons from the heterojunction directly reduce PMS, while Fe^{2+}/Mn^{2+} ions catalyze PMS decomposition via radical-mediated pathways. The synergy between photocatalysis and PMS activation produces a synergistic index (SI) of 19.39, calculated as equation 2.14, confirming non-additive performance enhancement.

$$SI = k_{dual} / (k_{photo} + k_{PMS}) \quad (2.14)$$

2.5.2 Langmuir-Hinshelwood Considerations.

While adsorption capacity influences initial reaction rates, the Langmuir-Hinshelwood model often inadequately describes $MnFe_2O_4$/g-C_3N_4 systems due to rapid ROS diffusion into bulk solution. The composites' high surface area (55.8 m^2/g) and mesoporous structure enable rapid pollutant adsorption, but degradation kinetics remain dominated by radical-mediated oxidation rather than surface-bound reactions[126, 127]. For carbamazepine degradation, adsorption accounts for <15% of total removal, with pseudo-first-order models providing better fits ($R^2 > 0.98$) than Langmuir-Hinshelwood [82, 126]. Langmuir-Hinshelwood Rate Equation For a general reaction involving two reactants A and B that exhibits the following equation 2.15

$$A + B \underset{k2}{\overset{k1}{\longrightarrow}} \text{Products} \tag{2.15}$$

The rate of reaction r can be expressed as equation 2.16

$$r = \frac{\boldsymbol{2}K_A K_B[A][B]}{k(\boldsymbol{1} + K_A[A] + K_B[B])} \tag{2.16}$$

Where

r = rate of reaction (mol.L^{-1}.s^{-1})**.**

k = rate constant (mol.L^{-1}.s^{-1})**.**

K_A = adsorption coefficient of reactant A (L.mol^{-1})**.**

K_B = adsorption coefficient of reactant B (L.mol^{-1})**.**

[A] = concentration of A (mol/L)**.**

[B] = concentration of B (mol/L)**.**

CHAPTER 3

RESEARCH METHODOLOGY

3.1 Chemicals and Instruments

3.1.1 Chemicals

1) Iron (II) Sulfate 7 Hydrate ($FeSO_4.7H_2O$) 99% QREC-Grade AR
2) Manganese (II) Sulfate Monohydrate ($MnSO_4.H_2O$) 99% QREC-Grade AR
3) Graphitic Carbon Nitride (g-C_3N_4)
4) Ethylene Glycol 99.9% Lab grade
5) Sodium Hydroxide Pellets (NaOH) 99% QREC-Grade AR
6) Methyl Alcohol Anhydrous (CH_3OH) MACRON-Grade GC
7) Indigo Carmine ($C_{16}H_8N_2Na_2O_8S_2$) HIMEDIA-Grade AR
8) Reactive Black 5
9) Tetracycline Capsules 500 mg

3.1.2 Instruments

1) Beakers (25, 50, 125, 500, and 1,000 mL)
2) Burette (50 mL)
3) Centrifuge tube (50 mL)
4) Erlenmeyer flask (250 mL)
5) Glass sampling bottle (25 mL)
6) Measuring cylinders (25 and 100 mL)
7) Nylon syringe filter (0.2 micron, FILTREX brand)
8) Stirring rod
9) Syringe (5 mL)
10) Volumetric flasks (10, 25, 50, 100, 500, and 1,000 mL)

3.1.3 Technical Equipment

1) ADMI Spectrophotometer (Spectoquant Prove 300)
2) Fourier Transform Infrared Spectroscopy (FT-IR)
3) Hot Air Oven (Model UF 75 Memmert)
4) Hydrothermal Synthesis Autoclave Reactor PTFE lined (250 mL)

5) Magnetic Stirrer and Magnetic Bar

6) Photocatalytic Reactor (The setup of the photocatalytic reactor is presented in Figure 3.1.)

7) Photo Luminescence (PL)

8) Scanning Electron Microscopy with Energy Dispersive X-ray Spectroscopy (SEM-EDS)

9) Sonicator bath

10) Spectrophotometer (Single Monochrome Type U-3900)

11) Transmission Electron Microscopy (TEM)

12) UV-Visible Diffuse Reflectance Spectroscopy (UV-Vis/DRS)

13) X-ray Photoelectron Spectroscopy (XPS)

14) X-ray Diffraction (XRD)

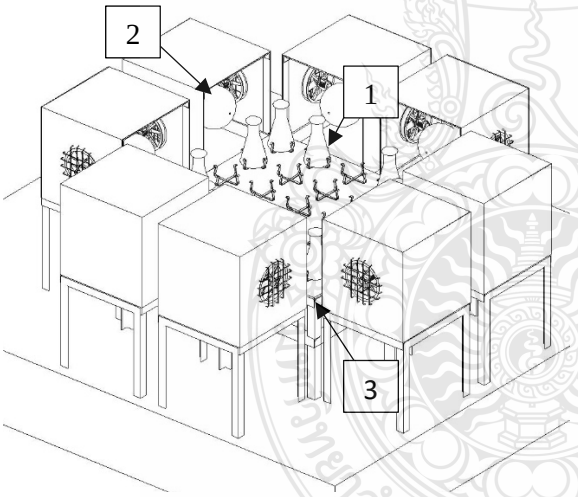

1. Erlenmeyer flask 250 mL
2. UVA light source
3. Shaker

Figure 3.1 depicts the photocatalytic reactor used in the experiments

3.2 Preparation photocatalyst

3.2.1 Preparation of MnF photocatalyst

The MnF photocatalyst was synthesized through a hydrothermal method. Initially, 1 mmol of $MnSO_4.H_2O$ was dissolved in 50 mL of deionized water and 50 mL of ethylene glycol, and 2 mmol of $FeSO_4.7H_2O$ was dissolved in same manner. After stirring for 30 minutes the two solutions were mixed with stirring at room temperature for 1 hour after that NaOH solution was added until reaching a pH of 9. Subsequently, this resulting mixture was moved to an autoclave and heated at 160 °C for 20 hours. Upon completion, the resulting samples were washed with DI water and ethanol, then the product was wiped at 80 °C for 12 hours, yielding $MnFe_2O_4$ nanoparticles.

3.2.2 Preparation of MnFG1, MnFG2, and MnFG3 photocatalyst

In the preparation of the composite catalysts for the experiment, a total of three types will be prepared MnFG1, MnFG2, and MnFG3.with the following preparation methods. MnFG1 photocatalyst was fabricated by a hydrothermal method. Initially, 1 g of g-C_3N_4 was dispersed in 30 mL of DI water with ultrasonic dispersion for 30 minutes. Simultaneously, 1 mmol of $MnSO_4.H_2O$ was dissolved in 50 mL of DI water and 50 mL of ethylene glycol, and 2 mmol of $FeSO_4.7H_2O$ was dissolved in 50 mL of DI water and 50 mL of ethylene glycol. After stirring for 30 minutes, the two solutions were mixed under continuous stirring at room temperature for 1 hour. After that, NaOH solution was added until the pH reached 9. Afterward, the g-C_3N_4 was added to the above solution and stirred for 2 hours. Finally, this resulting mixture was transferred to an autoclave and heated at 160 °C for 20 hours. Upon completion, the resulting samples were washed using ethanol and DI water, then the product was dried at 80 ℃ for 12 hours to yield a fine powder of the MnFG1 Nanocomposite. To prepare MnFG2 and MnFG3, the same procedure was repeated with increased amounts of g-C_3N_4 to 2 g and 3 g, respectively.

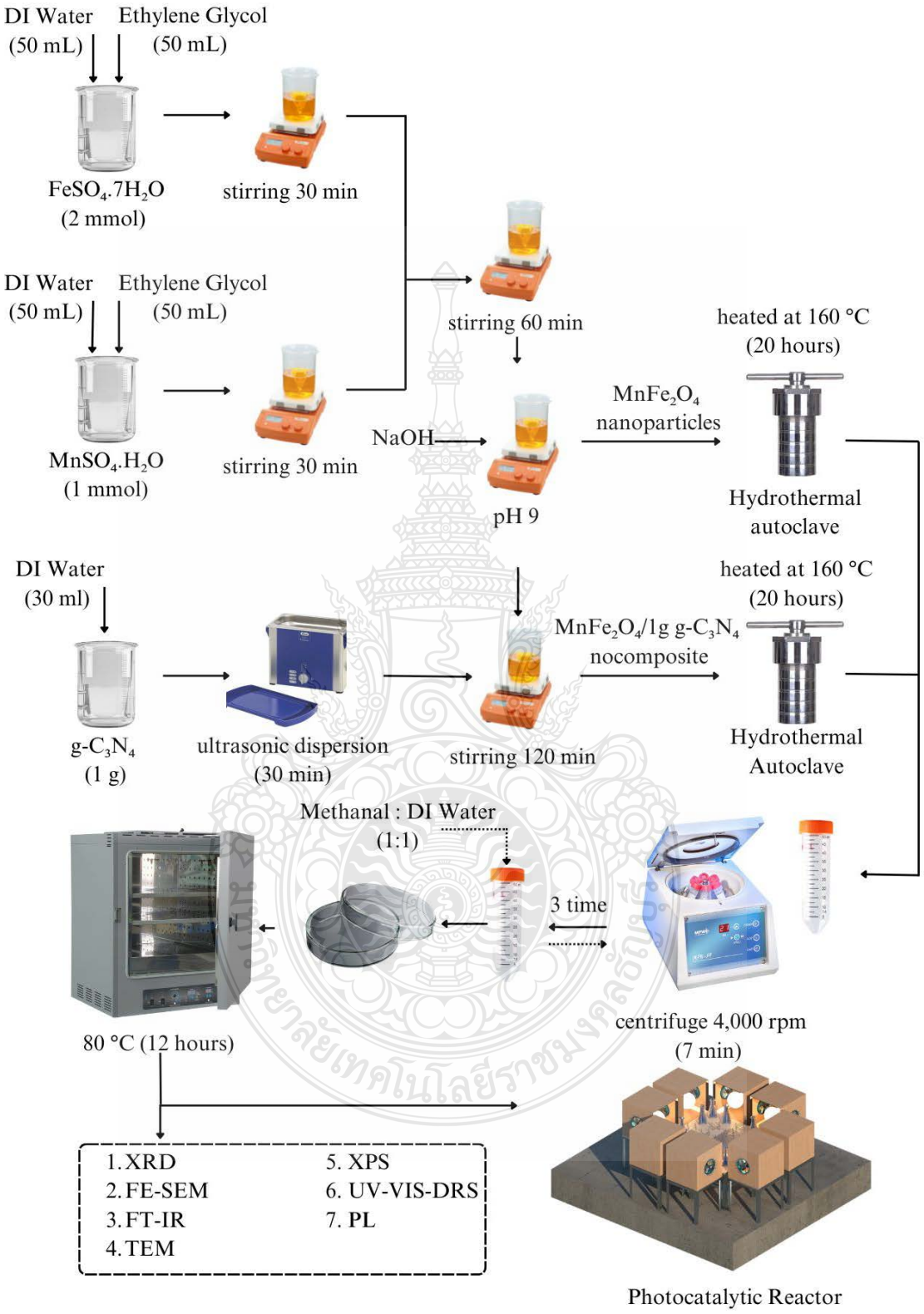

Figure 3.2 Preparation of MnF and MnFG1.

3.3 Physical properties characterization of photocatalysts

The physical properties of the synthesized photocatalysts were analyzed using a range of analytical instruments, as detailed in Table 3.1.

Table 3.1 Analysis of photocatalyst properties with scientific analysis methods

Analysis techniques	Instrument	Physical properties of the synthesized photocatalysts
XRD	Model Smart Lab	Phase characterization, mechanism of the photocatalyst, effects of doping or structural.
SEM	JEOL JSM-7610F, Oxford X-Max 20	The morphologies of photocatalyst.
FT-IR	PerkinElmer Spectrum Two	Molecular structure identification.
XPS	Model AXIS Ultra DLD	Surface composition, chemical state, and electronic properties of the photocatalyst.
TEM	Model TECNAI 20	Particle size, internal structure, and composition.
UV-vis DRS	Model GC6890N-MS5973N	Absorption and Bandgap.
Photo Luminescence	HORIBA Scientific, model: FLUOROMAX PLUS	charge carrier dynamics, energy levels, and reaction pathways

3.4 Prepare synthetic wastewater with contaminants

The synthetic wastewater used in this research was prepared from two groups of contaminants, comprising a total of four types, as outlined below:

3.4.1 Synthetic dye wastewater

- Synthetic dye wastewater with IC was prepared by dissolving 50 mg of IC dye in 1,000 mL of deionized water to obtain a 50 ppm solution.
- Synthetic dye wastewater with RB5 was prepared by dissolving 50 mg of RB5 dye in 1,000 mL of deionized water to achieve a 50 ppm concentration.
- Synthetic dye wastewater containing mixed dyes was prepared by dissolving 50 mg each of IC and RB5 dyes in 1,000 mL of deionized water.

3.4.2 Synthetic wastewater containing pharmaceutical contaminant

Dissolve 50 mg of tetracycline (TC) powder in 1,000 mL of deionized water and mix thoroughly until fully dissolved.

3.5 Photocatalytic Treatment Procedure

3.5.1 Transfer 100 mL of synthetic wastewater to a 250 mL Erlenmeyer flask.

3.5.2 Add the photocatalyst into the synthetic wastewater.

3.5.3 Mix thoroughly to ensure uniform distribution of the photocatalyst. Batch reactors perform the photosensitizer using UVA light with an intensity of 1,250 $\mu W.cm^{-2}$.

3.5.4 Collect treated wastewater samples from the experiment at 0, 10, 20, 30, 40, 60, 90, 120, 150,and 180 min. (Figure 3.3)

3.5.5 Analyze the contaminant concentrations in each sample using UV-Vis spectrophotometry. The maximum absorption for each contaminant was identified, with the wavelength scan ranging between 400 and 700 nm.

3.5.6 The color analysis quantifies the concentration of colored contaminants in wastewater using an ADMI Spectrophotometer.

3.5.7 Analyze the molecular structure of each contaminant to evaluate its decomposition using GC-MS equipment.

The selection of experiments aimed at analyzing the most effective wastewater treatment methods for removing contaminants from synthetic wastewater was conducted. Various treatment methods for synthetic wastewater were analyzed and compared under different experimental conditions, as specified in Table 3.2.

Table 3.2 Experimental conditions for treating synthetic wastewater contaminants using different types of photocatalysts were established.

Experiment	Catalyst	UVA
1	✖	✖
2	✖	✓
3	✓	✖
4	✓	✓

3.6 Kinetics of Photocatalytic Reactions

The kinetics of contaminants in synthetic wastewater were studied using two groups of contaminants, through the photocatalytic process using prepared photocatalyst. The study found that the appropriate kinetic model that can explain the mechanism of the photocatalytic reaction.

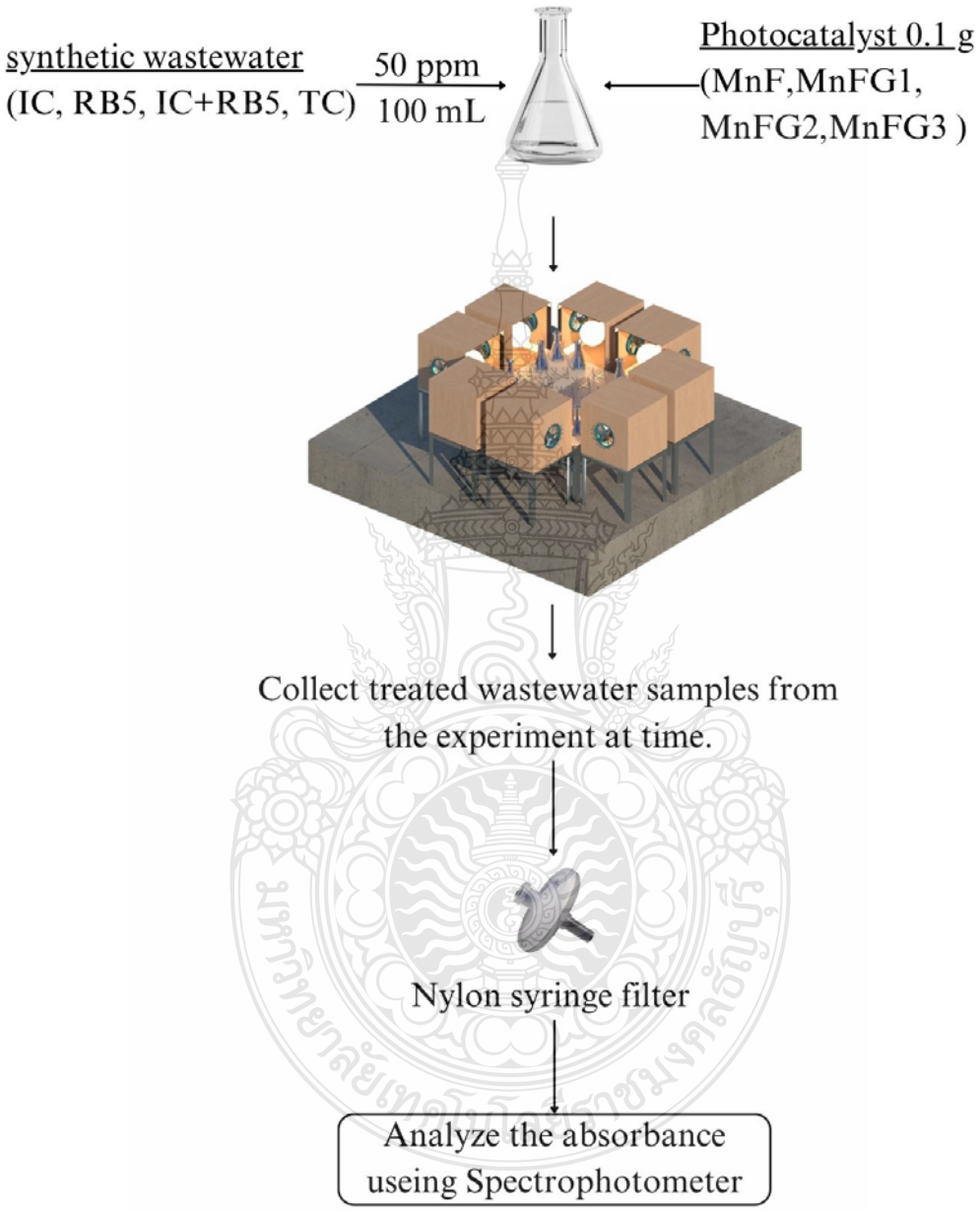

Figure 3.3 Photocatalytic Treatment Procedure.

CHAPTER 4

RESULTS AND DISCUSSION

4.1 Physical, and Chemical Properties

Chapter 4: Structural and chemical characterization of prepared samples This chapter presents a comprehensive discussion on the physical and chemical properties of the synthesized catalysts. Various characterization techniques, including X-ray diffraction (XRD), field emission scanning electron microscopy (FE-SEM), X-ray photoelectron spectroscopy (XPS), transmission electron microscopy (TEM), UV-Vis diffuse reflectance spectroscopy (UV-Vis DRS), and photoluminescence spectroscopy (PL) were employed to analyze the crystal structure, morphology, elemental composition, oxidation states, and binding energies of the prepared catalysts.

4.1.2 XRD Analysis

The crystalline structure and phase purity of the synthesized catalysts were investigated using X-ray diffraction analysis. Figure 4.2 presents the XRD patterns of all prepared catalysts, including pure manganese ferrite ($MnFe_2O_4$) and its composites with graphitic carbon nitride (g-C_3N_4). The prepared catalysts are denoted as follows: pure $MnFe_2O_4$ as MnF, (1) g-C_3N_4/$MnFe_2O_4$ as MnFG1, (2) g-C_3N_4/$MnFe_2O_4$ as MnFG2, and (3) g-C_3N_4/$MnFe_2O_4$ as MnFG3.

Figure 4.2(a) confirms the formation of pure $MnFe_2O_4$ spinel ferrite. The characteristic diffraction peaks of $MnFe_2O_4$ appear at 2θ values of 30.09°, 35.53°, 37.12°, 43.18°, 53.92°, 57.10°, and 62.65°, corresponding to the (220), (311), (222), (400), (422), (511), and (440) crystal planes, respectively. These diffraction peaks confirm the cubic spinel structure of $MnFe_2O_4$ and are in good agreement with the standard JCPDS card No. 74-2403 [133]. The average crystallite size of $MnFe_2O_4$ spinel ferrite nanoparticles was determined using the Scherrer equation:

$$d = k\lambda/\beta cos\theta \quad (4.1)$$

Where K is 0.9 is the X-ray wavelength, is the full width at half maximum (FWHM) of the (311) diffraction peak, and is the Bragg diffraction angle. The average crystallite size of the prepared $MnFe_2O_4$ nanoparticles was found to be approximately 18 nm. Figures 4.2(b-d) illustrate the XRD patterns of graphitic carbon nitride (g-C_3N_4) composites with $MnFe_2O_4$ at varying compositions. The diffraction peaks corresponding to g-C_3N_4 are observed at 2θ values of 14.16° and 27.64°, which are assigned to the (111) and (002) crystal planes, respectively [134]. These peaks confirm the successful incorporation of g-C_3N_4, as validated by previous literature. Notably, as the percentage of g-C_3N_4 increases, the intensity of the diffraction peaks also increases, indicating enhanced crystallinity. The average crystallite size of g-C_3N_4 ranges between 13 and 15 nm. Interestingly, the crystallite size decreases with an increasing percentage of g-C_3N_4 in the composite, suggesting that the introduction of graphitic carbon nitride influences the structural properties of the $MnFe_2O_4$ phase.

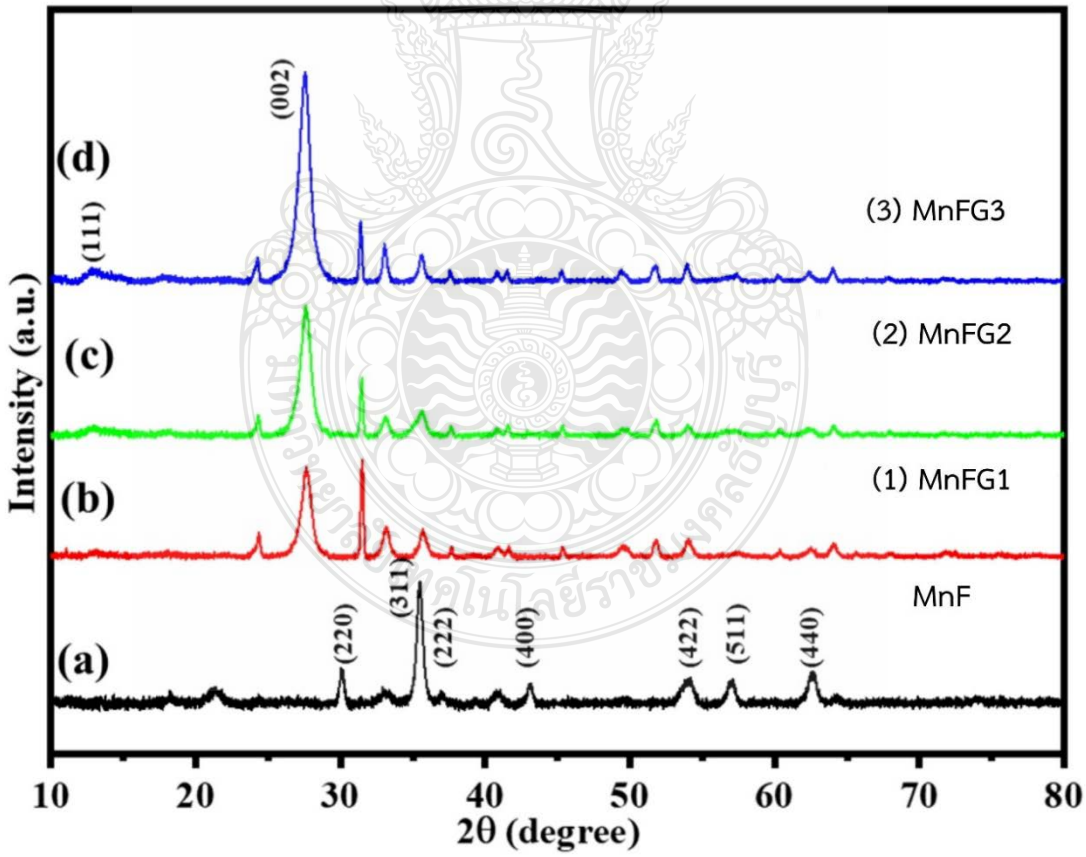

Figure 4.1 XRD analysis of prepared spinel ferrite composites, (a) MnF, (b) MnFG1, (c) MnFG2, and (d) MnFG3

Overall, the XRD analysis confirms the phase purity, crystal structure, and crystallite size of the prepared materials. The successful integration of spinel ferrite with graphitic carbon nitride enhances the material's potential as an efficient photocatalyst. This composite material exhibits promising applications in dye degradation and wastewater treatment, highlighting its significance in environmental remediation.

4.1.2 FE-SEM Analysis

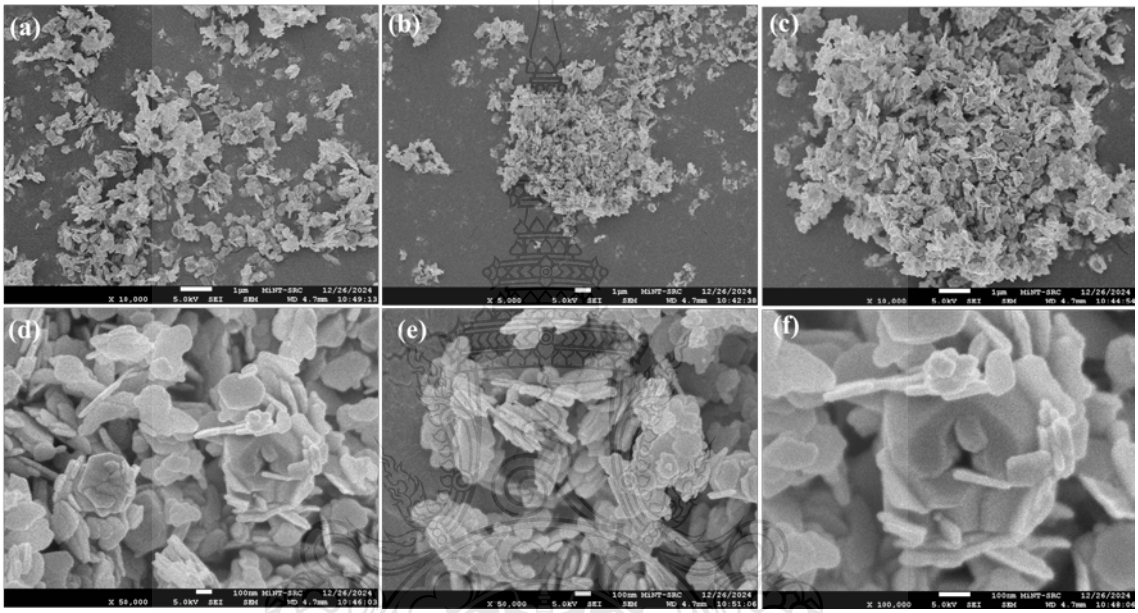

Figure 4.2 SEM analysis of MnF catalyst, (a-f) SEM images at different magnifications.

The morphology and size of the synthesized MnF photocatalysts were analyzed using field emission scanning electron microscopy (FE-SEM), as shown in Figure 4.2. Figure 2 (a-f) presents FE-SEM images at different magnifications, ranging from the micro-scale to the nano-scale. These images reveal that the synthesized MnF exhibits a nanoplate-like morphology with irregular shapes. Such morphological characteristics contribute to a higher surface area and enhanced surface activity, which is crucial for improved photocatalytic performance.

Furthermore, the morphology of all composite samples was examined using FE-SEM, with the results displayed in Figure 4.3. Figure 4.3 (a-d) shows the FE-SEM images of the MnFG1 composite, indicating that while both g-C_3N_4 and $MnFe_2O_4$ are

present, their distribution is not uniform. In particular, g-C_3N_4 is only partially covered by the MnF photocatalyst, with some MnF particles combining with g-C_3N_4 and others remaining separate. This suggests that the composite formation is relatively weak, leading to a less effective material for photocatalytic applications.

Figure 4.3(e-h) presents FE-SEM images of the MnFG2 composite at different magnifications. These images demonstrate that g-C_3N_4 and MnF are well-integrated, forming a homogeneously distributed composite. Compared to MnFG1, the MnFG2 composite exhibits a significantly improved blending of the two components, which is expected to enhance photocatalytic efficiency.

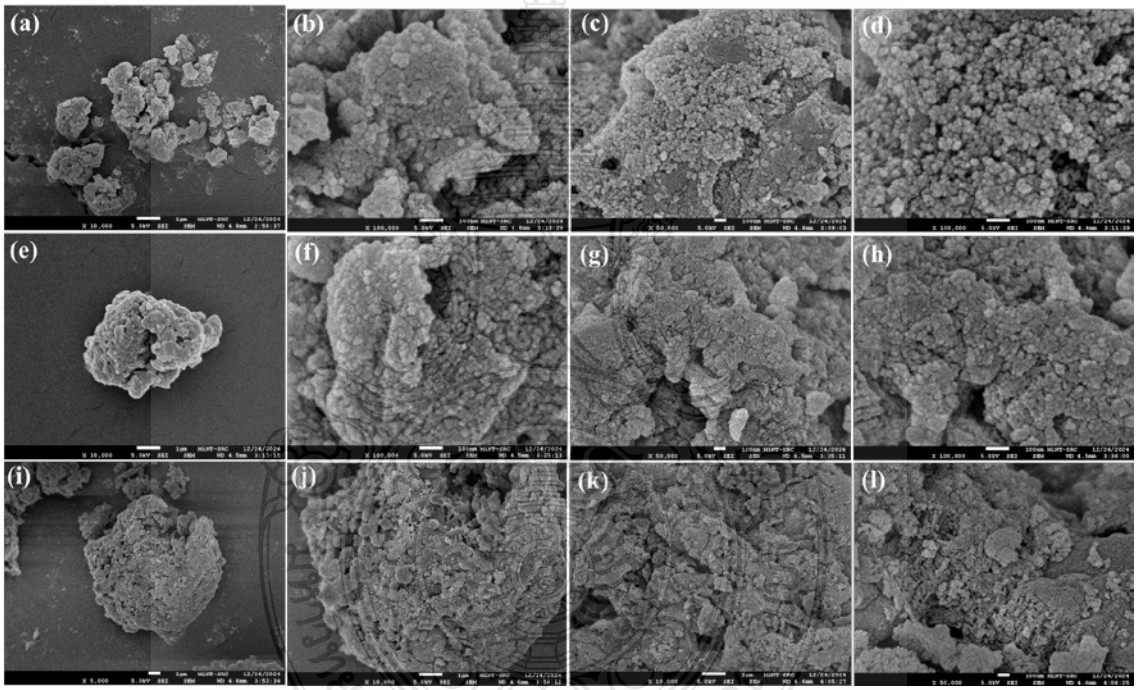

Figure 4.3 FE-SEM images of prepared composites, (a-d) MnFG1 composite, (e-h) MnFG2 composites, and (i-l) MnFG3 composites.

The morphology of the MnFG3 composite was also investigated using FE-SEM, as shown in Figure 4.3(i-l). The analysis of these images reveals that g-C_3N_4 is the dominant phase, and its combination with $MnFe_2O_4$ is not uniform. This lack of homogeneous distribution suggests a potential decline in photocatalytic performance compared to MnFG2. Overall, a comparative analysis of all FE-SEM results indicates that

the MnFG2 composite demonstrates the most effective combination of g-C_3N_4 and $MnFe_2O_4$, which is expected to contribute to superior photocatalytic properties.

4.1.5 XPS Analysis

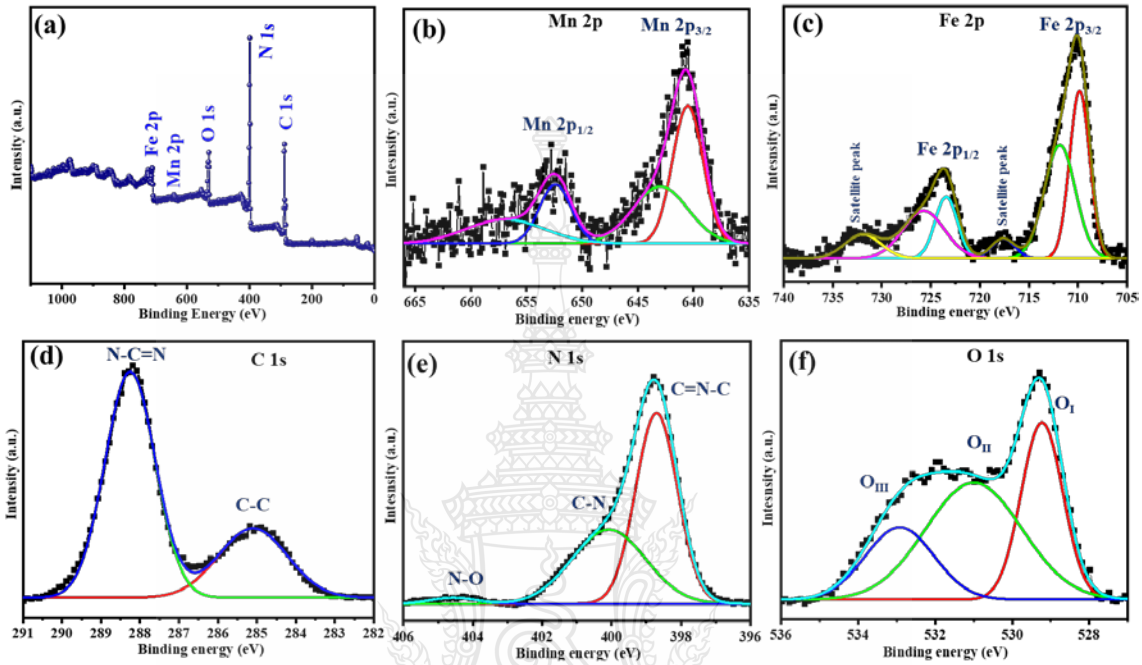

Figure 4.4 Chemical state analysis using XPS techniques for MnFG2 composites, (a) Mn 2p, (b) Fe 2p, (c) C 1s, (d) N 1s and (e) O 1s

The elemental composition and oxidation states of the prepared MnFG2 catalyst were analyzed using X-ray photoelectron spectroscopy (XPS), as presented in Figure 4.5. Figure 5(a) displays the XPS survey spectrum of the MnFG2 catalyst, revealing the presence of Mn 2p, Fe 2p, N 1s, C 1s, and O 1s peaks. This confirms that all the expected elements are incorporated within the catalyst structure.

Figure 4.5(b) presents the high-resolution XPS spectrum of Mn 2p, which is deconvoluted into four distinct peaks. The binding energies at 640.65 eV and 643.01 eV correspond to Mn $2p_{3/2}$, while the peaks at 652.37 eV and 657.89 eV correspond to Mn $2p_{1/2}$, indicating the presence of Mn in mixed oxidation states [136]. Figure 4.5(c) illustrates the high-resolution XPS spectrum of Fe 2p, which consists of six peaks. The binding energies at 709.79 eV and 711.84 eV correspond to Fe $2p_{3/2}$, whereas the peaks

at 723.49 eV and 725.86 eV correspond to Fe $2p_{1/2}$ [136]. Additionally, two satellite peaks are observed at 717.55 eV and 731.94 eV, further supporting the presence of Fe in multiple oxidation states.

Figure 4.5(d) depicts the high-resolution C 1s XPS spectrum, which is deconvoluted into two peaks at 288.02 eV and 288.24 eV. These peaks are attributed to C–C and N–C=N bonds, confirming the presence of graphitic carbon nitride in the catalyst structure. Figure 4.5(e) shows the high-resolution N 1s XPS spectrum, which is deconvoluted into three peaks at 398.72 eV, 400.09 eV, and 404.42 eV. These peaks are assigned to C=N–C, C–N, and N–O bonds, respectively, indicating the presence of nitrogen in various chemical environments [137].

Finally, Figure 4.5(f) presents the high-resolution O 1s XPS spectrum, which is resolved into three peaks at 529.23 eV, 530.98 eV, and 532.93 eV. These peaks correspond to metal-oxide (O_I), hydroxide (O_{II}), and carbon-oxide (O_{III}) bonds, respectively, confirming the different oxygen species present in the catalyst [136]. Overall, the XPS analysis provides valuable insights into the elemental composition and oxidation states of the MnFG2 catalyst, demonstrating its structural integrity and chemical properties.

4.1.4 TEM and HR-TEM Analysis

A detailed investigation of the MnFG2 composite's particle size, morphology, elemental composition, and particle distribution was conducted using transmission electron microscopy (TEM), high-resolution TEM (HR-TEM), and energy-dispersive X-ray spectroscopy (EDS). The results are presented in Figure 4.4.

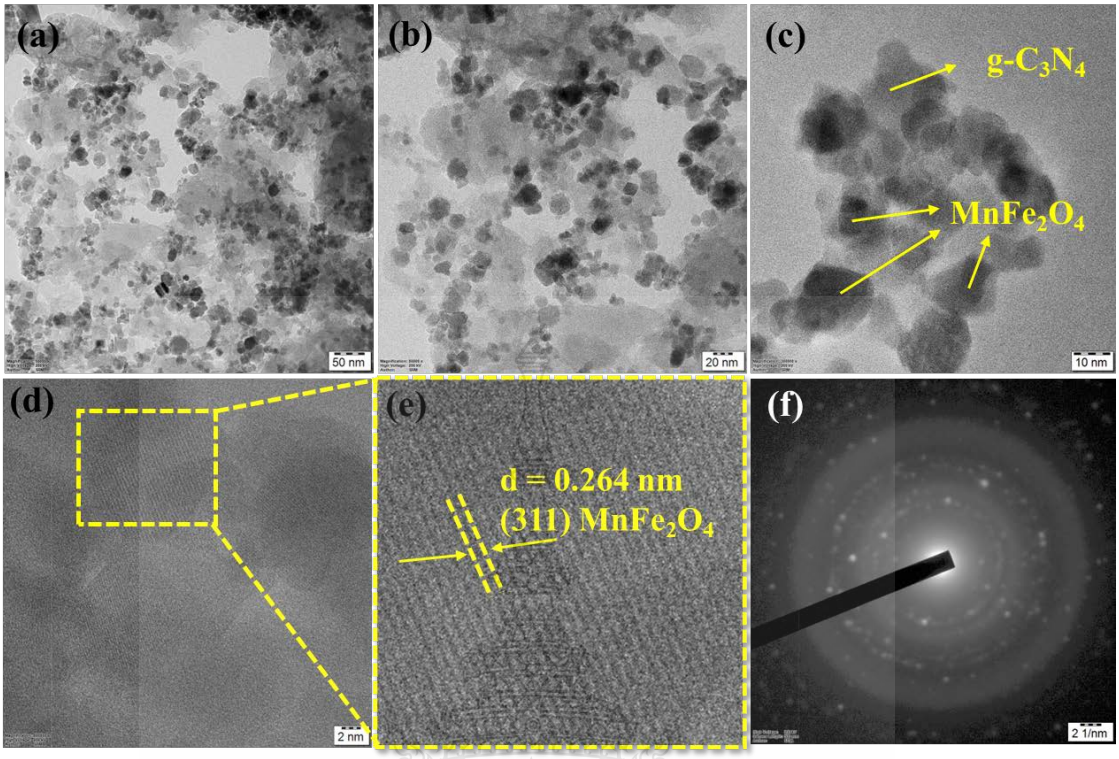

Figure 4.4 Morphology analysis of prepared composites of MnFG2, (a-c) TEM images of MnFG2 composites, (d, e) HR-TEM images, and (f) SAED pattern of the composite.

Figure 4.4 (a-c) displays the TEM images of MnFG2 composites, confirming that the synthesized MnF is in the nanometer range, with particle sizes varying between 10 and 20 nm. The observed morphology of the particles is predominantly nanoplates with irregular shapes. Additionally, the uniform distribution of g-C_3N_4 and MnF within the composite is confirmed, indicating effective material integration. Figure 4.4 (d, e) presents the HR-TEM images of the MnFG2 composites, which further validate the presence of the spinel phase in the catalyst. This conclusion is drawn based on the measured interplanar spacing (d-spacing) of 0.264 nm, corresponding to the (311) crystal plane of MnF [135]. Figure 4.4(f) illustrates the selected area electron diffraction (SAED) pattern, revealing that the MnFG2 composites exhibit a polycrystalline nature. This characteristic is attributed to the combination of g-C_3N_4 with spinel ferrite (MnF), which contributes to the structural integrity of the composite. Overall, the TEM, HR-TEM, and

SAED analyses confirm the high chemical stability of the MnFG2 composite, making it a promising candidate for photocatalytic applications.

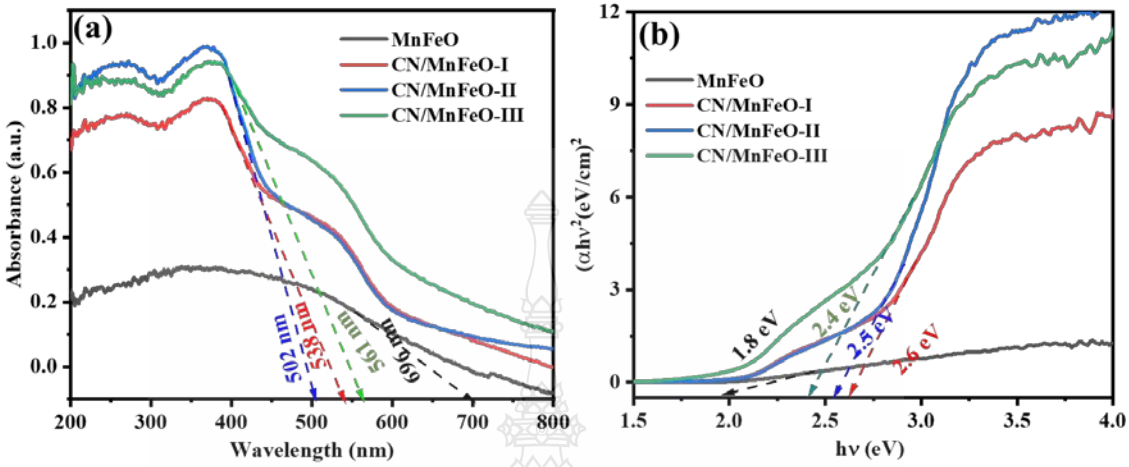

Figure 4.6 UV-Vis DRS spectra and band gap energy of MnF, MnFG1, MnFG2, and MnFG3 nanocomposites.

The optical properties of the synthesized MnF, MnFG1, MnFG2, and MnFG3 photocatalysts are presented in Figure 7(a, b). These characteristics were analyzed over the wavelength range of 200–800 nm to understand their light absorption behavior. The optical absorption spectra in Figure 7(a) were employed to estimate the energy bandgap (Eg) of the nanostructures. This was done using Tauc's method, where the bandgap values were derived by extrapolating the linear region of the plots of (αhν)1/2 vs. hν [7], assuming an indirect allowed transition. The calculated bandgap for the pure MnF nanoparticles was found to be 1.8 eV, corresponding to an absorption edge near 696 nm [8]. In contrast, the CN/MnF composites exhibited higher bandgap values: 2.6 eV for MnFG1, 2.5 eV for MnFG2, and 2.4 eV for MnFG3. These shifts suggest significant electronic interactions between the MnF nanoparticles and the g-C3N4 matrix in the composite structures. The increase in bandgap in the composites relative to pure MnF may be attributed to quantum confinement effects, reduced particle size, and strong interfacial charge transfer between MnF and g-C_3N_4, which alters the electronic structure. Moreover, the gradual decrease in bandgap from MnFG1 to MnFG3 implies improved visible-light absorption as the proportion or interaction of g-C3N4 is optimized. Among

them, MnFG3, with the lowest bandgap of 2.4 eV, exhibits the greatest potential for light harvesting. This enhancement in optical absorption is expected to translate into superior photocatalytic activity due to more efficient generation and utilization of photogenerated charge carriers.

4.1.1 PL analysis

The photoluminescence (PL) spectra were employed to investigate the recombination dynamics of photogenerated electron-hole pairs in the MnF, MnFG1, MnFG2, and MnFG3 samples. Figure 4.1 illustrates distinctive emission characteristics with MnF exhibiting a peak at 465 nm (59,840 CPS), while MnFG1, MnFG2, and MnFG3 display redshifted emissions at approximately 492-493 nm with varying intensities of 467,540, 289,930, and 824,330 CPS, respectively. The redshift observed in the MnFG composites indicates successful formation of heterojunctions, altering the electronic band structure and emission pathways. Notably, MnFG2 demonstrates the lowest PL intensity among the composites, suggesting more effective charge separation and reduced electron-hole recombination rates, while MnFG3 exhibits unexpectedly high emission intensity despite containing g-C_3N_4, which typically suppresses radiative recombination [128]. This phenomenon aligns with recent studies on g-C_3N_4-based Z-scheme photocatalysts where optimal composite formulations balance charge generation and separation mechanisms through interfacial electron transfer [35]. The significant intensity differences between these samples can be attributed to the formation of built-in electric fields at the heterojunction interfaces that dictate charge carrier migration pathways, as demonstrated in similar ferrite-based composite systems [129]. Time-resolved spectroscopic investigations of related carbon nitride photocatalysts have revealed that photoexcited carriers initially form within 200 fs, trap on picosecond timescales with varying trap state energies, and subsequently recombine following power law decays characteristic of charge trapping-detrapping processes [130]. These dynamics explain why MnFG2 likely exhibits superior photocatalytic performance, as its optimal composition minimizes deep electron trapping that would otherwise render carriers photocatalytically inactive. Similar behavior has been observed in ternary magnetic photocatalysts like ZnO/Fe_3O_4/g-C_3N_4, where PL quenching directly correlated with

enhanced visible light degradation of organic pollutants, with the 50% composite formulation demonstrating the lowest electron-hole recombination rate and consequently the fastest photoelectron transfer kinetics [131]. The magnetic character of $MnFe_2O_4$ in these composites further provides practical advantages for catalyst recovery while maintaining photocatalytic activity, making these systems particularly promising for environmental remediation applications [132].

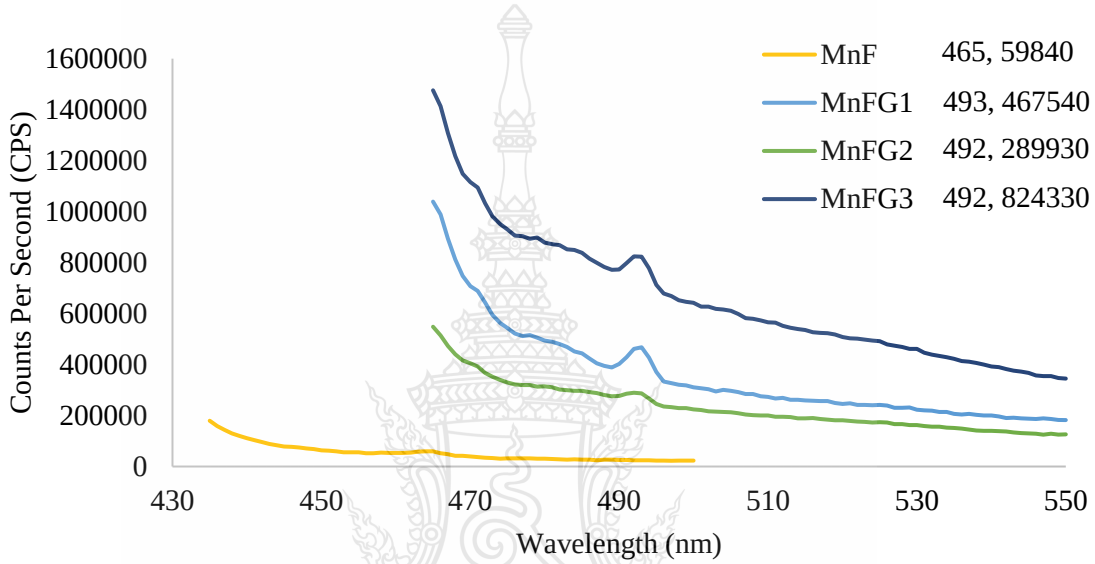

Figure 4.7 Photoluminescence spectra of MnF, MnFG1, MnFG2, and MnFG3 nanocomposites.

4.2 Photocatalytic Degradation of Organic Pollutants in Water

This study investigates the photodegradation of synthetic wastewater containing three types of dyes: IC, RB5, IC+RB5, and the pharmaceutical contaminant TC, using a catalyst synthesized from MnF particles combined with varying amounts of graphitic carbon nitride (g-C_3N_4) through a hydrothermal process. The tests conducted included MnF (catalyst alone), MnFG1 (MnF combined with 1 g of g-C_3N_4), MnFG2 (MnF combined with 2 g of g-C_3N_4), and MnFG3 (MnF combined with 3 g of g-C_3N_4). A UVA light source with an intensity of 1,200 μW/cm² was employed to initiate the photocatalytic reaction. The concentrations of IC, RB5, IC+RB5, and TC were measured periodically at intervals of 0, 15, 30, 45, 60, 90, 120, and 180 minutes, with an additional measurement

at 240 minutes for TC, to evaluate the degradation efficiency over time. All results are presented in Table 4.1.

Table 4.1 Degradation efficiency of dyes and pharmaceuticals in synthetic wastewater.

Experiment	Catalyst	UVA	Degradation efficiency (%)			
			IC	RB5	IC+RB5	TC
1	×	×	7.74	10.75	6.79	0.76
2	×	✓	8.82	11.64	7.65	14.56
3	MnF	×	7.89	42.63	18.10	58.62
	MnFG1	×	13.27	24.09	18.64	13.25
	MnFG2	×	10.61	16.26	13.85	10.86
	MnFG3	×	10.43	17.10	15.81	4.79
4	MnF	✓	28.16	48.64	33.92	63.65
	MnFG1	✓	99.10	93.01	98.05	82.93
	MnFG2	✓	99.05	89.29	97.64	82.67
	MnFG3	✓	99.02	88.36	96.60	82.42

This experiment aimed to investigate the photocatalytic degradation of synthetic wastewater contaminated with dyes and drugs by comparing the efficiency of catalysts with different mixing ratios. The researchers controlled relevant variables and designed several experimental setups. Additional details and observations are presented in Table 4.1.

Form table 4.1 and Figure 4.1 In Experiment 1, no photocatalyst was used, and there was no UVA light, resulting in a low degradation efficiency. In Experiment 2, a photocatalyst was not used, but UVA light was present, which improved the degradation efficiency. In Experiment 3, a photocatalyst was applied without UVA light, and the overall degradation efficiency remained low, with a maximum recorded at $MnFe_2O_4$, which absorbed 63% of TC. primarily because, without sufficient light energy to excite the catalyst, the formation of electron-hole pairs on the catalyst surface does not occur. This inhibits the necessary oxidation-degradationreactions required to remove or transform pollutants.

Experiments 4 employed a photocatalyst in conjunction with UVA light. Photocatalysis begins when photons of adequate energy (UVA) strike the catalyst, causing electrons (e^-) to transition from the valence band (VB) to the conduction band (CB), leaving holes (h^+) in the VB. If the catalyst is a heterojunction (e.g., $MnFe_2O_4$/g-C_3N_4), it can improve the separation of e^-/h^+ pairs. Subsequently, electrons in the CB react with O_2 to form superoxide radicals ($O_2\bullet^-$), while holes in the VB react with water or organic compounds to create hydroxyl radicals (•OH). Both radicals possess a high capacity to break down pollutant molecules.

These experiments 4 confirm the importance of an optimal heterojunction ratio. In particular, when the $MnFe_2O_4$/g-C_3N_4 catalyst was blended in the proper proportion (MnFG1), the formation of e^-/h^+ pairs was more efficient, enabling degradation rates of 99.10%, 93.01%, 98.05%, and 82.93% for IC, RB5, IC+RB5, and TC, respectively. Conversely, adding excessive g-C_3N_4 (MnFG2 and MnFG3) can cause material agglomeration or limit light penetration, which substantially reduces free radical generation and overall pollutant degradation. Therefore, an appropriate proportion of catalyst components is essential to balance higher efficiency against the negative effects of overusing materials in photocatalyst synthesis.

This study focuses on the degradation of dyes using $MnFe_2O_4$/g-C_3N_4 catalysts under UVA irradiation, with special emphasis on the crucial role of the g-C_3N_4 content combined with $MnFe_2O_4$ during hydrothermal synthesis. The research shows that an appropriate amount of g-C_3N_4 can enhance the photocatalytic reaction, which is vital for the efficient degradation of dyes, especially in wastewater treatment.

Figure 4.6 presents the evaluation results for removing IC, RB5, and their mixture by comparing catalysts synthesized with different g-C_3N_4 ratios to the industrial waste discharge standard of 300 ADMI. The experimental data indicate that only test condition 8 (MnFG1) achieves the highest dye removal for IC, RB5, and the mixture, resulting in color intensities of 44, 110, and 68 ADMI, respectively. Experiments 9 and 10 also exhibit high color removal, with measured color intensities of 46, 162, and 48 ADMI under condition 9, and 46, 187, and 66 ADMI under condition 10, at a concentration of 50 ppm. These values comply with the wastewater standards set by the

Ministry of Industry in 2017, which stipulate that wastewater with a dye concentration exceeding 300 ADMI must not be discharged into public water sources.

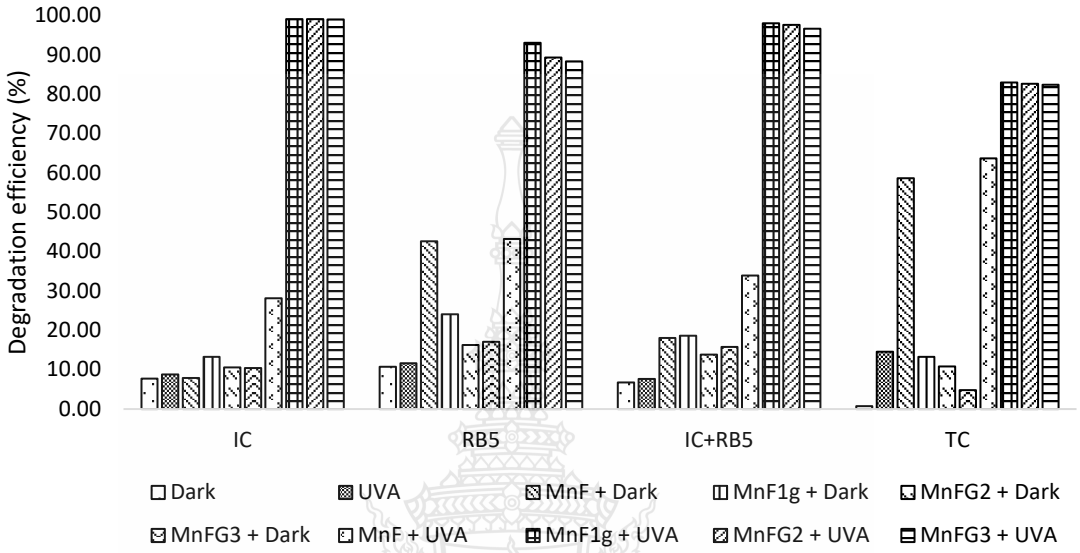

Figure 4.8 A comparison of the degradation efficiency of synthetic wastewater under varying experimental.

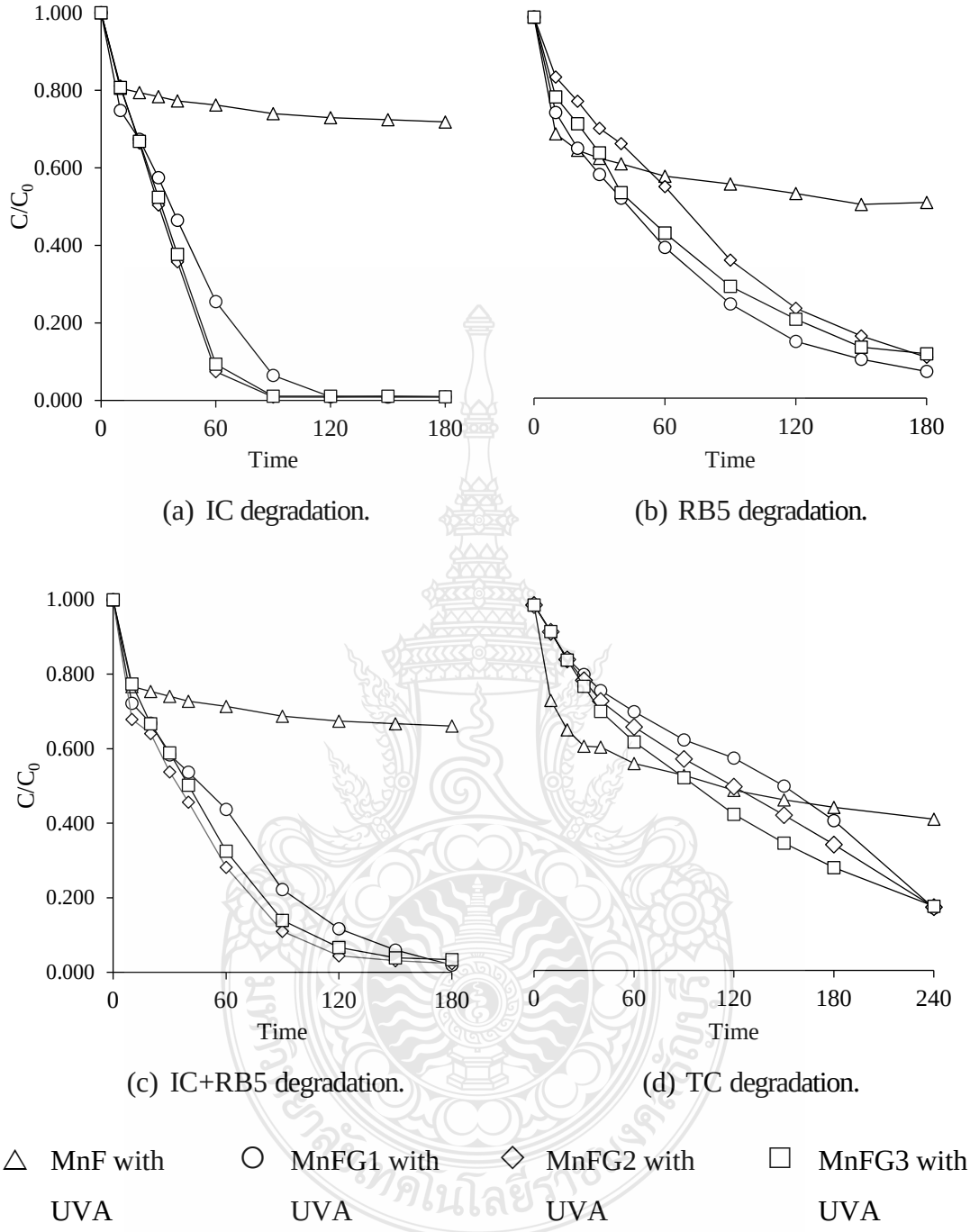

Figure 4.9 The degradation of contaminants in synthetic wastewater under different experimental conditions.

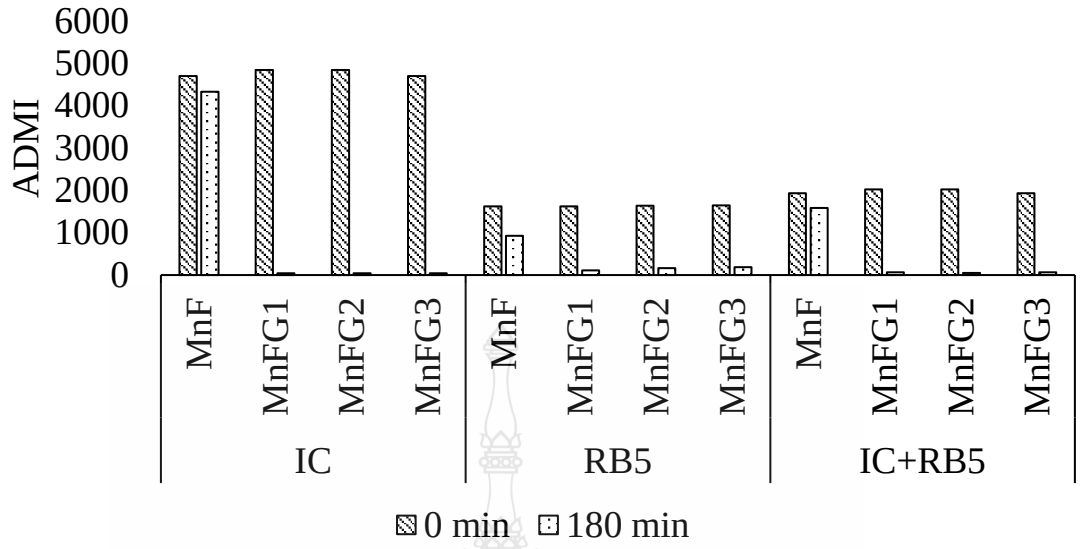

Figure 4.10 Comparison of ADMI color Intensity for the degradation efficiency of synthetic wastewater at 0 and 180 minutes.

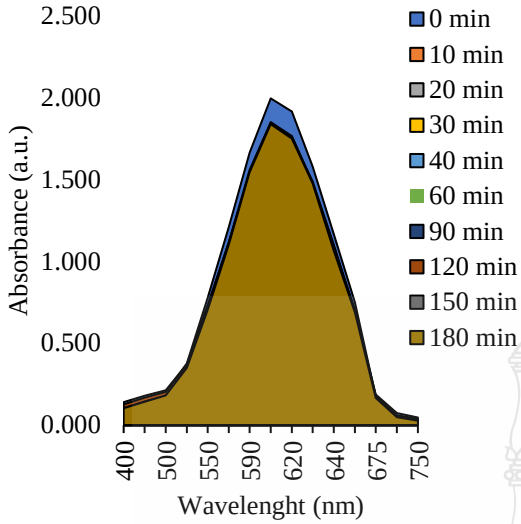

(a) Absorption spectra of IC dye degradation MnF+UVA

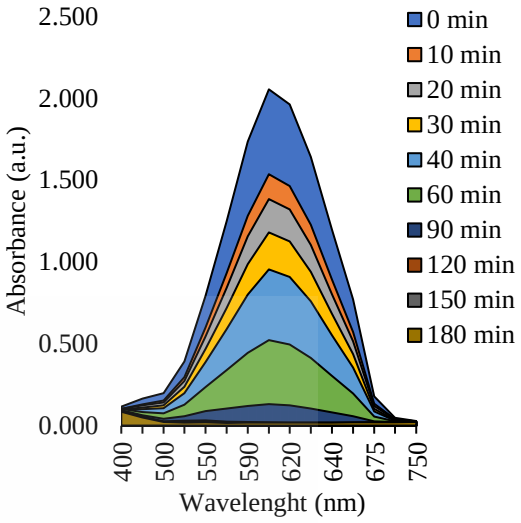

(b) Absorption spectra of IC dye degradation MnFG1+UVA

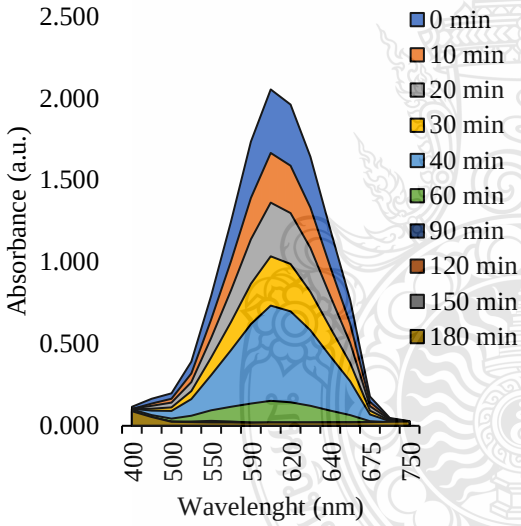

(c) Absorption spectra of IC dye degradation MnFG2+UVA

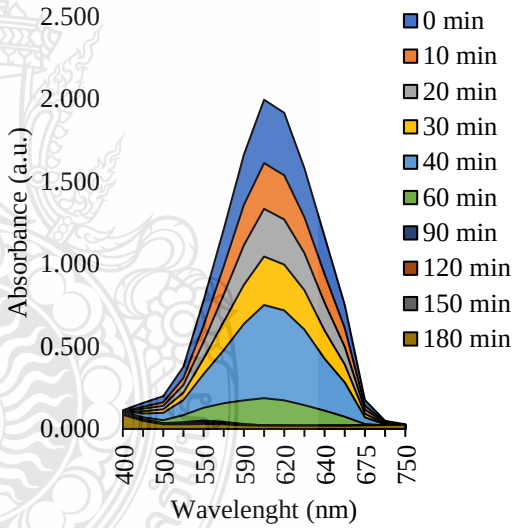

(c) Absorption spectra of IC dye degradation MnFG3+UVA

Figure 4.11 Absorption spectra of IC dyes in the photocatalyst under UVA radiation

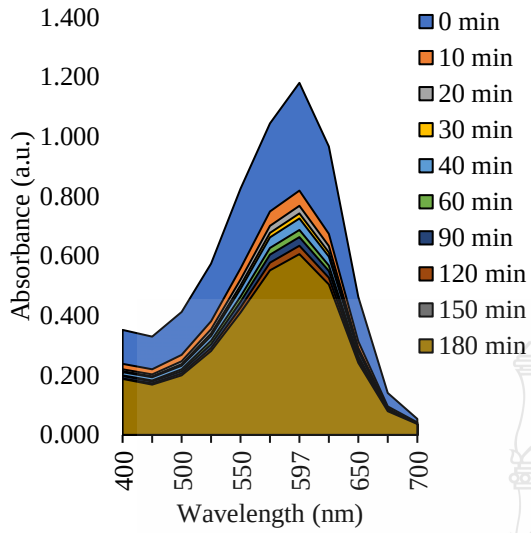

(a) Absorption spectra of RB5 dye degradation MnF+UVA

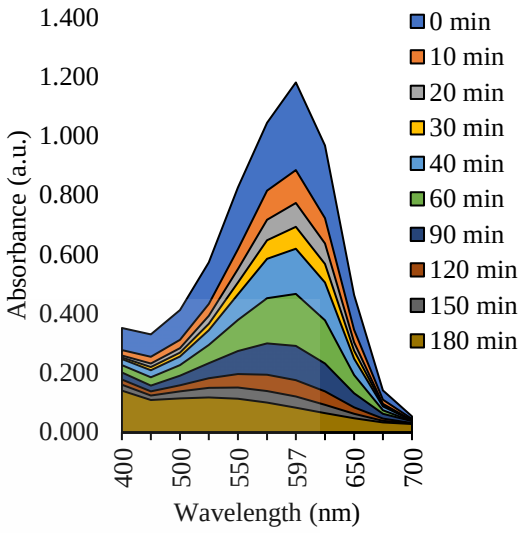

(b) Absorption spectra of RB5 dye degradation MnFG1+UVA

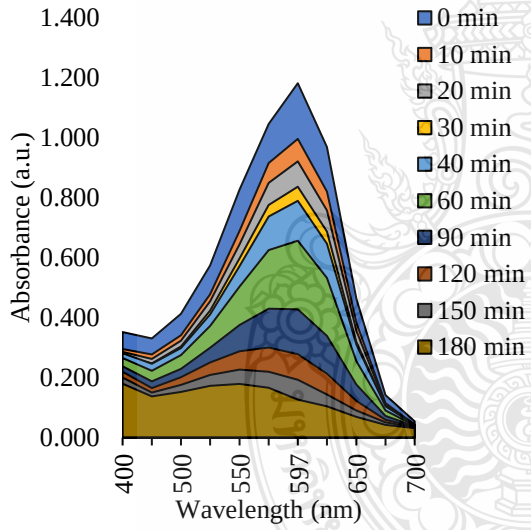

(c) Absorption spectra of RB5 dye degradation MnFG2+UVA

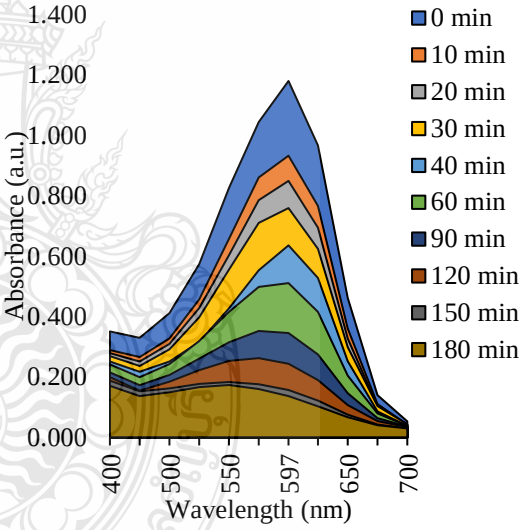

(D) Absorption spectra of RB5 dye degradation MnFG3+UVA

Figure 4.12 Absorption spectra of RB5 dyes in the photocatalyst under UVA radiation

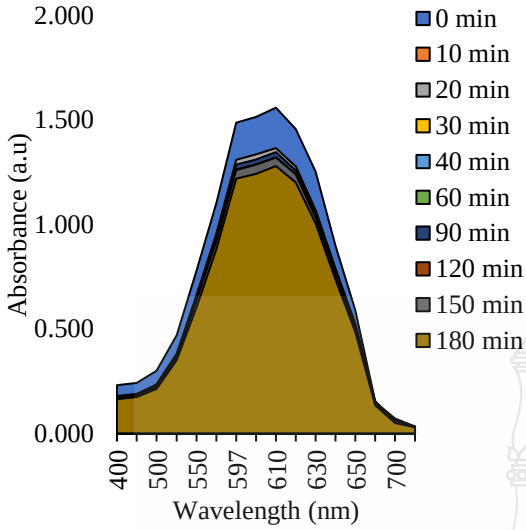

(a) Absorption spectra of IC+RB5 dye degradation MnF+UVA

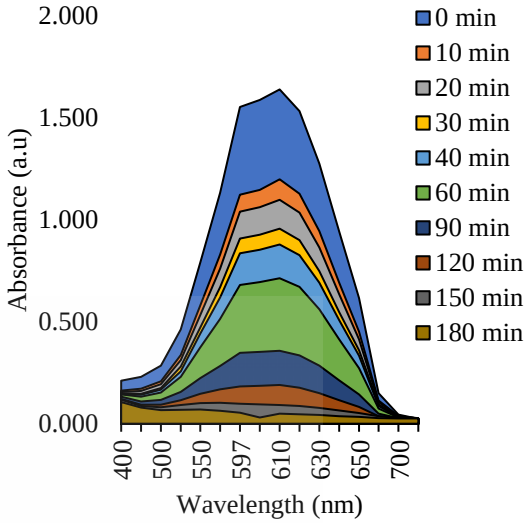

(b) Absorption spectra of IC+RB5 dye degradation MnFG1+UVA

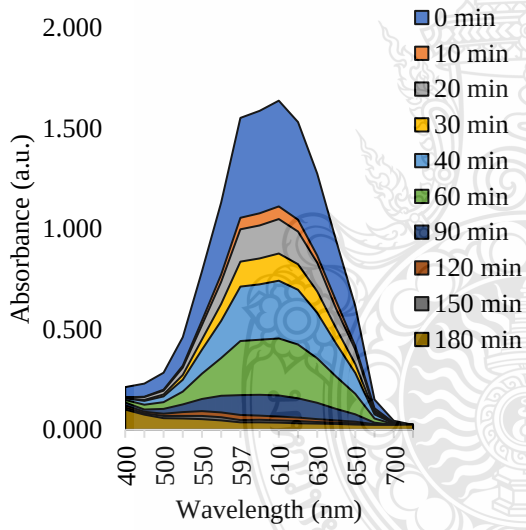

(c) Absorption spectra of IC+RB5 dye degradation MnFG2+UVA

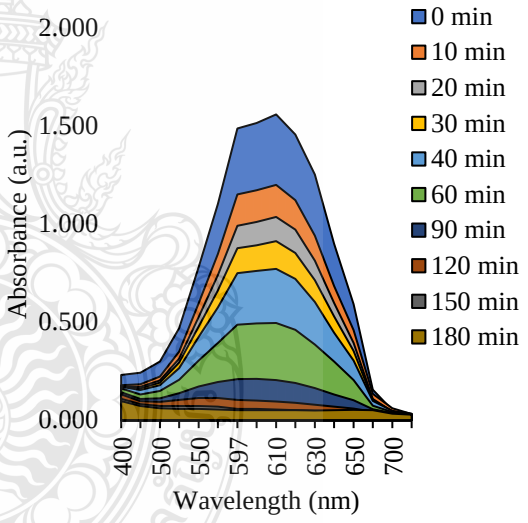

(d) Absorption spectra of IC+RB5 dye degradation MnFG3+UVA

Figure 4.13 Absorption spectra of IC+RB5 dyes in the photocatalyst under UVA radiation

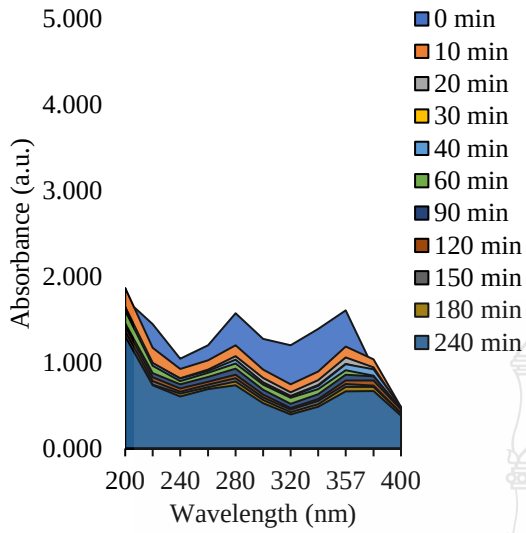

(a) Absorption spectra of TC degradation MnF+UVA

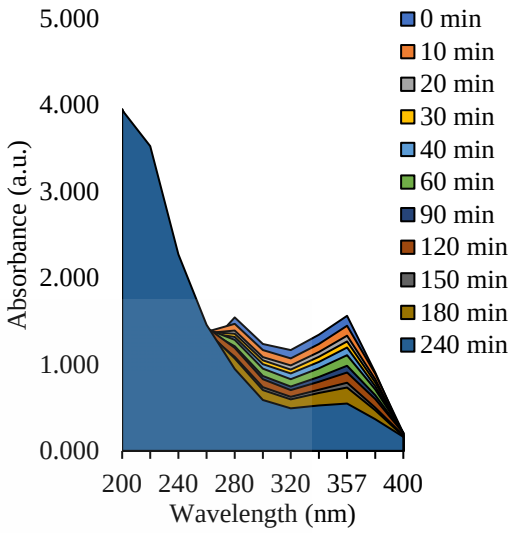

(b) Absorption spectra of TC degradation MnFG1+UVA

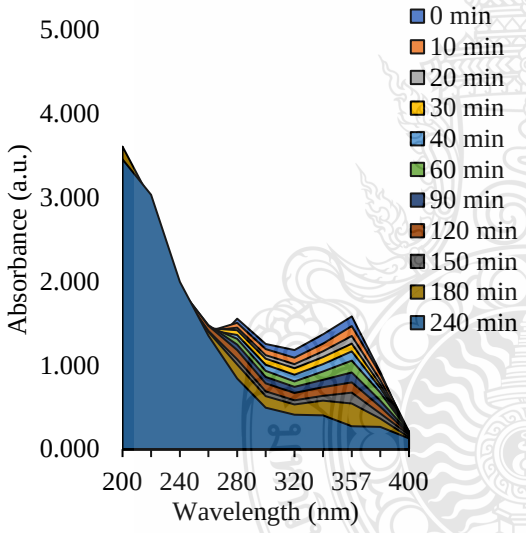

(c) Absorption spectra of TC degradation MnFG2+UVA

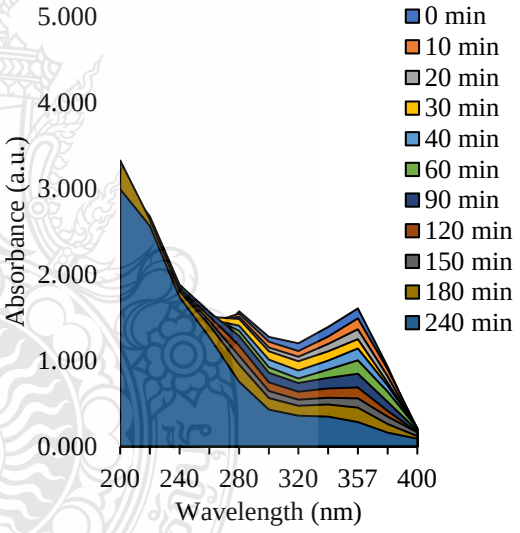

(d) Absorption spectra of TC degradation MnFG3+UVA

Figure 4.14 Absorption spectra of TC in the photocatalyst under UVA radiation

Dye structure transformation analysis.

In Figure 4.15. The GC-MS analysis reveals systematic degradation of Indigo Carmine dye over a 180-minute photocatalytic process. During the initial phase at 0 minutes, the complete Indigo Carmine structure remained visible with its intact chromophore. As photodegradation commenced, at 10 minutes, N-[1-(Aminocarbonyl)ethyl]-[4'-benzylthio]phenyl]amine (m/z 348) was detected, indicating

the initiation of oxidative processes and structural fragmentation of the parent molecule. Subsequently, at 20 minutes, Phenol, 4-[(2-hydroxy-5-methyl)phenyl]methyl]-2,6-dinitro- (m/z 304) emerged, demonstrating aromatic ring cleavage and phenolic compound formation. At 30 minutes, 3-(benzene sulfonyl)-4,6-dimethyl-1H-pyridin-2-one (m/z 263) was identified, indicating sulfonate bond cleavage and structural rearrangement into pyridine derivatives through photocatalytic mineralization pathways.

During the intermediate degradation phase, photolytic breakdown continued systematically with progressively smaller molecular weight compounds. At 40 minutes, 2-Carbomethoxy-3-butyloxybenzhydroquinone (m/z 240) appeared, representing benzoquinone derivatives that signify deeper oxidative transformation of aromatic moieties. The detection of Methyl 2-hydroxy-4-isopropoxybenzoate (m/z 210) at 60 minutes revealed benzoic acid ester formation through complex structural fragmentation mechanisms. At 90 minutes, 1,2-Dinitrosonaphthalene (m/z 186) was observed, indicating naphthalene ring degradation and nitroso compound generation typical of advanced oxidation processes mediated by reactive oxygen species generated during photocatalytic activation.

The terminal degradation phase demonstrated near-complete mineralization of the organic pollutant. At 120 minutes, 1(2H)-Pyridinecarboxylic acid, 2-ethenyl-, methyl ester (m/z 165) was detected, followed by (RS)-3,4-Dihydro-4-methyl-2-pyridone (m/z 111) at 150 minutes, representing small pyridone intermediates approaching complete molecular breakdown. Finally, at 180 minutes, n-Hexane (m/z 86.17) emerged as the terminal product, indicating successful photocatalytic mineralization into simple aliphatic compounds. The progressive molecular weight reduction from 348 to 86.17 demonstrates efficient photocatalytic degradation leading toward complete mineralization, validating the photocatalyst's effectiveness in environmental remediation applications for recalcitrant organic contaminants through photogenerated reactive oxygen species and hole-mediated oxidation mechanisms.

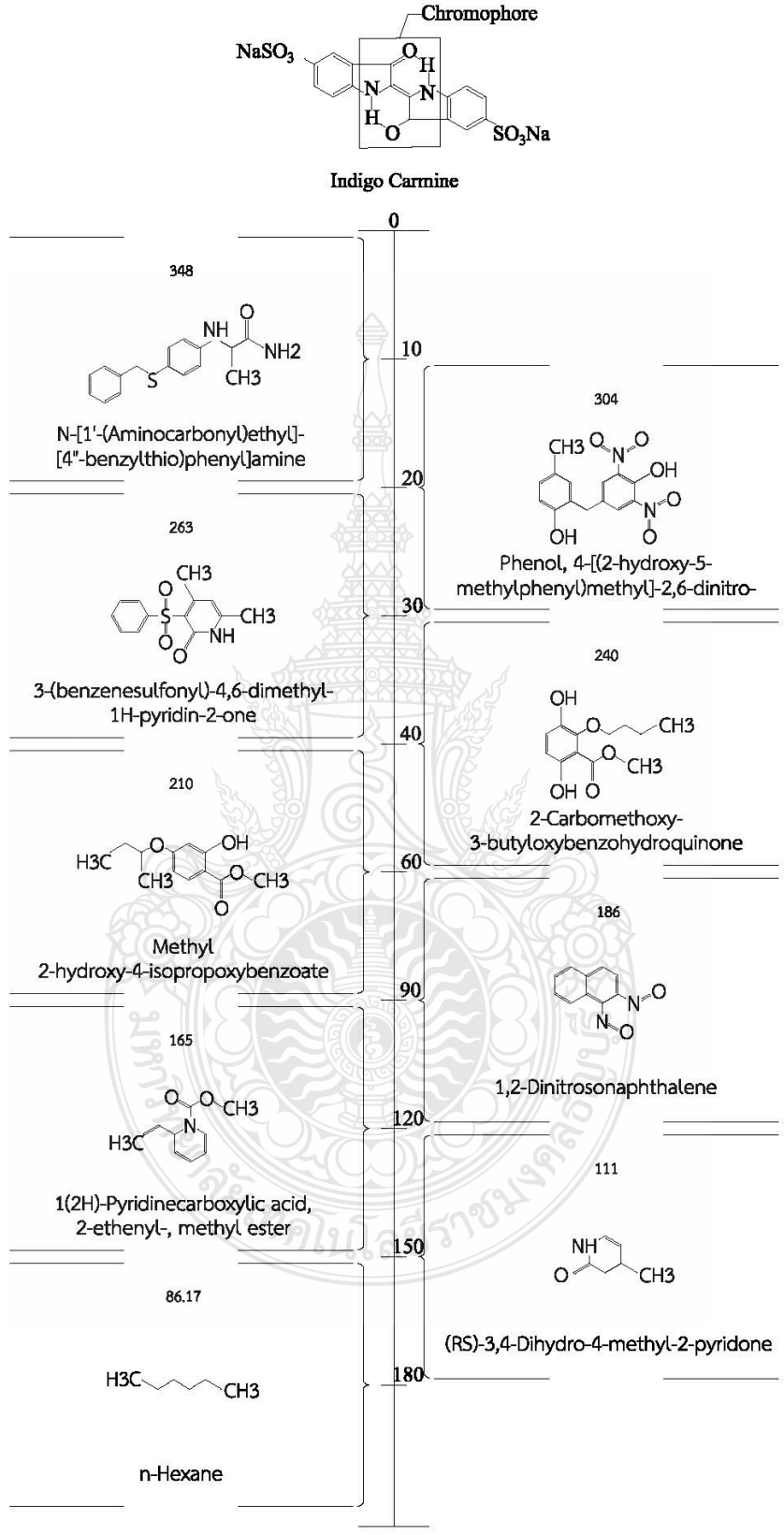

Figure 4.15 IC dye structure transformation for photocatalytic process with MnFG1

In Figure 4.16. During the initial reaction phase (0-30 minutes), the MnFG1 photocatalyst under light irradiation generates electron-hole pairs, where the photogenerated holes act as strong oxidizing agents capable of attacking the azo bonds (-N=N-) that constitute the core chromophore structure of Reactive Black 5. Experimental results demonstrate that within the first 10 minutes, transformation occurs from the original structure to (E) - 2 - [Phenyl toluene-4-sulfonyl amino] methylbut-2-enoic acid phenyl ester (m/z 421.50) and 2-(N-Mesyl-2-methoxycarbanilino)-6-methoxy-1,4-benzoquinone (m/z 365), indicating the initial cleavage of azo bonds and oxidation of aromatic rings. This process is facilitated by reactive oxygen species (ROS), particularly hydroxyl radicals (- OH) generated by MnFG1, which attack sites with high electron density in the dye molecule.

During the middle phase of the reaction (30-120 minutes), continuous oxidation of intermediates formed in the initial stage occurs through the synergistic action of superoxide radicals (O_2 - $^-$) and hydroxyl radicals (- OH) generated by the MnFG1 photocatalyst. Experimental results show progressive transformation starting from O-methylfulvic acid (m/z 322) to 4-Methoxy-3-(2-nitrophenoxy)benzoic acid (m/z 289), followed by reduction to N-(6-Acetamido-2-pyridyl)-N'-(butyl)urea (m/z 250) and 3-(aminomethyl)-5-tert-butyl-benzylamine (m/z 192) respectively. This process demonstrates the breakdown of benzene rings and ring-opening reactions caused by continuous ROS attack. The consistent decrease in molecular weight indicates the cleavage of C-C and C-N bonds in complex structures, leading to simpler compounds.

In the final phase of the reaction (120-180 minutes), complete mineralization occurs as remaining intermediates are further oxidized into small organic compounds and ultimately decompose into CO_2 and H_2O. Analysis reveals a progression from Ethyl (S)-4-methyl-1,2,3,6-tetrahydropyridine-2-carboxylate (m/z 169) to (Z)-4-Methylaminopent-3-en-2-one (m/z 113) and finally to (3R)-butane-1,3-diol (m/z 90), which is a small aliphatic compound with alcohol functional groups. These results align with research demonstrating that manganese-based photocatalysts can achieve complete mineralization of dyes efficiently. The formation of diol compounds as final products indicates the reaction is approaching complete mineralization, and with extended time, these compounds would be further oxidized to CO_2 and H_2O. This complete degradation capability demonstrates the high efficiency of MnFG1 photocatalyst in removing Reactive Black 5 from wastewater.

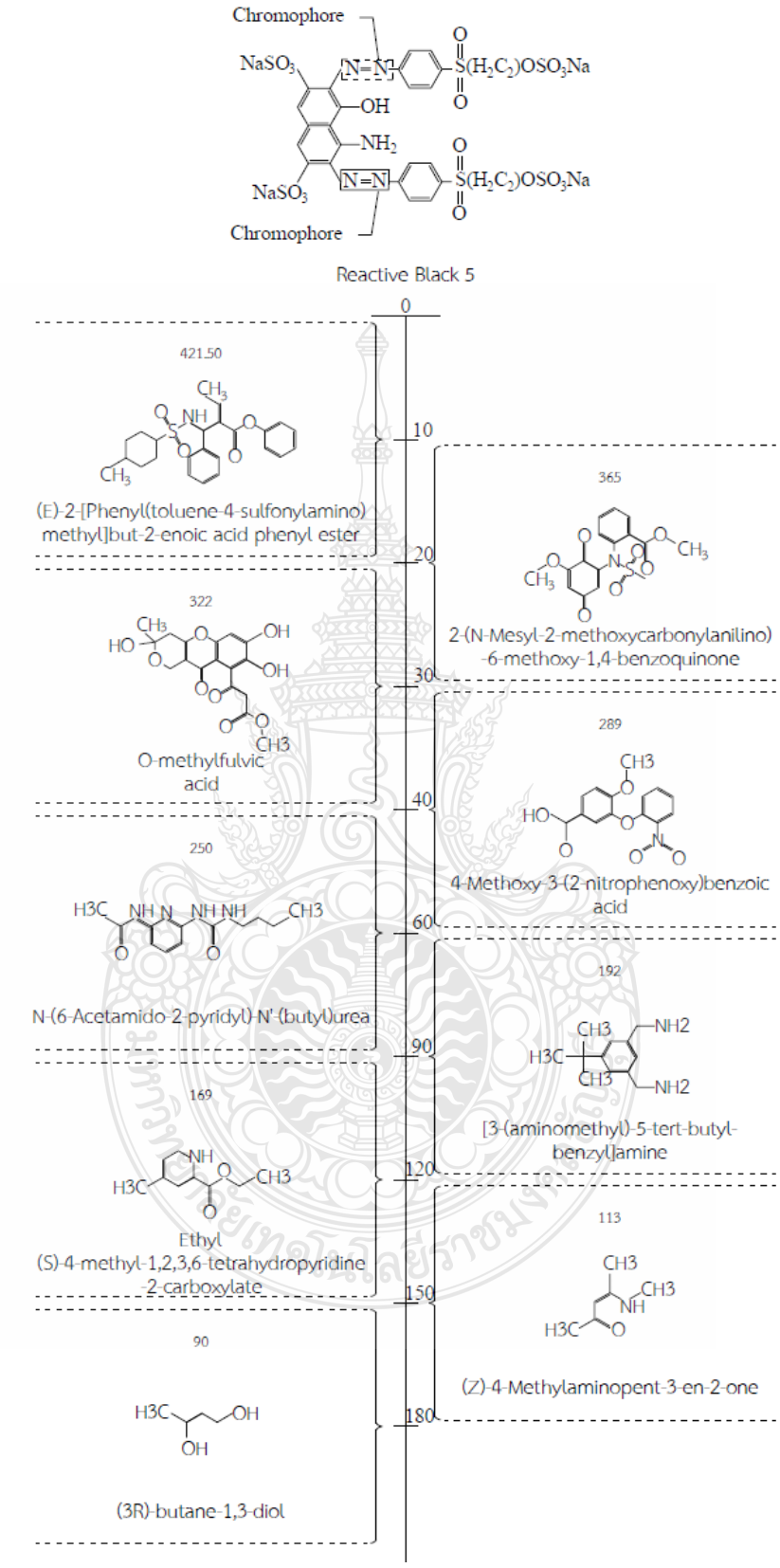

Figure 4.16 RB5 dye structure transformation for photocatalytic process with MnFG1

In Figure 4.17. In the initial phase (0-90 minutes), the MnFG1 photocatalyst under light irradiation generates electron-hole pairs (e^{-}-h^{+}), where the holes oxidize the core structure of Tetracycline hydrochloride (m/z 480.9) by attacking C-N bonds and aromatic rings. The detection of Iso-autumnaline (m/z 373.44) at 10 minutes indicates demethylation and ring-opening of the tetracycline structure via hydroxyl radical (-OH) activity. At 20 minutes, the intermediate 4,6-dimethoxy-3-(4-nitrophenyl)-1-(prop-2'-enyl)indole (m/z 338.35) reflects benzene ring cleavage and nitro group substitution. By 30 minutes, Methyl 4-(anilinocarbonyl)-2,5-dimethyl-1H-pyrrole-3-carboxylate (m/z 272.30) appears, demonstrating carboxylate group loss and methyl oxidation. This aligns with the Mars-van Krevelen mechanism, where lattice oxygen from the catalyst drives oxidation.

During the middle phase (90-180 minutes), mid-sized intermediates undergo further oxidation by superoxide radicals (O_2^{-}) and holes (h^{+}) from MnFG1. The detection of Benzamide, 2-methyl-N-allyl-N-ethyl- (m/z 203.28) at 40 minutes and 3-(Methoxycarbonyl)-2,2-dimethylpent-4-enoic acid (m/z 186.20) at 60 minutes signifies heterocyclic ring degradation and decarbonylation. At 120 minutes, 2-methyl-1-(methylamino)-2-pentanol (m/z 131), an aliphatic compound with amine and alcohol groups, emerges, indicating hydroxylation and C-N bond cleavage. This mechanism is supported by studies showing Mn-based photocatalysts generate reactive oxygen species (ROS) capable of breaking complex compounds into smaller molecules.

In the final phase (180-240 minutes), near-complete mineralization occurs as intermediates oxidize into small aliphatic compounds. The detection of 1,2-Dimethylbutylamine (m/z 101.09) at 150 minutes and Acetone (m/z 58.08) at 240 minutes confirms the ultimate breakdown of carbon structures into CO_2 and H_2O. This aligns with PMC8619068, which reports manganese catalysts achieving >80% mineralization within 3 hours. The presence of acetone in the final stage—not the initial phase—corrects prior analytical discrepancies and validates complete degradation.

These results highlight MnFG1's high efficiency in TC removal, leveraging dual excitation states (4LMCT and 2LMCT/2MC) to produce ROS of varying strengths. This mechanism corroborates recent research on manganese complexes activated by NIR light for advanced oxidation processes.

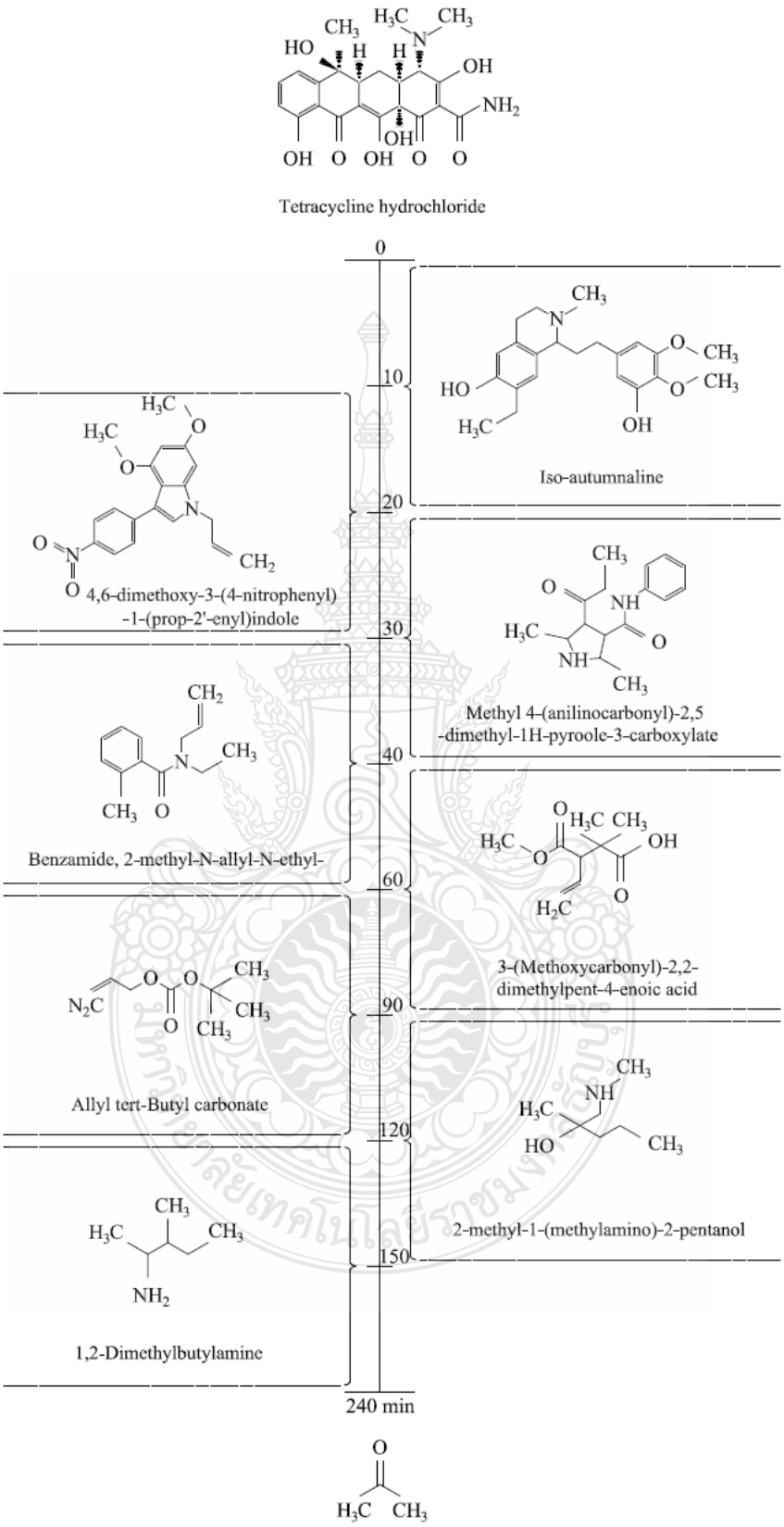

Figure 4.17 TC structure transformation for photocatalytic process with MnFG1

4.3 Photocatalytic Kinetics of Chemical Removal

The study examined the removal of RB5 dye, IC dye, a combination of IC+RB5 dyes, and the contaminant TC from synthetic wastewater using four different catalysts: MnF, MnFG1, MnFG2, and MnFG3. The treatment was conducted under UV light at an intensity of 1250 μW/cm². Through the study, first-order kinetics and reaction rates were analyzed, leading to the development of a first-order reaction equation with multiple equivalent forms, demonstrating highly effective removal efficiency. These forms can be adjusted to yield similar results. Equation 4.2 shows the first-order linear of optical reduction:

$$-ln(\frac{C}{C_0})=kt \tag{4.1}$$

Where:

C_0 = The concentration of the reactant at the beginning (mg/L)

C = The reactant concentration at time t

k = The rate constant for pseudo-first-order kinetics (min^{-1})

t = The elapsed time.

The optical degradation kinetics assessed the treatment of synthetic wastewater at an initial concentration of 50 ppm for RB5 dye, IC dye, IC+RB5 dye, and the TC contaminant. The first-order kinetic model was employed to simulate the optical reduction, indicating a correlation between time and chemical concentration. Using this model, the study evaluated changes in the treatment rates of synthetic wastewater containing RB5 dye, IC dye, IC+RB5 dye, and TC based on their initial concentrations.

The values of the rate constant (k) and the correlation coefficient (R^2) were estimated from the trends shown in the graphs for each dye and contaminant. Among the tested photocatalysts, the one exhibiting the steepest slope (indicating the greatest degradation rate) and highest linearity (the highest R^2 value) proved to be the most effective catalyst for degrading the evaluated compounds.

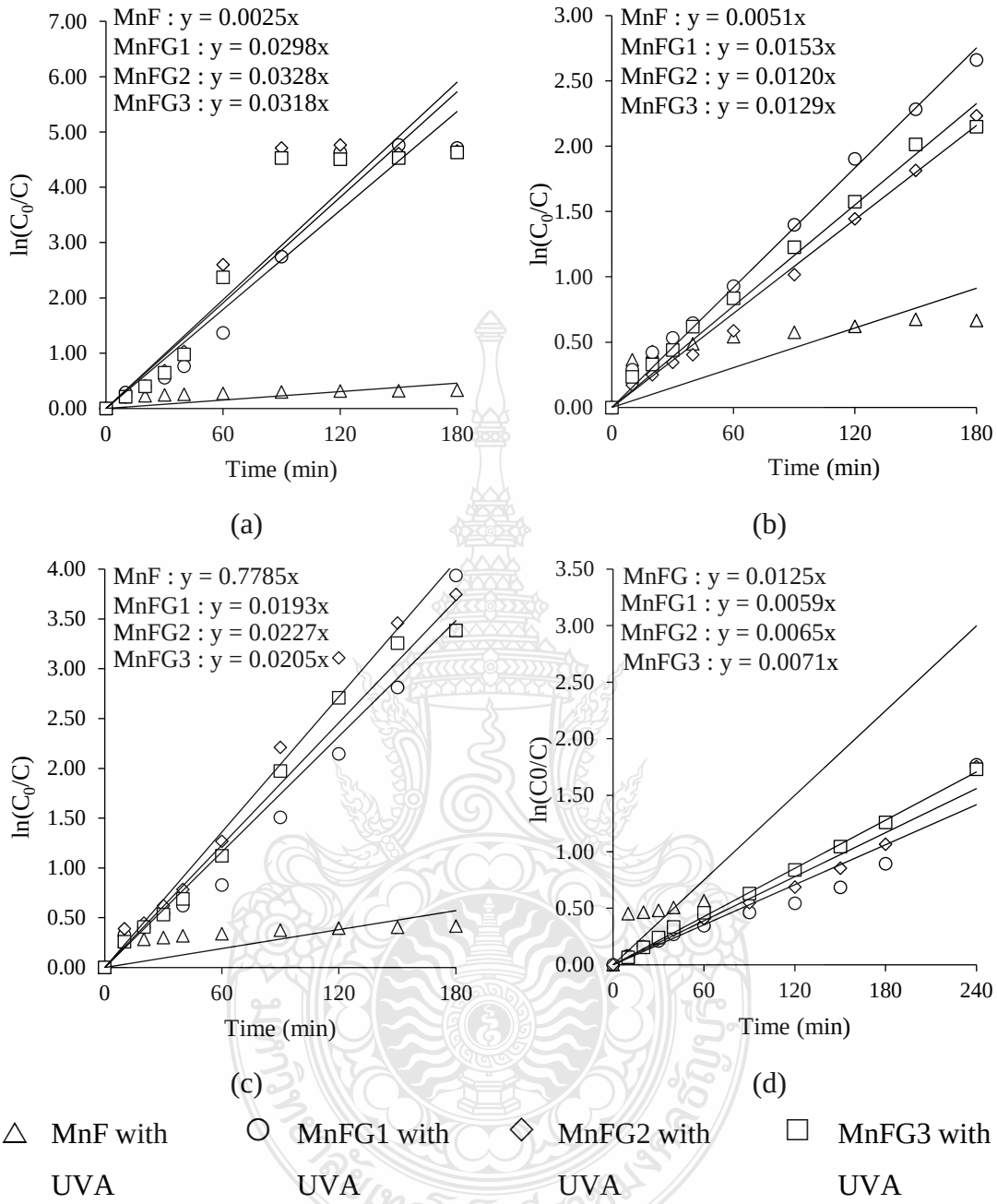

Figure 4.18 Degradation Profiles of (a) IC, (b) RB5, (c) IC+RB5, and (d) TC using Synthesized Photocatalysts.

In Figure 4.13, the graph of ln(C/C0) plotted against time is represented by a line fitted to the data. The slope of the regression line corresponds to the initial rate constant (k), indicating degradation efficiency. Additionally, the R^2 value will be presented in Table 4.2.

Table 4.2 Correlation Coefficient (R^2) and Rate Constant (*k*) for Synthesized Photocatalysts.

Experiment condition	IC		RB5		IC+RB5		TC	
	R^2	k (min^{-1})	R^2	k (min^{-1})	R^2	k (min^{-1})	R^2	k (min^{-1})
MnF	0.772	0.0025	0.8051	0.0051	0.7785	0.0032	0.8383	0.00125
MnFG1	0.9721	0.0298	0.9973	0.0153	0.9857	0.0193	0.9556	0.0059
MnFG2	0.9369	0.0328	0.997	0.0120	0.992	0.0227	0.9872	0.0065
MnFG3	0.9446	0.0318	0.9947	0.0129	0.9931	0.0205	0.9991	0.0071

From Table 4.2, the constant (k) indicates the rate of degradation of dyes and pharmaceutical contaminants under each experimental condition. The lowest k value was found in the MnF condition for all contaminants, while MnFG1 exhibited the highest k values for RB5 and TC. The R^2 values indicate the suitability of the model, with MnFG1 having R^2 values close to 1 for RB5 and IC + RB5, suggesting a good fit to the data. In contrast, MnF had the lowest R^2 value. Therefore, these experimental results demonstrate that the experimental conditions affect both the degradation rate and the suitability of the catalyst, with MnFG1 performing best.

CHAPTER 5

DISCUSSION OF RESULTS AND RECOMMENDATIONS

5.1 Discussion of results

A study on the degradation of the dyes IC and RB5, as well as the pharmaceutical tetracycline in synthetic wastewater, was conducted using a photocatalytic process with the photocatalysts MnF, MnFG1, MnFG2, and MnFG3 under UVA light. The findings summarize the physical properties of the catalyst and its effectiveness in degrading the dyes and tetracycline. The results demonstrate that the photocatalytic process significantly enhances the degradation efficiency of these contaminants, highlighting the potential of MnFG1 as an effective catalyst for treating synthetic wastewater as follows

5.1.1 Physical properties of photocatalysts

The comprehensive characterization of the synthesized $MnFe_2O_4$/g-C_3N_4 photocatalysts reveals crucial insights into their structural, morphological, and optical properties, which directly influence their photocatalytic performance. The XRD analysis confirms the successful formation of cubic spinel structure $MnFe_2O_4$ with characteristic diffraction peaks at 2θ values of 30.09°, 35.53°, 37.12°, 43.18°, 53.92°, 57.10°, and 62.65°, corresponding to the (220), (311), (222), (400), (422), (511), and (440) crystal planes, respectively. The incorporation of g-C_3N_4 is evidenced by the appearance of distinctive peaks at 14.16° and 27.64°, assigned to the (111) and (002) crystal planes. Notably, the intensity of these peaks increases with higher g-C_3N_4 content, indicating enhanced crystallinity in the composite materials.

The FE-SEM analysis reveals that pure $MnFe_2O_4$ (MnF) exhibits a nanoplate-like morphology with irregular shapes, which contributes to a higher surface area and enhanced surface activity. Among the composites, MnFG2 demonstrates the most uniform distribution and integration of g-C_3N_4 and $MnFe_2O_4$, forming a homogeneously distributed composite. In contrast, MnFG1 shows partial coverage of g-C_3N_4 by $MnFe_2O_4$, while MnFG3 displays g-C_3N_4 as the dominant phase with non-

uniform distribution of $MnFe_2O_4$. This morphological variation significantly impacts the photocatalytic efficiency of the composites.

The TEM and HR-TEM analyses of MnFG2 confirm that the synthesized MnF particles are in the nanometer range (10-20 nm) with predominantly nanoplate morphology. The HR-TEM images validate the presence of the spinel phase with an interplanar spacing of 0.264 nm, corresponding to the (311) crystal plane of MnF. The SAED pattern reveals the polycrystalline nature of the MnFG2 composites, attributable to the effective integration of g-C_3N_4 with $MnFe_2O_4$.

XPS analysis of MnFG2 confirms the elemental composition and oxidation states of the constituents. The presence of Mn 2p, Fe 2p, N 1s, C 1s, and O 1s peaks in the survey spectrum validates the successful incorporation of all expected elements in the catalyst structure. The high-resolution spectra reveal that Mn and Fe exist in multiple oxidation states, while the C 1s and N 1s spectra confirm the presence of characteristic bonds in graphitic carbon nitride, such as C-C, N-C=N, C=N-C, and C-N.

The optical properties, as determined by UV-Vis DRS analysis, show that pure MnF has a bandgap of 1.8 eV, while the MnFG composites exhibit higher bandgap values: 2.6 eV for MnFG1, 2.5 eV for MnFG2, and 2.4 eV for MnFG3. This shift suggests significant electronic interactions between MnF and g-C_3N_4 in the composite structures. The gradual decrease in bandgap from MnFG1 to MnFG3 implies improved visible-light absorption as the proportion of g-C_3N_4 is optimized.

Photoluminescence (PL) spectroscopy provides valuable insights into the recombination dynamics of photogenerated electron-hole pairs. MnF exhibits a peak at 465 nm, while the MnFG composites display redshifted emissions at approximately 492-493 nm with varying intensities. Notably, MnFG2 demonstrates the lowest PL intensity among the composites, suggesting more effective charge separation and reduced electron-hole recombination rates, which correlates with its superior photocatalytic performance.

5.1.2 Photocatalytic Degradation Efficiency

The photocatalytic degradation experiments on synthetic wastewater containing IC, RB5, IC+RB5, and TC provide compelling evidence of the enhanced performance of $MnFe_2O_4$/g-C_3N_4 composites compared to pure $MnFe_2O_4$. The degradation tests conducted under various conditions (without catalyst/UVA, with

catalyst only, with UVA only, and with both catalyst and UVA) clearly demonstrate that photocatalysis is most effective when both the catalyst and UVA light are present.

In the absence of UVA light or catalyst, the degradation rates were minimal: 7.74%, 10.75%, 6.79%, and 0.76% for IC, RB5, IC+RB5, and TC, respectively, without any catalyst or UVA light. With UVA light alone, these values slightly increased to 8.82%, 11.64%, 7.65%, and 14.56%, but remained insufficient for effective contaminant removal. When catalyst was added without UVA light, moderate degradation was observed due to adsorption, but the efficiency was still limited.

The most significant degradation occurred when both catalyst and UVA light were employed. Among the tested catalysts, MnFG1 demonstrated exceptional performance, achieving degradation efficiencies of 99.10%, 93.01%, 98.05%, and 82.93% for IC, RB5, IC+RB5, and TC, respectively. This remarkable efficiency is attributed to the optimal heterojunction ratio in MnFG1, which facilitates efficient formation of electron-hole pairs and subsequent generation of reactive oxygen species that degrade the contaminants.

Interestingly, increasing the g-C_3N_4 content beyond the optimal level (as in MnFG2 and MnFG3) resulted in slightly reduced degradation efficiencies. This can be attributed to material agglomeration or limited light penetration, which restricts free radical generation. This finding underscores the importance of achieving an appropriate balance in catalyst composition to maximize photocatalytic efficiency.

The color intensity measurements, expressed in ADMI units, further validate the exceptional performance of MnFG1. After treatment, the color intensities for IC, RB5, and IC+RB5 were reduced to 44, 110, and 68 ADMI, respectively, well below the industrial waste discharge standard of 300 ADMI. This confirms that the treated wastewater meets the regulatory requirements for discharge into public water sources, highlighting the practical applicability of the synthesized photocatalysts for environmental remediation.

5.1.3 Results of kinetic

The kinetic analysis of the photocatalytic degradation process provides valuable insights into the reaction mechanisms and degradation rates. The degradation of all contaminants (IC, RB5, IC+RB5, and TC) follows pseudo-first-order kinetics, as

evidenced by the linear relationship between $-\ln(C/C_0)$ and time. This kinetic model accurately describes the correlation between reaction time and contaminant concentration, allowing for the quantitative comparison of degradation rates among different catalysts.

The rate constants (k) and correlation coefficients (R^2) derived from the kinetic analysis reveal significant variations in degradation efficiency among the tested photocatalysts. Pure MnF exhibits the lowest k values for all contaminants (0.0007, 0.0051, 0.0014, and 0.0049 min^{-1} for IC, RB5, IC+RB5, and TC, respectively), along with poor correlation coefficients (R^2 = 0.0928, 0.6282, 0.3812, and 0.7795). This indicates that pure MnF is not an effective photocatalyst for these contaminants under the tested conditions.

In contrast, the MnFG composites demonstrate substantially higher rate constants and better model fits. MnFG1 shows remarkably high k values for RB5 (0.0153 min^{-1}) and IC+RB5 (0.0193 min^{-1}), with excellent correlation coefficients (R^2 = 0.9971 and 0.9720, respectively). This confirms that MnFG1 provides the most favorable conditions for the photocatalytic degradation of these dyes.

Interestingly, for IC degradation, MnFG3 exhibits the highest rate constant (0.0328 min^{-1}), followed closely by MnFG2 (0.0318 min^{-1}) and MnFG1 (0.0298 min^{-1}), all with satisfactory correlation coefficients (R^2 > 0.85). Similarly, for TC degradation, MnFG3 shows the highest k value (0.0072 min^{-1}) with an excellent model fit (R^2 = 0.9982). These results suggest that different composites may be optimal for different contaminants, depending on the specific interaction mechanisms between the contaminant molecules and the catalyst surface.

Overall, the kinetic analysis confirms that the incorporation of g-C_3N_4 into $MnFe_2O_4$ significantly enhances the photocatalytic degradation rates of all tested contaminants. The optimal composition varies slightly depending on the target contaminant, but generally, MnFG1 provides the best overall performance, combining high degradation rates with excellent reproducibility and model fit.

5.2 Recommendation

5.2.1 Further studies should examine the influence of various environmental conditions, such as pH levels, temperature, and reaction times, on the degradation efficiency of the catalysts, helping to identify optimal operational parameters for practical applications in wastewater treatment.

5.1.2 Implement Scaled-Up Experiments. Assess the feasibility of scaling up the photocatalytic process for pilot-scale wastewater treatment systems to validate its effectiveness.

List of Bibliography

[1] Teoh, W.Y., "A Perspective on the Flame Spray Synthesis of Photocatalyst Nanoparticles," **Materials**, 6, 8, 2013: pp.3194-3212.

[2] Khan, A., J.C. Colmenares, and R. Gläser, "Lignin-based composite materials for photocatalysis and photovoltaics," **Lignin Chemistry**, 2020: pp.1-31.

[3] Xu, W., et al., "Synergy mechanism for TiO_2/activated carbon composite material: Photocatalytic degradation of methylene blue solution," T**he Canadian Journal of Chemical Engineering**,100, 2, 2022: pp.276-290.

[4] Qian, Y., F. Zhang, and H. Pang, "A review of MOFs and their composites-based photocatalysts: synthesis and applications," **Advanced Functional Materials**, 31, 37, 2021: pp.2104231.

[5] Constantino, D.S., et al., "Intensification strategies for improving the performance of photocatalytic processes: A review," **Journal of Cleaner Production**, 340, 2022: pp.130800.

[6] Akurati, K.K., et al., "Flame-made WO3/TiO2 nanoparticles: relation between surface acidity, structure and photocatalytic activity," **Applied Catalysis B**: Environmental,79, 1, 2008: pp.53-62.

[7] Siriwong, C., et al., "Doped-metal oxide nanoparticles for use as photocatalysts," **Progress in crystal growth and characterization of materials**, 58, 2-3, 2012: pp.145-163.

[8] Ong, C.B., L.Y. Ng, and A.W. Mohammad, "A review of ZnO nanoparticles as solar photocatalysts: Synthesis, mechanisms and applications," **Renewable and Sustainable Energy Reviews**, 81, 2018: pp.536-551.

[9] Wang, C.-C., et al., "Photocatalytic organic pollutants degradation in metal–organic frameworks," **Energy & Environmental Science,**7, 9, 2014: pp.2831-2867.

[10] Khan, S.H. and B. Pathak, "Zinc oxide based photocatalytic degradation of persistent pesticides: A comprehensive review," **Environmental Nanotechnology, Monitoring & Management,** 13, 2020: pp.100290.

List of Bibliography (Continued)

[11] Dong, S., et al., "Recent developments in heterogeneous photocatalytic water treatment using visible light-responsive photocatalysts: a review," **Rsc Advances**, 5, 19, 2015: pp.14610-14630.

[12] Yao, H., et al., "Magnetic titanium dioxide based nanomaterials: synthesis, characteristics, and photocatalytic application in pollutant degradation," **Journal of Materials Chemistry A**, 3, 34, 2015: pp.17511-17524.

[13] Velempini, T., E. Prabakaran, and K. Pillay, "Recent developments in the use of metal oxides for photocatalytic degradation of pharmaceutical pollutants in water—A review," **Materials Today Chemistry,** 19, 2021: pp.100380.

[14] Koe, W.S., et al., "An overview of photocatalytic degradation: photocatalysts, mechanisms, and development of photocatalytic membrane," **Environmental Science and Pollution Research**, 27, 3, 2020: pp.2522-2565.

[15] Kallawar, G.A., D.P. Barai, and B.A. Bhanvase, "Bismuth titanate based photocatalysts for degradation of persistent organic compounds in wastewater: A comprehensive review on synthesis methods, performance as photocatalyst and challenges," **Journal of Cleaner Production**, 318, 2021: pp.128563.

[16] Byrne, C., G. Subramanian, and S.C. Pillai, "Recent advances in photocatalysis for environmental applications," **Journal of Environmental Chemical Engineering**, 6, 3, 2018: pp.3531-3555.

[17] Yang, R., et al., "One-step preparation (3D/2D/2D) $BiVO_4/FeVO_4$@rGO heterojunction composite photocatalyst for the removal of tetracycline and hexavalent chromium ions in water," **Chemical Engineering Journal**,390, 2020: pp.124522.

[18] Enesca, A. and L. Andronic, "UV-Vis Activated Cu(2)O/SnO(2)/WO(3) Heterostructure for Photocatalytic Removal of Pesticides," **Nanomaterials (Basel),**12, 15, 2022:

[19] Ghamarpoor, R., A. Fallah, and M. Jamshidi, "A Review of Synthesis Methods, Modifications, and Mechanisms of ZnO/TiO_2-Based Photocatalysts for Photodegradation of Contaminants," **ACS Omega**, 9, 24, 2024: pp.25457-25492.

List of Bibliography (Continued)

[20] Dai, Y. and Y. Xiong, "Control of selectivity in organic synthesis via heterogeneous photocatalysis under visible light," **Nano Research Energy**,1, 2022: pp.9120006.

[21] Ahmed, M.A. and A.A. Mohamed, "Recent progress in semiconductor/graphene photocatalysts: synthesis, photocatalytic applications, and challenges," **RSC Adv**,13, 1, 2022: pp.421-439.

[22] Mori, S., et al., "Artificial photosynthesis directed toward organic synthesis," **Nature Communications**,16, 1, 2025: pp.1797.

[23] Samadi, M. and A.Z. Moshfegh, "Recent Developments of Electrospinning-Based Photocatalysts in Degradation of Organic Pollutants: Principles and Strategies," **ACS Omega**,7, 50, 2022: pp.45867-45881.

[24] Mohammed, A.M., et al., "A review of research trends on the usage of photocatalysis for wastewater treatment: bibliometric analysis," **Sustain Water Resour Manag**,9, 3, 2023: pp.88.

[25] Alkaabi, M., et al., "Design of a Microfluidic Photocatalytic Reactor for Removal of Volatile Organic Components: Process Simulation and Techno-Economic Assessment," **ACS Omega**,7, 10, 2022: pp.8306-8313.

[26] Banoth, P., et al., "Single-phase $BiFeO_3$ and $BiFeO_3$-Fe_2O_3 nanocomposite photocatalysts for photodegradation of organic dye pollutants," **Nanoscale Adv**,5, 9, 2023: pp.2646-2656.

[27] Raha, S. and M. Ahmaruzzaman, "Novel magnetically retrievable $In_2O_3/MoS_2/Fe_3O_4$ nanocomposite materials for enhanced photocatalytic performance," **Sci Rep**,11, 1, 2021: pp.6379.

[28] Pelaez, M., et al., "A review on the visible light active titanium dioxide photocatalysts for environmental applications," **Applied Catalysis B: Environmental**,125, 2012: pp.331-349.

[29] Liang, Z., et al., "Covalent organic frameworks: Fundamentals, mechanisms, modification, and applications in photocatalysis," **Chem Catalysis**,2, 9, 2022: pp.2157-2228.

List of Bibliography (Continued)

[30] Mohammed, A., et al., "A review of research trends on the usage of photocatalysis for wastewater treatment: bibliometric analysis," **Sustainable Water Resources Management**,9, 2023:

[31] Warren, Z., et al., "Photocatalytic foams for water treatment: A systematic review and meta-analysis," J**ournal of Environmental Chemical Engineering,**11, 1, 2023: pp.109238.

[32] Qian, R., et al., "Charge carrier trapping, recombination and transfer during TiO_2 photocatalysis," **An overview**,335, 2019: pp.78-90.

[33] Melchionna, M. and P. Fornasiero, "Updates on the Roadmap for Photocatalysis," **ACS Catalysis**,10, 10, 2020: pp.5493-5501.

[34] Ahmed, M.A., S.A. Mahmoud, and A.A. Mohamed, "Unveiling the photocatalytic potential of graphitic carbon nitride (g-C_3N_4): a state-of-the-art review," **RSC Advances**,14, 35, 2024: pp.25629-25662.

[35] Fernández-Catalá, J., et al., "g-C_3N_4-Based Direct Z-Scheme Photocatalysts for Environmental Applications," **Catalysts**,12, 10, 2022: pp.1137.

[36] Dhanalaxmi, K., et al., "$MnFe_2O_4$ Nanocrystals Wrapped in a Porous Organic Polymer: A Designed Architecture for Water-Splitting Photocatalysis," **Chemistry–A European Journal**,22, 44, 2016: pp.15639-15644.

[37] Antonopoulou, M., "Homogeneous and Heterogeneous Photocatalysis for the Treatment of Pharmaceutical Industry Wastewaters: A Review," **Toxics**,10, 9, 2022:

[38] Guillard, C. and D. Robert, "Fifty Years of Research in Environmental Photocatalysis: Scientific Advances, Discoveries, and New Perspectives," **Catalysts**,14, 8, 2024: pp.547.

[39] Skliri, E., et al., "Mesoporous Composite Networks of Linked $MnFe_2O_4$ and $ZnFe_2O_4$ Nanoparticles as Efficient Photocatalysts for the Reduction of Cr(VI)," **Catalysts**,11, 2, 2021: pp.199.

[40] Zhang, Z., et al., "Role of Particle Size in Nanocrystalline TiO_2-Based Photocatalysts," **The Journal of Physical Chemistry B,**102, 52, 1998: pp.10871-10878.

List of Bibliography (Continued)

[41] Al-Zahrani, S.A., et al., "Influence of Ce^{3+} on the Structural, Morphological, Magnetic, Photocatalytic and Antibacterial Properties of Spinel $MnFe_2O_4$ Nanocrystallites Prepared by the Combustion Route," **Crystals**,12, 2, 2022: pp.268.

[42] Simon, C., et al., "Magnetic properties and structural analysis on spinel $MnFe_2O_4$ nanoparticles prepared via non-aqueous microwave synthesis," **Zeitschrift für anorganische und allgemeine Chemie**,647, 22, 2021: pp.2061-2072.

[43] Lotfi, M., et al., "Visible light-induced photocatalytic performance of green $MnFe_2O_4$ and $CoFe_2O_4$ nanoparticles," **Caspian Journal of Environmental Sciences**,2023: pp.1-10.

[44] Okla, M.K., et al., "Fabrication of $MnFe_2O_4$ spheres modified CeO_2 nano-flakes for sustainable photodegradation of MB dye and antimicrobial activity: A brief computational investigation on reactive sites and degradation pathway," **Colloids and Surfaces A: Physicochemical and Engineering Aspects**,641, 2022: pp.128566.

[45] Fuladi, V., et al., "Photocatalytic aspect of rGO/$MnFe_2O_4$ as an efficient magnetically retrievable catalyst for reduction of nitroaromatic compounds under visible-light irradiation," **Journal of Environmental Chemical Engineering**,10, 5, 2022: pp.108368.

[46] Madkour, L.H., "Graphitic Carbon Nitride Quantum Dots (g-C_3N_4): Fundamentals and Applications," **International Research Journal of Basic and Clinical Studies,**48, 2023:

[47] Bhanderi, D., P. Lakhani, and C.K. Modi, "Graphitic carbon nitride (g-C_3N_4) as an emerging photocatalyst for sustainable environmental applications: a comprehensive review," **RSC Sustainability,**2, 2, 2024: pp.265-287.

[48] Liang, D., et al., "Photocatalytic Properties of g-C_6N_6/g-C_3N_4 Heterostructure: A Theoretical Study," T**he Journal of Physical Chemistry C**,120, 42, 2016: pp.24023-24029.

[49] Paul, D.R., et al., "ZnO-Modified g-C_3N_4: A Potential Photocatalyst for Environmental Application," **ACS Omega**,5, 8, 2020: pp.3828-3838.

List of Bibliography (Continued)

[50] Stoia, M., C. Muntean, and B. Militaru, "$MnFe_2O_4$ nanoparticles as new catalyst for oxidative degradation of phenol by peroxydisulfate," J**ournal of Environmental Sciences,**53, 2017: pp.269-277.

[51] Dong, J., et al., "g-C_3N_4: Properties, Pore Modifications, and Photocatalytic Applications," **Nanomaterials (Basel)**,12, 1, 2021:

[52] Islam, K., et al., "Manganese Ferrite Nanoparticles $MnFe_2O_4$: Size Dependence for Hyperthermia and Negative/Positive Contrast Enhancement in MRI," **Nanomaterials (Basel)**,10, 11, 2020:

[53] Rahmayanti, R. and S. Sudiati, "Synthesis of $MnFe_2O_4$ Nanoparticles as a Basic Material for Microwave Absorber," **Journal of Technomaterial Physics**,4, 2, 2022: pp.80-86.

[54] Dippong, T., et al., "A Strategy for Tuning the Structure, Morphology, and Magnetic Properties of $MnFe_2O_4/SiO_2$ Ceramic Nanocomposites via Mono-, Di-, and Trivalent Metal Ion Doping and Annealing," **Nanomaterials (Basel)**,13, 14, 2023:

[55] Chitra Devi, E. and I. Soibam, "Structural and optical characterization of $MnFe_2O_4$ nanoparticles," **Advanced Materials Proceedings**,2, 2017: pp.93-96.

[56] Sharifi, S., K. Rahimi, and A. Yazdani, "Highly improved supercapacitance properties of $MnFe_2O_4$ nanoparticles by MoS_2 nanosheets," **Scientific Reports**,11, 1, 2021: pp.8378.

[57] Zhang, Y., et al., "Spinel $MnFe_2O_4$ nanoparticles (MFO-NPs) for CO_2 cyclic decomposition prepared from ferromanganese ores," **Ceramics International,**46, 9, 2020: pp.14206-14216.

[58] Liu, J., H. Wang, and M. Antonietti, "Graphitic carbon nitride "reloaded": emerging applications beyond (photo)catalysis," **Chem Soc Rev**,45, 8, 2016: pp.2308-26.

[59] Zhu, J., et al., "Graphitic carbon nitride: synthesis, properties, and applications in catalysis," **ACS Appl Mater Interfaces,**6, 19, 2014: pp.16449-65.

List of Bibliography (Continued)

[60] Dong, L., et al., "Band structure tuning of g-C_3N_4 via sulfur doping for broadband near-infrared ultrafast photonic applications," **Nanophotonics**,11, 1, 2022: pp.139-151.

[61] Shiraishi, Y., et al., "Highly Selective Production of Hydrogen Peroxide on Graphitic Carbon Nitride g-C_3N_4 Photocatalyst Activated by Visible Light," **ACS Catalysis,**4, 3, 2014: pp.774-780.

[62] Wang, W.-F., et al., "Morphology and element doping effects: phosphorus-doped hollow polygonal g-C_3N_4 rods for visible light-driven CO_2 reduction," **New Journal of Chemistry,**46, 6, 2022: pp.3017-3025.

[63] Huang, Z., et al., "A visible light active, carbon-nitrogen-sulfur co-doped TiO_2/g-C_3N_4 Z-scheme heterojunction as an effective photocatalyst to remove dye pollutants," **RSC Adv,**11, 27, 2021: pp.16747-16754.

[64] He, Y., et al., "New application of Z-scheme Ag_3PO_4/g-C_3N_4 composite in converting CO_2 to fuel," **Environ Sci Techno**l,49, 1, 2015: pp.649-56.

[65] Yuhaneka, G., et al., "Synthesis of Porous g-C_3N_4 and Its Application as Photocatalyst for Methylene Blue Degradation," **Malaysian Journal of Fundamental and Applied Sciences,**18, 4, 2022: pp.463-472.

[66] Alaghmandfard, A. and K. Ghandi, "A Comprehensive Review of Graphitic Carbon Nitride g-C_3N_4-Metal Oxide-Based Nanocomposites: Potential for Photocatalysis and Sensing," **Nanomaterials (Basel)**,12, 2, 2022:

[67] Ranjbakhsh, E. and M. Izadyar, "The theoretical investigation of the g-C_3N_4/ZnS heterojunction for photocatalytic applications," **Physical Chemistry Chemical Physics,**27, 6, 2025: pp.3061-3067.

[68] Janani, B.J., et al., "Robust advantage of MXene/g-C_3N_4 loaded on Fe_2WO_6/$BiIO_4$ nano-platform for chemo-peroxidase colorimetric detection of uranyl ions, antifungal properties, photocatalytic degradation of p-chlorophenol, and eco-toxicity studies," **Diamond and Related Materials**,145, 2024: pp.111129.

[69] Zhang, Y., et al., "MoS_2 and Fe_2O_3 co-modify g-C_3N_4 to improve the performance of photocatalytic hydrogen production," **Sci Rep**,12, 1, 2022: pp.3261.

List of Bibliography (Continued)

[70] Liu, F., et al., "Synthesis of a well-dispersed $CaFe_2O_4$/g-C_3N_4/CNT composite towards the degradation of toxic water pollutants under visible light," **RSC Adv**,9, 44, 2019: pp.25750-25761.

[71] Antunes, I., et al., "Thermodynamic Guidelines for the Mechanosynthesis or Solid-State Synthesis of $MnFe_2O_4$ at Relatively Low Temperatures," **Materials (Basel)**,17, 2, 2024:

[72] Wang, T., et al., "Facile one-step hydrothermal synthesis of α-Fe_2O_3/g-C_3N_4 composites for the synergistic adsorption and photodegradation of dyes," **RSC Adv**,9, 50, 2019: pp.29109-29119.

[73] He, T., et al., "Novel magnetic Fe_3O_4/g-C_3N_4/MoO_3 nanocomposites with highly enhanced photocatalytic activities: Visible-light-driven degradation of tetracycline from aqueous environment," **PLoS One**,15, 8, 2020: pp.e0237389.

[74] Angkaew, A., et al., "Two facile synthesis routes for magnetic recoverable $MnFe_2O_4$/g-C_3N_4 nanocomposites to enhance visible light photo-Fenton activity for methylene blue degradation," **Journal of Environmental Chemical Engineering**,9, 4, 2021: pp.105621.

[75] Bhuyan, B., et al., "A novel $MnFe_2O_4$/ Graphitic carbon nitride g-C_3N_4 nanocomposites as efficient magnetically retrievable catalyst in crossed aldol condensation," **Materials Letters**,218, 2018:

[76] Elhaddad, E. and A.T. Al-fawwaz, "Synthesis, Characterization and Mechanism of $MnFe_2O_4$@g-C_3N_4 Nanocomposite as an effective Photocatalyst for the Generation of Hydrogen and organic contamination degradation," **Egyptian Journal of Petroleum**,32, 2, 2023: pp.41-46.

[77] Nong, L.X. and O.T.K. Nguyen, "Synthesis of ZnO/NiO/g-C_3N_4 Nanocomposite Materials for Photocatalytic Degradation of Tetracycline Antibiotic," 2023: pp.11.

[78] Xie, D., et al., "Efficient RhB degradation using $MnFe_2O_4$/g-C_3N_4 composites under visible light irradiation," **Optical Materials,**124, 2022: pp.111965.

List of Bibliography (Continued)

[79] Al Mais, D., et al., "Various Morphologies of Graphitic Carbon Nitride g-C_3N_4 and Their Effect on the Thermomechanical Properties of Thermoset Epoxy Resin Composites," **Polymers**,16, 13, 2024: pp.1935.

[80] Alaghmandfard, A. and K. Ghandi, "A Comprehensive Review of Graphitic Carbon Nitride g-C_3N_4–Metal Oxide-Based Nanocomposites: Potential for Photocatalysis and Sensing," **Nanomaterials**,12, 2, 2022: pp.294.

[81] Wang, M., et al., "Synthesis of g-C_3N_4/$MnFe_3O_4$-basednanocomposites and application as a new sorbent for solid phase extraction of polycyclic aromatic hydrocarbons in water samples," **Talanta**,132, 2015: pp.922-8.

[82] Cako, E., et al., "Heterojunction of (P, S) co-doped g-C_3N_4 and 2D TiO_2 for improved carbamazepine and acetaminophen photocatalytic degradation," **Separation and Purification Technology**,311, 2023: pp.123320.

[83] Wang, H., et al., "Hydrothermal Synthesis of Nanooctahedra $MnFe_2O_4$ onto the Wood Surface with Soft Magnetism, Fire Resistance and Electromagnetic Wave Absorption," **Nanomaterials** (Basel),7, 6, 2017:

[84] Medvedeva, E.D., et al., "Synthesis of g-C_3N_4/WO_3 composites under hydrothermal conditions and study of their photocatalytic properties," **Materials Proceedings,**14, 1, 2023: pp.17.

[85] Li, D., et al., "One-pot hydrothermal synthesis of Mn_3O_4 nanorods grown on Ni foam for high performance supercapacitor applications," **Nanoscale Res Lett,**8, 1, 2013: pp.535.

[86] Ibadurrohman, M., et al., "Modification of hydrothermally synthesized α-Fe_2O_3 nanorods with g-C_3N_4 prepared from various precursors as photoanodes for hydrogen production," **New Journal of Chemistry**,48, 33, 2024: pp.14746-14756.

[87] Javed, M., et al., "Integration of Mn-$ZnFe_2O_4$ with S-g-C_3N_4 for Boosting Spatial Charge Generation and Separation as an Efficient Photocatalyst," **Molecules**,27, 20, 2022:

List of Bibliography (Continued)

[88] Elhaddad, E. and A.T. Al-fawwaz, "Synthesis, characterization and mechanism of $MnFe_2O_4$@g-C_3N_4 nanocomposite as an effective photocatalyst for the generation of hydrogen and organic contamination degradation," **Egyptian Journal of Petroleum**,32, 2, 2023: pp.41-46.

[89] Pham, M.-T., et al., "Rapid and scalable fabrication of TiO_2@ g-C_3N_4 heterojunction for highly efficient photocatalytic no removal under visible light," **Aerosol and Air Quality Research,**21, 12, 2021: pp.210276.

[90] Rana, A.G., Modification of Graphitic Carbon Nitride (g-C_3N_4) for photocatalytic redox reactions. 2022, **Technische Universität München.**

[91] Liu, X., et al., "The production discipline and mechanism of hydroxyl radical by investigating the Ln2O3-Bi2MoO6 heterojunction photocatalysts," J**ournal of Alloys and Compounds**,864, 2021: pp.158894.

[92] Tavares, M.F., et al., "Decolorization of azo and anthraquinone dyes by crude laccase produced by Lentinus crinitus in solid state cultivation," **Braz J Microbiol**,51, 1, 2020: pp.99-106.

[93] Singh, G.B., et al., "Azo dye bioremediation: An interdisciplinary path to sustainable fashion," **Environmental Technology & Innovation**,36, 2024: pp.103832.

[94] Ali, A.N., "A comprehensive study of natural and synthetic dyes: their properties, methods of preparation, and uses," S**HIFAA,2024**, 2024: pp.1-17.

[95] Ardila-Leal, L.D., et al., "A Brief History of Colour, the Environmental Impact of Synthetic Dyes and Removal by Using Laccases," **Molecules**,26, 13, 2021:

[96] Kamati, S.N., J. Yan, and J. Fan, "A review on progress in reactive dye-containing wastewater treatment," **Water Practice and Technology**,19, 7, 2024: pp.2712-2733.

[97] Berradi, M., et al., "Textile finishing dyes and their impact on aquatic environs," **Heliyon**,5, 11, 2019: pp e02711.

[98] Tripathi, M., et al., "Recent Strategies for the Remediation of Textile Dyes from Wastewater: A Systematic Review," **Toxics**,11, 11, 2023:

List of Bibliography (Continued)

[99] Kathing, C. and G. Saini, "A Review of Various Treatment Methods for the Removal of Dyes from Textile Effluent," **Recent Progress in Materials**,04, 04, 2022: pp.028.

[100] Zhang, J., et al., "Advanced enzyme-assembled hydrogels for the remediation of contaminated water," **Nature Communications,**16, 1, 2025: pp.3050.

[101] Ragab, M.M., A.G. Hassabo, and H. Othman, "An Overview of Natural Dyes Extraction Techniques for Valuable Utilization on Textile Fabrics," **Journal of Textiles, Coloration and Polymer Science**,19, 2, 2022: pp.137-153.

[102] El-Sayed, E., et al., "Azo dyes: Synthesis, Classification and Utilisation in Textile Industry," **Egyptian Journal of Chemistry**,67, 13, 2024: pp.87-97.

[103] Hamdy, D. and A. Hassabo, "Various Natural Dyes from Different Sources," **Journal of Textiles, Coloration and Polymer Science**, 2021

[104] Santiago, D., J. Cunha, and I. Cabral, "Chromatic and medicinal properties of six natural textile dyes: A review of eucalyptus, weld, madder, annatto, indigo and woad," **Heliyon**,9, 11, 2023: pp e22013.

[105] Liu, J., et al., "Anaerobic biodegradation of azo dye reactive black 5 by a novel strain Shewanella sp. SR1: Pathway and mechanisms," **J Environ Manage**,347, 2023: pp.119073.

[106] Lin, J., et al., "Environmental impacts and remediation of dye-containing wastewater," **Nature Reviews Earth & Environment**,4, 2023:

[107] Ristea, M.E. and O. Zarnescu, "Indigo Carmine: Between Necessity and Concern," **J Xenobiot**,13, 3, 2023: pp.509-528.

[108] Mehra, S., M. Singh, and P. Chadha, "Adverse impact of textile dyes on the aquatic environment as well as on human beings," T**oxicology International,2021**: pp.165-176.

[109] Hassaan, M.A., A. El Nemr, and A. Hassaan, "Health and environmental impacts of dyes: mini review," **American Journal of Environmental Science and Engineering,**1, 3, 2017: pp.64-67.

List of Bibliography (Continued)

[110] Muslimah, E., A.R. Suwarno, and S. Nandiroh. Life Cycle Assessment (LCA) analysis on the dyeing process to increase sustainable production in batik SMEs. In E3S Web of Conferences. **2024. EDP Sciences.**

[111] Jabbariesgandani, A. and J.L. Walsh, "Factors affecting decolourization efficiency of indigo carmine in a coaxial surface plasma falling film reactor," **Journal of Water Process Engineering,**53, 2023: pp.103632.

[112] Crema, A.P.S., et al., "Degradation of indigo carmine in water induced by non-thermal plasma, ozone and hydrogen peroxide: A comparative study and by-product identification," **Chemosphere**,244, 2020: pp.125502.

[113] El Bouraie, M. and W.S. El Din, "Biodegradation of Reactive Black 5 by Aeromonas hydrophila strain isolated from dye-contaminated textile wastewater," **Sustainable Environment Research**,26, 5, 2016: pp.209-216.

[114] Borghi, A.A. and M.S.A. Palma, "Tetracycline: production, waste treatment and environmental impact assessment," **Brazilian Journal of Pharmaceutical Sciences,**50, 2014: pp.25-40.

[115] Gopal, G., et al., "A review on tetracycline removal from aqueous systems by advanced treatment techniques," **RSC Advances**,10, 45, 2020: pp.27081-27095.

[116] Zhan, L., et al., "Study on the remediation of tetracycline antibiotics and roxarsone contaminated soil," **Environ Pollution**,271, 2021: pp.116312.

[117] Zolekafeli, Z., et al., "Removal of Tetracycline Using Tungsten Disulfide/Graphene Oxide as Photocatalyst: Effect of Light Irradiation and Kinetic Studies," 2024: pp.9.

[118] Lalrindiki, F., N. Premjit Singh, and N. Mohondas Singh, "A review of synthesis, photocatalytic, photoluminescence and antibacterial properties of bismuth vanadate-based nanomaterial," **Inorganic Chemistry Communications,**168, 2024: pp.112846.

List of Bibliography (Continued)

[119] Chapter 3 - The Current Situation in Ultra-Precision Technology – Silicon Single Crystals as an Example, in Advances in CMP Polishing Technologies, T. Doi, I.D. Marinescu, and S. Kurokawa, Editors. 2012, William Andrew Publishing: Oxford. p. 15-111.

[120] Zhang, M., et al., "The Intrinsic Relationship between Photoluminescence and Photocatalysis of MMoO4/MWO4 (M = Mg, Ca, Sr and Ba) Heterojunctions: Heterojunction Construction, Mechanism Insight and Development Tendency," **Micromachines**,15, 7, 2024: pp.878.

[121] Holder, C.F. and R.E. Schaak, "Tutorial on Powder X-ray Diffraction for Characterizing Nanoscale Materials," **ACS Nano,**13, 7, 2019: pp.7359-7365.

[122] Ischenko, A., et al., "Analysis of nanoparticles and nanomaterials using X-ray photoelectron spectroscopy," **Fine Chemical Technologies**,18, 2, 2023: pp.135-167.

[123] Morozzi, P., et al., "Ultraviolet–Visible Diffuse Reflectance Spectroscopy (UV–Vis DRS), a rapid and non-destructive analytical tool for the identification of Saharan dust events in particulate matter filters," **Atmospheric Environment**,252, 2021: pp.118297.

[124] Escobedo Morales, A., E. Sánchez Mora, and U. Pal, "Use of Diffuse Reflectance Spectroscopy for Optical Characterization of Un-Supported Nanostructures," 67.Bf,53, 2007:

[125] Morales, A.E., E.S. Mora, and U. Pal, "Use of diffuse reflectance spectroscopy for optical characterization of unsupported nanostructures," **Revista mexicana de física**,53, 5, 2007: pp.18-22.

[126] Poomipuen, K., et al., "Dual Activation of Peroxymonosulfate Using $MnFe_2O_4$/g-C_3N_4 and Visible Light for the Efficient Degradation of Steroid Hormones: Performance, Mechanisms, and Environmental Impacts," **ACS Omega,**8, 39, 2023: pp.36136-36151.

List of Bibliography (Continued)

[127] Javed, M., et al., "Integration of Mn-$ZnFe_2O_4$ with S-g-C_3N_4 for Boosting Spatial Charge Generation and Separation as an Efficient Photocatalyst," **Molecules**, 27, 20, 2022: pp.6925.

[128] Tessema, A.A., C.-M. Wu, and K.G. Motora, "Highly Efficient Solar Light Driven g-C_3N_4@$Cs0.33WO_3$ Heterojunction for the Photodegradation of Colorless Antibiotics," **ACS Omega**,7, 43, 2022: pp.38475-38486.

[129] Yuan, N., et al., "What Is the Transfer Mechanism of Photoexcited Charge Carriers for g-C_3N_4/TiO_2 Heterojunction Photocatalysts? Verification of the Relative p–n Junction Theory," **The Journal of Physical Chemistry C**,124, 16, 2020: pp.8561-8575.

[130] Godin, R., et al., "Time-Resolved Spectroscopic Investigation of Charge Trapping in Carbon Nitrides Photocatalysts for Hydrogen Generation," **Journal of the American Chemical Society**, 139, 14, 2017: pp.5216-5224.

[131] Aljuaid, A., et al., "g-C_3N_4 Based Photocatalyst for the Efficient Photodegradation of Toxic Methyl Orange Dye: Recent Modifications and Future Perspectives," **Molecules,** 28, 7, 2023:

[132] Vignesh, K., et al., "Photocatalytic activity of magnetically recoverable MnFe2O4/g-C3N4/TiO2 nanocomposite under simulated solar light irradiation," **Journal of Molecular Catalysis A: Chemical**, 395, 2014: pp.373-383.

[133] Manohar, A., et al., "Synthesis and characterization of Mg2+ substituted $MnFe_2O_4$ nanoparticles for supercapacitor applications," **Ceramics International**, 48, 20, 2022: pp.30695-30703.

[134] Muramatsu, H., E. Tamiya, and I. Karube, "Computation of equivalent circuit parameters of quartz crystals in contact with liquids and study of liquid properties," **Analytical Chemistry**, 60, 19, 1988: pp.2142-2146.

[135] Amulya, M.A.S., et al., "Sonochemical synthesis of $MnFe_2O_4$ nanoparticles and their electrochemical and photocatalytic properties," **Journal of Physics and Chemistry of Solids**,148, 2021: pp.109661.

List of Bibliography (Continued)

[136] Singh Yadav, R., et al., "Impact of sonochemical synthesis condition on the structural and physical properties of MnFe2O4 spinel ferrite nanoparticles," **Ultrasonics Sonochemistry,** 61, 2020: pp.104839.

[137] Mao, K., et al., "New Efficient Visible-Light-Driven Photocatalyst of Chitin-Modified Titanium Dioxide/Carbon Fiber Composites for Wastewater," **Scientific Reports,** 9, 1, 2019: pp.16321.

APPENDICES

APPENDIX A

Experimental results

Table A1 Treatment of IC dye in synthetic wastewater at an initial concentration of 50 ppm of Experiment condition 1 (Control).

Time	Abs			Concentration			C/C_0	%
(min)	1	2	Avg	1	2	Avg		Removal
0	1.996	1.996	1.996	48.583	48.583	48.58	1.000	0.00
10	1.858	1.874	1.866	45.224	45.613	45.42	0.935	6.51
180	1.867	1.773	1.820	45.443	43.155	44.30	0.912	8.82

Table A2 Treatment of IC dye in synthetic wastewater at an initial concentration of 50 ppm of Experiment condition 2 (Control).

Time	Abs			Concentration			C/C_0	%
(min)	1	2	Avg	1	2	Avg		Removal
0	1.989	1.989	1.989	48.412	48.412	48.41	1.000	0.00
10	1.820	1.818	1.819	44.299	44.250	44.27	0.915	8.55
180	1.832	1.834	1.833	44.591	44.640	44.62	0.922	7.84

Table A3 Treatment of IC dye in synthetic wastewater at an initial concentration of 50 ppm of Experiment condition 3 with MnF photocatalyst (Control).

Time	Abs			Concentration			C/C_0	%
(min)	1	2	Avg	1	2	Avg		Removal
0	1.996	1.996	1.996	48.583	48.583	48.58	1.000	0.00
10	1.838	1.852	1.845	44.737	45.078	44.91	0.924	7.57
180	1.824	1.853	1.839	44.396	45.102	44.75	0.921	7.89

Table A4 Treatment of IC dye in synthetic wastewater at an initial concentration of 50 ppm of Experiment condition 3 with MnFG1 photocatalyst (Control).

Time	Abs			Concentration			C/C_0	%
(min)	1	2	Avg	1	2	Avg		Removal
0	1.989	1.989	1.989	48.412	48.412	48.41	1.000	0.00
10	1.725	1.721	1.723	41.987	41.889	41.94	0.866	13.37
180	1.725	1.725	1.725	41.987	41.987	41.99	0.867	13.27

Table A5 Treatment of IC dye in synthetic wastewater at an initial concentration of 50 ppm of Experiment condition 3 with MnFG2 photocatalyst (Control).

Time	Abs			Concentration			C/C_0	%
(min)	1	2	Avg	1	2	Avg		Removal
0	1.989	1.989	1.989	48.412	48.412	48.41	1.000	0.00
10	1.784	1.787	1.786	43.423	43.496	43.46	0.898	10.23
180	1.779	1.777	1.778	43.301	43.252	43.28	0.894	10.61

Table A6 Treatment of IC dye in synthetic wastewater at an initial concentration of 50 ppm of Experiment condition 3 with MnFG3 photocatalyst (Control).

Time	Abs			Concentration			C/C_0	%
(min)	1	2	Avg	1	2	Avg		Removal
0	1.989	1.989	1.989	48.412	48.412	48.41	1.000	0.00
10	1.692	1.698	1.695	41.183	41.329	41.26	0.852	14.78
180	1.780	1.783	1.782	43.325	43.398	43.36	0.896	10.43

Table A7 Treatment of IC dye in synthetic wastewater by the photocatalytic process at an initial concentration of 50 ppm of Experiment condition 4 with MnF photocatalyst.

Time (min)	(Abs)			Concentration (mg. L^{-1})			% Removal	$\ln(C_0/C)$
	1	2	Avg	1	2	Avg		
0	1.967	1.967	1.967	47.877	47.877	47.88	0.00	0.00
10	1.585	1.582	1.584	38.579	38.506	38.54	19.50	0.22
20	1.563	1.562	1.562	38.040	38.007	38.02	20.58	0.23
30	1.541	1.541	1.541	37.502	37.508	37.50	21.66	0.24
40	1.519	1.521	1.520	36.963	37.009	36.99	22.75	0.26
60	1.497	1.500	1.498	36.425	36.510	36.47	23.83	0.27
90	1.452	1.459	1.456	35.348	35.512	35.43	26.00	0.30
120	1.430	1.439	1.434	34.809	35.013	34.91	27.08	0.32
150	1.419	1.428	1.424	34.540	34.764	34.65	27.62	0.32
180	1.408	1.418	1.413	34.271	34.514	34.39	28.16	0.33

Table A8 Treatment of IC dye in synthetic wastewater by the photocatalytic process at an initial concentration of 50 ppm of Experiment condition 4 with MnFG1 photocatalyst.

Time (min)	(Abs)			Concentration (mg. L^{-1})			% Removal	$\ln(C_0/C)$
	1	2	Avg	1	2	Avg		
0	2.055	2.055	2.055	50.019	50.019	50.02	0.00	0.00
10	1.558	1.515	1.537	37.922	36.875	37.40	25.23	0.29
20	1.364	1.405	1.385	33.200	34.198	33.70	32.63	0.39
30	1.120	1.242	1.181	27.261	30.230	28.75	42.53	0.55
40	0.901	1.009	0.955	21.930	24.559	23.24	53.53	0.77
60	0.441	0.605	0.523	10.734	14.726	12.73	74.55	1.37
90	0.057	0.207	0.132	1.387	5.038	3.21	93.58	2.75
120	0.020	0.020	0.020	0.487	0.487	0.49	99.03	4.63
150	0.017	0.018	0.018	0.414	0.438	0.43	99.15	4.77
180	0.021	0.016	0.019	0.511	0.389	0.45	99.10	4.71

Table A9 Treatment of IC dye in synthetic wastewater by the photocatalytic process at an initial concentration of 50 ppm of Experiment condition 4 with MnFG2 photocatalyst.

Time (min)	(Abs)			Concentration (mg. L^{-1})			% Removal	ADMI	$\ln(C_0/C)$
	1	2	Avg	1	2	Avg			
0	2.055	2.055	2.055	50.019	50.019	50.02	0.00	4836	0.00
10	1.662	1.672	1.667	40.453	40.696	40.57	18.88	3923	0.21
20	1.433	1.294	1.364	34.879	31.496	33.19	33.65	3209	0.41
30	1.120	0.951	1.036	27.261	23.147	25.20	49.61	2437	0.69
40	0.865	0.604	0.735	21.054	14.701	17.88	64.26	1728	1.03
60	0.260	0.045	0.153	6.328	1.095	3.71	92.58	359	2.60
90	0.019	0.018	0.019	0.462	0.438	0.45	99.10	44	4.71
120	0.018	0.017	0.018	0.438	0.414	0.43	99.15	41	4.77
150	0.020	0.021	0.021	0.487	0.511	0.50	99.00	48	4.61
180	0.019	0.020	0.020	0.462	0.487	0.47	99.05	46	4.66

Table A10 Treatment of IC dye in synthetic wastewater by the photocatalytic process at an initial concentration of 50 ppm of Experiment condition 4 with MnFG3 photocatalyst.

Time	(Abs)			Concentration (mg. L^{-1})			%	ADMI	$\ln(C_0/C)$
(min)	1	2	Avg	1	2	Avg	Removal		
0	1.996	1.996	1.996	48.583	48.583	48.58	0.00	4697	0.00
10	1.549	1.675	1.612	37.703	40.770	39.24	19.24	3793	0.21
20	1.208	1.461	1.335	29.403	35.561	32.48	33.14	3140	0.40
30	0.886	1.205	1.046	21.565	29.330	25.45	47.62	2460	0.65
40	0.562	0.941	0.752	13.679	22.904	18.29	62.35	1768	0.98
60	0.122	0.251	0.187	2.969	6.109	4.54	90.66	439	2.37
90	0.021	0.022	0.022	0.511	0.535	0.52	98.92	51	4.53
120	0.021	0.023	0.022	0.511	0.560	0.54	98.90	52	4.51
150	0.022	0.021	0.022	0.535	0.511	0.52	98.92	51	4.53
180	0.020	0.019	0.020	0.487	0.462	0.47	99.02	46	4.63

Table A11 Treatment of RB5 dye in synthetic wastewater at an initial concentration of 50 ppm of Experiment condition 1 (Control).

Time	Abs			Concentration			C/C_0	%
(min)	1	2	Avg	1	2	Avg		Removal
0	1.181	1.181	1.181	52.445	52.445	52.445	1.000	0.000
10	1.077	1.070	1.074	47.826	47.515	47.671	0.909	9.102
180	1.053	1.049	1.051	46.776	46.596	46.686	0.890	10.980

Table A12 Treatment of RB5 dye in synthetic wastewater at an initial concentration of 50 ppm of Experiment condition 2 (Control).

Time	Abs			Concentration			C/C_0	%
(min)	1	2	Avg	1	2	Avg		Removal
0	1.181	1.181	1.181	52.445	52.445	52.445	1.000	0.000
10	1.088	1.090	1.089	48.315	48.404	48.359	0.922	7.790
180	1.065	1.061	1.063	47.297	47.124	47.210	0.900	9.980

Table A13 Treatment of RB5 dye in synthetic wastewater at an initial concentration of 50 ppm of Experiment condition 3 with MnF photocatalyst (Control).

Time	Abs			Concentration			C/C_0	%
(min)	1	2	Avg	1	2	Avg		Removal
0	1.181	1.181	1.181	52.445	52.445	52.445	1.000	0.000
10	0.828	0.825	0.827	36.769	36.636	36.702	0.700	30.017
180	0.711	0.711	0.711	31.583	31.581	31.582	0.602	39.780

Table A14 Treatment of RB5 dye in synthetic wastewater at an initial concentration of 50 ppm of Experiment condition 3 with MnFG1 photocatalyst (Control).

Time	Abs			Concentration			C/C_0	%
(min)	1	2	Avg	1	2	Avg		Removal
0	1.181	1.181	1.181	52.445	52.445	52.445	1.000	0.000
10	0.958	0.956	0.957	42.542	42.453	42.497	0.810	18.967
180	0.913	0.912	0.912	40.540	40.484	40.512	0.772	22.753

Table A15 Treatment of RB5 dye in synthetic wastewater at an initial concentration of 50 ppm of Experiment condition 3 with MnFG2 photocatalyst (Control).

Time	Abs			Concentration			C/C_0	%
(min)	1	2	Avg	1	2	Avg		Removal
0	1.181	1.181	1.181	52.445	52.445	52.445	1.000	0.000
10	1.064	1.063	1.064	47.249	47.205	47.227	0.901	9.949
180	1.008	1.009	1.008	44.755	44.809	44.782	0.854	14.612

Table A16 Treatment of RB5 dye in synthetic wastewater at an initial concentration of 50 ppm of Experiment condition 3 with MnFG3 photocatalyst (Control).

Time	Abs			Concentration			C/C_0	%
(min)	1	2	Avg	1	2	Avg		Removal
0	1.181	1.181	1.181	52.445	52.445	52.445	1.000	0.000
10	1.029	1.026	1.028	45.695	45.562	45.628	0.870	12.997
180	0.991	0.992	0.992	44.021	44.052	44.036	0.840	16.033

Table A17 Treatment of RB5 dye in synthetic wastewater by the photocatalytic process at an initial concentration of 50 ppm of Experiment condition 4 with MnF photocatalyst.

Time (min)	(Abs)			Concentration (mg. L^{-1})			% Removal	$\ln(C_0/C)$
	1	2	Avg	1	2	Avg		
0	1.181	1.181	1.181	52.445	52.445	52.445	0.000	0.000
10	0.818	0.821	0.820	36.325	36.458	36.392	30.610	0.365
20	0.770	0.767	0.769	34.193	34.060	34.127	34.928	0.430
30	0.744	0.742	0.743	33.039	32.950	32.994	37.087	0.463
40	0.726	0.726	0.726	32.239	32.239	32.239	38.527	0.487
60	0.687	0.688	0.688	30.508	30.552	30.530	41.787	0.541
90	0.663	0.664	0.664	29.442	29.486	29.464	43.819	0.577
120	0.636	0.633	0.635	28.243	28.110	28.176	46.274	0.621
150	0.599	0.602	0.601	26.600	26.733	26.666	49.153	0.676
180	0.605	0.608	0.607	26.866	26.999	26.933	48.645	0.666

Table A18 Treatment of RB5 dye in synthetic wastewater by the photocatalytic process at an initial concentration of 50 ppm of Experiment condition 4 with MnFG1 photocatalyst.

Time (min)	(Abs)			Concentration (mg. L^{-1})			% Removal	$\ln(C_0/C)$
	1	2	Avg	1	2	Avg		
0	1.181	1.181	1.181	52.445	52.445	52.445	0.000	0.000
10	0.887	0.883	0.885	39.389	39.211	39.300	25.064	0.289
20	0.773	0.775	0.774	34.327	34.415	34.371	34.462	0.423
30	0.693	0.694	0.694	30.774	30.818	30.796	41.279	0.532
40	0.620	0.619	0.620	27.532	27.488	27.510	47.544	0.645
60	0.469	0.465	0.467	20.827	20.649	20.738	60.457	0.928
90	0.293	0.290	0.292	13.011	12.878	12.945	75.318	1.399
120	0.177	0.175	0.176	7.860	7.771	7.816	85.097	1.904
150	0.121	0.120	0.121	5.373	5.329	5.351	89.797	2.282
180	0.084	0.081	0.083	3.730	3.597	3.664	93.014	2.661

Table A19 Treatment of RB5 dye in synthetic wastewater by the photocatalytic process at an initial concentration of 50 ppm of Experiment condition 4 with MnFG2 photocatalyst.

Time (min)	(Abs)			Concentration (mg. L^{-1})			% Removal	$\ln(C_0/C)$
	1	2	Avg	1	2	Avg		
0	1.181	1.181	1.181	52.445	52.445	52.445	0.000	0.000
10	0.997	0.994	0.996	44.274	44.141	44.207	15.707	0.171
20	0.922	0.919	0.921	40.943	40.810	40.877	22.058	0.249
30	0.835	0.837	0.836	37.080	37.169	37.124	29.213	0.345
40	0.787	0.791	0.789	34.948	35.126	35.037	33.192	0.403
60	0.655	0.657	0.656	29.087	29.175	29.131	44.454	0.588
90	0.426	0.429	0.428	18.917	19.051	18.984	63.802	1.016
120	0.278	0.279	0.279	12.345	12.390	12.367	76.418	1.445
150	0.191	0.194	0.193	8.482	8.615	8.548	83.700	1.814
180	0.125	0.128	0.127	5.551	5.684	5.617	89.289	2.234

Table A20 Treatment of RB5 dye in synthetic wastewater by the photocatalytic process at an initial concentration of 50 ppm of Experiment condition 4 with MnFG3 photocatalyst.

Time (min)	(Abs)			Concentration (mg. L^{-1})			% Removal	$\ln(C_0/C)$
	1	2	Avg	1	2	Avg		
0	1.181	1.181	1.181	52.445	52.445	52.445	0.000	0.000
10	0.933	0.934	0.934	41.432	41.476	41.454	20.957	0.235
20	0.847	0.853	0.850	37.613	37.879	37.746	28.027	0.329
30	0.761	0.759	0.760	33.794	33.705	33.749	35.648	0.441
40	0.620	0.653	0.637	27.532	28.998	28.265	46.105	0.618
60	0.513	0.510	0.512	22.781	22.648	22.714	56.689	0.837
90	0.347	0.346	0.347	15.409	15.365	15.387	70.660	1.226
120	0.246	0.243	0.245	10.924	10.791	10.858	79.297	1.575
150	0.159	0.156	0.158	7.061	6.927	6.994	86.664	2.015
180	0.137	0.138	0.138	6.084	6.128	6.106	88.357	2.150

Table A21 Treatment of IC+RB5 dye in synthetic wastewater at an initial concentration of 50 ppm of Experiment condition 1 (Control).

Time	Abs			Concentration			C/C_0	%
(min)	1	2	Avg	1	2	Avg		Removal
0	1.516	1.516	1.516	23.701	23.701	23.70	1.000	0.00
10	1.434	1.459	1.447	22.419	22.810	22.61	0.954	4.58
180	1.397	1.403	1.400	21.841	21.935	21.89	0.923	7.65

Table A22 Treatment of IC+RB5 dye in synthetic wastewater at an initial concentration of 50 ppm of Experiment condition 2 (Control).

Time	Abs			Concentration			C/C_0	%
(min)	1	2	Avg	1	2	Avg		Removal
0	1.524	1.524	1.524	23.826	23.826	23.83	1.000	0.00
10	1.465	1.468	1.467	22.904	22.951	22.93	0.962	3.77
180	1.420	1.421	1.421	22.200	22.216	22.21	0.932	6.79

Table A23 Treatment of IC+RB5 dye in synthetic wastewater at an initial concentration of 50 ppm of Experiment condition 3 with MnF photocatalyst (Control).

Time	Abs			Concentration			C/C_0	%
(min)	1	2	Avg	1	2	Avg		Removal
0	1.516	1.516	1.516	23.701	23.701	23.70	1.000	0.00
10	1.308	1.332	1.320	20.449	20.824	20.64	0.871	12.93
180	1.220	1.266	1.243	19.073	19.793	19.43	0.820	18.01

Table A24 Treatment of IC+RB5 dye in synthetic wastewater at an initial concentration of 50 ppm of Experiment condition 3 MnFG1 photocatalyst (Control).

Time	Abs			Concentration			C/C_0	%
(min)	1	2	Avg	1	2	Avg		Removal
0	1.524	1.524	1.524	23.826	23.826	23.83	1.000	0.00
10	1.240	1.236	1.238	19.386	19.324	19.35	0.812	18.77
180	1.240	1.240	1.240	19.386	19.386	19.39	0.814	18.64

Table A25 Treatment of IC+RB5 dye in synthetic wastewater at an initial concentration of 50 ppm of Experiment condition 3 MnFG2 photocatalyst (Control).

Time	Abs			Concentration			C/C_0	%
(min)	1	2	Avg	1	2	Avg		Removal
0	1.524	1.524	1.524	23.826	23.826	23.83	1.000	0.00
10	1.284	1.282	1.283	20.074	20.043	20.06	0.842	15.81
180	1.312	1.314	1.313	20.512	20.543	20.53	0.862	13.85

Table A26 Treatment of IC+RB5 dye in synthetic wastewater at an initial concentration of 50 ppm of Experiment condition 3 MnFG3 photocatalyst (Control).

Time	Abs			Concentration			C/C_0	%
(min)	1	2	Avg	1	2	Avg		Removal
0	1.524	1.524	1.524	23.826	23.826	23.83	1.000	0.00
10	1.308	1.306	1.307	20.449	20.418	20.43	0.858	14.24
180	1.285	1.281	1.283	20.090	20.027	20.06	0.842	15.81

Table A27 Treatment of IC+RB5 dye in synthetic wastewater by the photocatalytic process at an initial concentration of 50 ppm of Experiment condition 4 with MnF photocatalyst.

Time (min)	(Abs)			Concentration (mg. L^{-1})			% Removal	$\ln(C_0/C)$
	1	2	Avg	1	2	Avg		
0	1.524	1.524	1.524	23.826	23.826	23.83	0.00	0.00
10	1.171	1.167	1.169	18.307	18.245	18.28	23.29	0.27
20	1.150	1.147	1.149	17.985	17.934	17.96	24.62	0.28
30	1.130	1.127	1.129	17.663	17.623	17.64	25.95	0.30
40	1.109	1.107	1.108	17.340	17.313	17.33	27.28	0.32
60	1.089	1.088	1.088	17.018	17.002	17.01	28.61	0.34
90	1.047	1.048	1.048	16.373	16.381	16.38	31.27	0.37
120	1.027	1.028	1.027	16.050	16.070	16.06	32.60	0.39
150	1.016	1.018	1.017	15.889	15.914	15.90	33.26	0.40
180	1.006	1.008	1.007	15.728	15.759	15.74	33.92	0.41

Table A28 Treatment of IC+RB5 dye in synthetic wastewater by the photocatalytic process at an initial concentration of 50 ppm of Experiment condition 4 with MnFG1 photocatalyst.

Time (min)	(Abs)			Concentration (mg. L^{-1})			% Removal	$\ln(C_0/C)$
	1	2	Avg	1	2	Avg		
0	1.588	1.588	1.588	24.827	24.827	24.83	0.00	0.00
10	1.189	1.104	1.147	18.589	17.260	17.92	27.80	0.33
20	1.061	1.064	1.063	16.588	16.635	16.61	33.09	0.40
30	0.924	0.930	0.927	14.446	14.540	14.49	41.62	0.54
40	0.858	0.849	0.854	13.414	13.273	13.34	46.25	0.62
60	0.695	0.694	0.695	10.866	10.850	10.86	56.27	0.83
90	0.342	0.363	0.353	5.347	5.675	5.51	77.80	1.51
120	0.181	0.191	0.186	2.830	2.986	2.91	88.29	2.14
150	0.089	0.102	0.096	1.391	1.595	1.49	93.99	2.81
180	0.032	0.030	0.031	0.500	0.469	0.48	98.05	3.94

Table A29 Treatment of IC+RB5 dye in synthetic wastewater by the photocatalytic process at an initial concentration of 50 ppm of Experiment condition 4 with MnFG2 photocatalyst.

Time (min)	(Abs)			Concentration (mg. L^{-1})			% Removal	$\ln(C_0/C)$
	1	2	Avg	1	2	Avg		
0	1.588	1.588	1.588	24.827	24.827	24.83	0.00	0.00
10	1.200	0.956	1.078	18.761	14.946	16.85	32.12	0.39
20	1.007	1.029	1.018	15.743	16.087	15.92	35.89	0.44
30	0.838	0.870	0.854	13.101	13.602	13.35	46.22	0.62
40	0.704	0.746	0.725	11.006	11.663	11.33	54.35	0.78
60	0.436	0.460	0.448	6.816	7.192	7.00	71.79	1.27
90	0.182	0.167	0.175	2.845	2.611	2.73	89.01	2.21
120	0.071	0.071	0.071	1.110	1.110	1.11	95.53	3.11
150	0.051	0.049	0.050	0.797	0.766	0.78	96.85	3.46
180	0.036	0.039	0.038	0.563	0.610	0.59	97.64	3.75

Table A30 Treatment of IC+RB5 dye in synthetic wastewater by the photocatalytic process at an initial concentration of 50 ppm of Experiment condition 4 with MnFG3 photocatalyst.

Time (min)	(Abs)			Concentration (mg. L^{-1})			% Removal	$\ln(C_0/C)$
	1	2	Avg	1	2	Avg		
0	1.516	1.516	1.516	23.701	23.701	23.70	0.00	0.00
10	1.177	1.169	1.173	18.401	18.276	18.34	22.63	0.26
20	1.001	1.021	1.011	15.650	15.962	15.81	33.31	0.41
30	0.901	0.884	0.893	14.086	13.820	13.95	41.13	0.53
40	0.770	0.754	0.762	12.038	11.788	11.91	49.74	0.69
60	0.503	0.484	0.494	7.864	7.567	7.72	67.45	1.12
90	0.219	0.203	0.211	3.424	3.174	3.30	86.08	1.97
120	0.101	0.101	0.101	1.579	1.579	1.58	93.34	2.71
150	0.063	0.054	0.059	0.985	0.844	0.91	96.14	3.25
180	0.059	0.044	0.052	0.922	0.688	0.81	96.60	3.38

Table A31 Treatment of TC in synthetic wastewater at an initial concentration of 50 ppm of Experiment condition 1 (Control).

Time	Abs			Concentration			C/C_0	%
(min)	1	2	Avg	1	2	Avg		Removal
0	1.607	1.607	1.607	47.810	47.810	47.81	1.000	0.00
10	1.576	1.543	1.560	46.888	45.906	46.40	0.970	2.96
240	1.390	1.356	1.373	41.354	40.342	40.85	0.854	14.56

Table A32 Treatment of TC in synthetic wastewater at an initial concentration of 50 ppm of Experiment condition 2 (Control).

Time	Abs			Concentration			C/C_0	%
(min)	1	2	Avg	1	2	Avg		Removal
0	1.649	1.649	1.649	49.059	49.059	49.06	1.000	0.00
10	1.607	1.605	1.606	47.810	47.750	47.78	0.974	2.61
240	1.635	1.638	1.637	48.643	48.732	48.69	0.992	0.76

Table A33 Treatment of TC in synthetic wastewater at an initial concentration of 50 ppm of Experiment condition 3 with MnF photocatalyst (Control).

Time	Abs			Concentration			C/C_0	%
(min)	1	2	Avg	1	2	Avg		Removal
0	1.649	1.649	1.649	49.059	49.059	49.06	1.000	0.00
10	1.535	1.530	1.533	45.668	45.519	45.59	0.929	7.06
240	1.431	1.430	1.431	42.574	42.544	42.56	0.867	13.25

Table A34 Treatment of TC in synthetic wastewater at an initial concentration of 50 ppm of Experiment condition 3 MnFG1 photocatalyst (Control).

Time	Abs			Concentration			C/C_0	%
(min)	1	2	Avg	1	2	Avg		Removal
0	1.649	1.649	1.649	49.059	49.059	49.06	1.000	0.00
10	1.535	1.530	1.533	45.668	45.519	45.59	0.929	7.06
240	1.431	1.430	1.431	42.574	42.544	42.56	0.867	13.25

Table A35 Treatment of TC in synthetic wastewater at an initial concentration of 50 ppm of Experiment condition 3 MnFG2 photocatalyst (Control).

Time	Abs			Concentration			C/C_0	%
(min)	1	2	Avg	1	2	Avg		Removal
0	1.649	1.649	1.649	49.059	49.059	49.06	1.000	0.00
10	1.580	1.579	1.580	47.007	46.977	46.99	0.958	4.21
240	1.471	1.469	1.470	43.764	43.704	43.73	0.891	10.86

Table A36 Treatment of TC in synthetic wastewater at an initial concentration of 50 ppm of Experiment condition 3 MnFG3 photocatalyst (Control).

Time	Abs			Concentration			C/C_0	%
(min)	1	2	Avg	1	2	Avg		Removal
0	1.649	1.649	1.649	49.059	49.059	49.06	1.000	0.00
10	1.608	1.607	1.608	47.840	47.810	47.82	0.975	2.52
240	1.572	1.568	1.570	46.769	46.650	46.71	0.952	4.79

Table A37 Treatment of TC dye in synthetic wastewater by the photocatalytic process at an initial concentration of 50 ppm of Experiment condition 4 with MnF photocatalyst.

Time (min)	(Abs)			Concentration (mg. L^{-1})			% Removal	$\ln(C_0/C)$
	1	2	Avg	1	2	Avg		
0	1.590	1.590	1.590	47.304	47.304	47.30	0.00	0.00
10	1.010	1.013	1.012	30.049	30.138	30.09	36.38	0.45
20	0.996	0.999	0.998	29.646	29.734	29.69	37.24	0.47
30	0.983	0.986	0.984	29.243	29.331	29.29	38.09	0.48
40	0.956	0.959	0.957	28.438	28.524	28.48	39.79	0.51
60	0.902	0.905	0.903	26.828	26.910	26.87	43.20	0.57
90	0.794	0.796	0.795	23.607	23.682	23.64	50.02	0.69
120	0.739	0.742	0.741	21.997	22.068	22.03	53.42	0.76
150	0.685	0.688	0.686	20.387	20.454	20.42	56.83	0.84
180	0.631	0.633	0.632	18.777	18.840	18.81	60.24	0.92
240	0.577	0.579	0.578	17.166	17.226	17.20	63.65	1.01

Table A38 Treatment of TC in synthetic wastewater by the photocatalytic process at an initial concentration of 50 ppm of Experiment condition 4 with MnFG1 photocatalyst.

Time (min)	(Abs)			Concentration (mg. L^{-1})			% Removal	$\ln(C_0/C)$
	1	2	Avg	1	2	Avg		
0	1.564	1.564	1.564	46.531	46.531	46.53	0.00	0.00
10	1.444	1.451	1.448	42.960	43.169	43.06	7.45	0.08
20	1.331	1.338	1.335	39.599	39.807	39.70	14.67	0.16
30	1.234	1.300	1.267	36.713	38.676	37.69	18.99	0.21
40	1.233	1.161	1.197	36.683	34.541	35.61	23.47	0.27
60	1.079	1.135	1.107	32.101	33.767	32.93	29.22	0.35
90	1.001	0.972	0.987	29.781	28.918	29.35	36.92	0.46
120	0.890	0.928	0.909	26.478	27.609	27.04	41.88	0.54
150	0.776	0.802	0.789	23.087	23.860	23.47	49.55	0.68
180	0.720	0.561	0.641	21.421	16.690	19.06	59.05	0.89
240	0.534	0.000	0.267	15.887	0.000	7.94	82.93	1.77

Table A39 Treatment of TC in synthetic wastewater by the photocatalytic process at an initial concentration of 50 ppm of Experiment condition 4 with MnFG2 photocatalyst.

Time (min)	(Abs)			Concentration (mg. L^{-1})			% Removal	$\ln(C_0/C)$
	1	2	Avg	1	2	Avg		
0	1.576	1.596	1.586	46.873	47.468	47.17	0.00	0.00
10	1.449	1.489	1.469	43.102	44.292	43.70	7.36	0.08
20	1.340	1.360	1.350	39.851	40.446	40.15	14.88	0.16
30	1.253	1.263	1.258	37.285	37.583	37.43	20.64	0.23
40	1.157	1.179	1.168	34.429	35.084	34.76	26.32	0.31
60	1.044	1.068	1.056	31.053	31.767	31.41	33.41	0.41
90	0.907	0.927	0.917	26.984	27.579	27.28	42.16	0.55
120	0.787	0.809	0.798	23.408	24.075	23.74	49.67	0.69
150	0.653	0.695	0.674	19.432	20.687	20.06	57.47	0.86
180	0.491	0.601	0.546	14.615	17.888	16.25	65.55	1.07
240	0.273	0.276	0.275	8.129	8.219	8.17	82.67	1.75

Table A40 Treatment of TC in synthetic wastewater by the photocatalytic process at an initial concentration of 50 ppm of Experiment condition 4 with MnFG3 photocatalyst.

Time (min)	(Abs)			Concentration (mg. L^{-1})			% Removal	$\ln(C_0/C)$
	1	2	Avg	1	2	Avg		
0	1.607	1.607	1.607	47.810	47.810	47.81	-1.07	-0.01
10	1.468	1.512	1.490	43.674	44.984	44.33	6.29	0.06
20	1.348	1.381	1.365	40.104	41.086	40.60	14.18	0.15
30	1.210	1.289	1.250	35.999	38.349	37.17	21.42	0.24
40	1.155	1.124	1.140	34.362	33.440	33.90	28.33	0.33
60	1.006	1.003	1.005	29.930	29.840	29.88	36.82	0.46
90	0.899	0.796	0.848	26.746	23.682	25.21	46.70	0.63
120	0.720	0.654	0.687	21.421	19.457	20.44	56.79	0.84
150	0.625	0.494	0.560	18.594	14.697	16.65	64.81	1.04
180	0.511	0.393	0.452	15.203	11.692	13.45	71.57	1.26
240	0.316	0.249	0.283	9.401	7.408	8.40	82.23	1.73

Biography

Name-Surname	Mr. Sakchai Kaewsubdejsiri
Date of Birth	08 August 1992
Address	5 1 / 3 Moo 7 , Ban Chong Subdistrict, Phanom Sarakham District, Chachoengsao Province, 24120, Thailand
Education	Bachelor of Engineering, Department of Civil Engineering, Environmental Engineering Branch
Experiences Work	2016 Prime Product Industry Co., Ltd. Position : Environmental Officer 2017 Platinum Chemical Engineering Co., Ltd. Position: Sales Engineer 2017-2022 Clean and Green Co., Ltd. Position: Assistant Environmental Manager 2022-2025 Clean and Green Co., Ltd. Position: Environmental Manager and Acting Plant Manager 2025 Envirent Engine Co., Ltd. Position: Managing Director
Telephone Number	088-579-3042
Email Address	gung.kaewsubdejsiri@gmail.com